LINKER DESIGN PRINCIPLES AND IMPLEMENTATION IN HIGH
PERFORMANCE MICROPOROUS COORDINATION POLYMERS

by

Jennifer K. Schnobrich

A dissertation submitted in partial fulfillment
of the requirements for the degree of
Doctor of Philosophy
(Chemistry)
in The University of Michigan
2011

Doctoral Committee:

     Professor Adam J. Matzger, Chair
     Professor David W. Gidley
     Professor Vincent L. Pecoraro
     Assistant Professor Anne J. McNeil

ACKNOWLEDGEMENTS

TABLE OF CONTENTS

CHAPTER 3.   A Highly Connected Network for the Stabilization of Non-Interpenetrated Porous Coordination Polymers

CHAPTER 4.   Linker-Directed Vertex Desymmetrization for the Production of Coordination Polymers with High Porosity

LIST OF FIGURES

Figure

LIST OF TABLES

ABSTRACT

Due to their tunable and varied structures, microporous coordination polymers (MCPs) are considered promising candidates for gas storage, separations, and catalysis. Performance in these applications is highly dependent on surface area, which is greatly impacted by factors such as incomplete guest removal, framework collapse, non-optimal linker or metal cluster geometry, and/or framework interpenetration. The studies within this thesis serve to address these problems by offering a method for understanding surface area as well as the implementation of novel linker design strategies for avoiding common structural impediments to achieving high surface area materials.

A surface area prediction method is introduced for the rational dissection of structures into building block components so that surface area contributions from linker and metal cluster units may be recognized. MOF-5 and HKUST-1 are used as prototypical structures to analyze MCPs with octahedral $M_4O(CO_2R)_6$ and paddlewheel $M_2(CO_2R)_4$ metal clusters. It was determined that the theoretical upper limit of a benzene linked system is approximately 10,500 m^2/g and that features such as ring fusion, functional group substitution, and interpenetration reduce MCP surface areas.

Implementation of design guidelines determined through theoretical studies led to the development and application of two synthetic strategies. In one method, a large linker containing seven benzene units is stabilized with six carboxylate groups to form a non-interpenetrated MCP, UMCM-300. The lack of interpenetration is an outstanding feature

that is attributed to the formation of a (3,24)-connected network that contains cuboctahedral cages containing small pore apertures too small to allow interpenetration.

In the second method, five examples of non-interpenetrated MCPs are derived by employing linkers with symmetry inequivalent coordinating groups. Gas sorption in polymorphic frameworks, UMCM-152 and UMCM-153, reveals nearly identical properties with BET surface areas in the range of 3300-3500 m^2/g and excess hydrogen uptakes of 5.7 and 5.8 wt % at 77 K. In contrast, adsorption of organosulfur compounds shows remarkably different capacities demonstrating the importance of pore size and shape on liquid phase adsorption. MCPs constructed by this method also exhibit rare metal clusters and network topologies previously unseen, demonstrating the potential for reduced symmetry linkers in forming MCPs with new properties.

CHAPTER 1

Introduction

1.1. Microporous Coordination Polymers

Microporous coordination polymers (MCPs) are a class of porous materials composed of organic ligands coordinated to metal ions having well-defined structures with tunable pore sizes. These materials are described with varying terminology including metal-organic framework (MOF), metal-organic material (MOM), porous coordination polymer (PCP), and porous coordination network (PCN). They are often named to reflect the location of creation: University of Michigan Crystalline Material (UMCM), Hong Kong University of Science and Technology (HKUST), Matériaux de l'Institut Lavoisier (MIL), University of Nottingham (NOTT), and Northwestern University (NU).

Compared to other classes of porous materials such as zeolites and activated carbon, the combination of high surface areas, high accessible pore volumes, and narrow pore size distributions gives MCPs an advantage in potential applications such as molecular recognition, storage, and catalysis.[1] Two prototypical MCPs that were among the first to demonstrate permanent porosity and serve as important examples in these applications are MOF-5[2] and HKUST-1.[3] MOF-5 is synthesized from terephthalic acid and zinc nitrate. Heating in the presence of *N,N*-diethylformamide (DEF) leads to the

formation of a cubic structure having pores of approximately 1.3 nm diameter (Figure

1.1a). MOF-5 has a BET surface area of 3800 m^2/g with a free volume of 77 %.[4]

HKUST-1 is synthesized using trimesic acid and copper nitrate, which produce a caged

structure with two distinct pores of approximately 1.1 nm and 0.6 nm diameter (Figure

1.1b). The BET surface area of HKUST-1 is approximately 1900 m^2/g and free pore

volume is 69.5 %.[5]
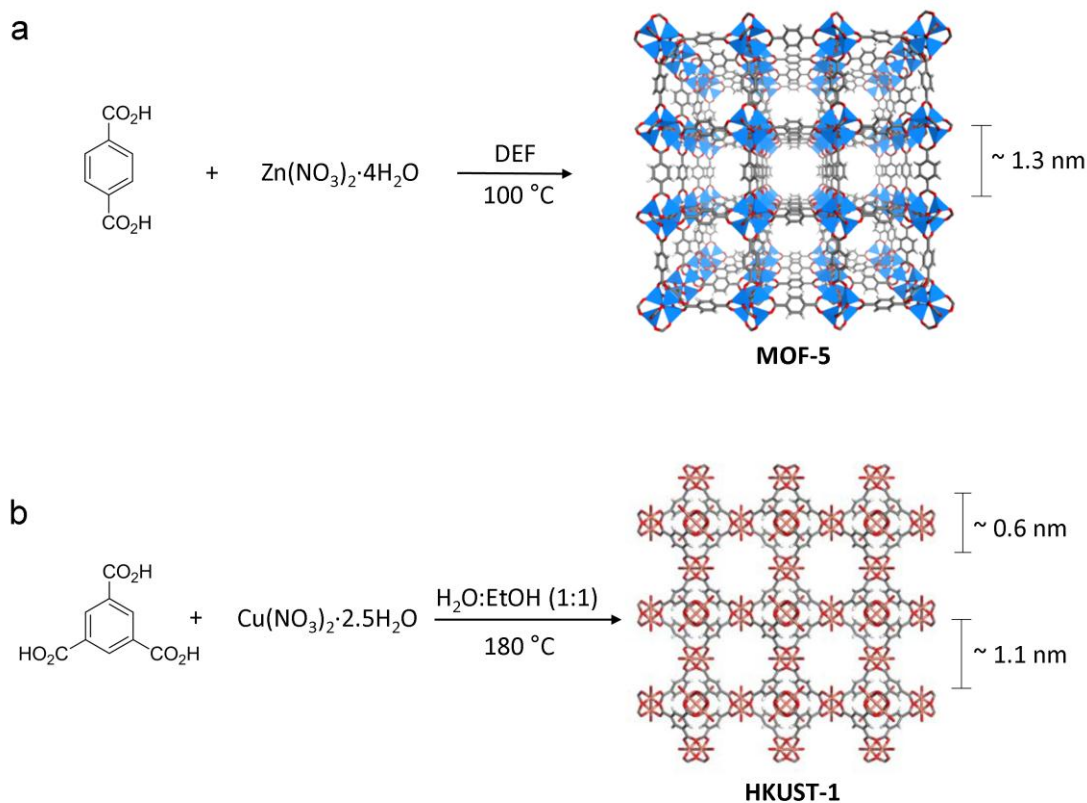
Figure 1.1 Synthesis of prototypical MCPs: (a) MOF-5,[1] and (b) HKUST-1.[2]

1.2. Building Block Components

An attractive feature in MCPs is the ease by which structures can be tailored for specific applications. By selecting the building block components employed in synthesis, properties such as surface area, pore size, and density can be influenced and, in favorable cases, controlled. Consequently, thousands of structures have been synthesized by selecting different organic and inorganic building units.[6]

1.2.1. Linkers

Organic ligands, referred to as linkers when used in the construction of extended coordination networks, provide geometric predictability based upon the size, shape, and number and placement of coordinating groups. MOF-5, also named IRMOF-1, is the parent material in a series of MCPs with the same net (a isoreticular series) where the carboxylate linker is lengthened and/or substituted with various functional groups.[7] This series has served as a foundation for understanding how linker modifications affect structural and chemical properties.[3,8,9]

Lengthening the span between coordination groups is often accomplished through adding aryl or triple-bonded units while maintaining linker shape. In one example, linear dicarboxylate linkers coordinate with octahedral $Zn_4O(CO_2R)_6$ nodes to form a structure with cubic pores having sizes directly proportional to linker length (Figure 1.2). Although these types of extensions tend to form structures with low densities and high surface areas, extended structures are also more inclined to interpenetrate and collapse upon guest removal, thus limiting their applications.
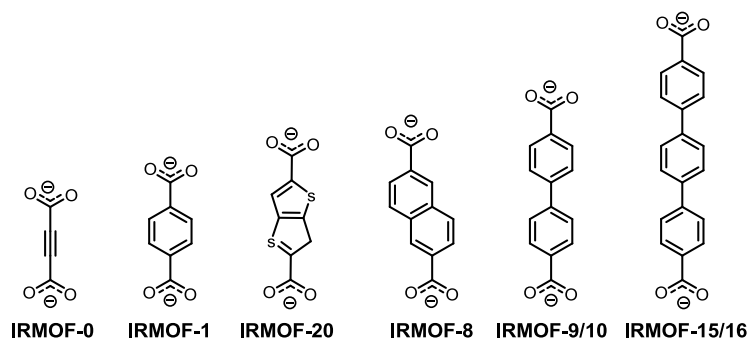
Figure 1.2. Linker extension leading to MCPs having the same network connectivity as MOF-5.[7,9,10]

Functionalization is an effective method for modifying the structures of MCPs. For example, a variety of terephthalate derivatives coordinate with zinc to form the same network as MOF-5. (Figure 1.3) By incorporating functional groups that are not part of the coordination polymer backbone, host-guest interactions such as heats of adsorption and selectivity can be enhanced.[7] Additionally, functional groups not compatible with MCP synthetic conditions can be incorporated through post-synthetic modification steps.[11] Finally, complex scaffolds using multivariate functionalities in both random and systematic core-shell layers have been demonstrated,[12,13] revealing the versatility of organic linker functionalization in controlling the properties in MCPs.
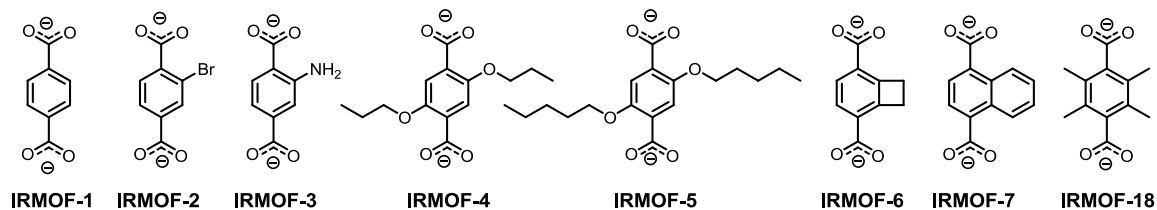
Figure 1.3. Terephthalate linker and derivatives leading to the formation of MCPs having the same network connectivity as MOF-5.[7]

4

1.2.2. Metal Clusters

Metal clusters act as connectors between the organic linkers and offer directionality that controls the pore shape and network topology of a structure. Unlike most linkers, metal clusters form in-situ and during the synthesis of the structure. Therefore, variables including solvent, temperature, and the presence of additives may all influence the type of metal cluster and, in turn, the network that will form.

Two of the metal clusters first demonstrated to effectively produce permanently porous MCPs, $Zn_4O(CO_2R)_6$ and $Cu_2(CO_2R)_4$, are still among the most commonly employed. The basic zinc carboxylate cluster, $Zn_4O(CO_2R)_6$, contains four Zn^{2+} atoms bound by a μ_4-O^{2-} that coordinates with six carboxylate groups in an octahedral geometry (Figure 1.4a). This cluster is featured in various high performance MCPs including MOF-5,[2] MOF-177,[14] IRMOF-20,[15] UMCM-1,[16] and UMCM-2.[17] Metals such as beryllium and magnesium have been considered desirable substitutes for zinc in this cluster geometry due to their relatively lighter atomic weights that would reduce the weight of the framework;[18,19] however, experimental efforts have yet to match theoretically attainable properties.[20] Copper paddlewheel $Cu_2(CO_2R)_4$ clusters are formed by four carboxylates coordinating to two Cu^{2+} ions in a square planar geometry (Figure 1.4b). Guest molecules coordinate in apical positions and can typically be removed to create two coordinatively unsaturated metal sites producing a strong binding energy between the framework and adsorbate guests. This has been demonstrated in materials including HKUST-1,[3] MOF-505,21 PCN-12 and PCN-12',[22] NOTT-101, and NOTT-102.[23,24] Other metals, such as zinc[25] and molybdenum[26] can form this metal cluster motif in coordination polymers and numerous others have demonstrated the geometry as discreet inorganic clusters.
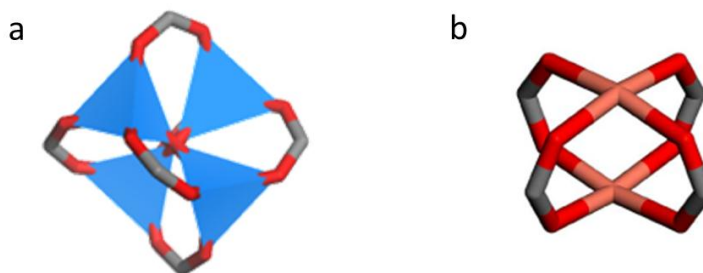
Figure 1.4: (a) $Zn_4O(CO_2R)_6$ and (b) $Cu_2(CO_2R)_4$ metal clusters.

1.3. Hydrogen Storage

Due to their exceptional surface areas, tunable pore sizes, and the ease of imparting functionality, MCPs are considered potential materials for hydrogen storage. The Department of Energy (DOE) has set a target that onboard automobile fuel storage systems should store 0.055 kg H_2/kg by 2015 with an ultimate goal of 0.075 kg H_2/kg.[27] Gravimetric uptakes are commonly reported as excess capacities, the amount of H_2 in excess of what would occupy the same free volume if the adsorbent was absent; however, the absolute capacity, the total amount contained within the material is also meaningful, especially at very high pressures. The volumetric capacity of hydrogen is also an important consideration and the DOE as has set targets of 0.040 kg H_2/L (year 2015) and 0.070 kg H_2/L (ultimate goal)[27] With these criteria in mind, numerous studies have probed the mechanism of adsorption in MCPs with the aim of determining ideal properties for efficient hydrogen storage.[28,29]

Neutron diffraction and inelastic neutron scattering techniques have provided evidence that adsorption occurs first near the metal clusters of coordination polymers and secondly along the linker.[30] Because the number of sites available for adsorption is limited by the size and accessibility of the metal cluster, the length of the linker provides

6

a significant amount of adsorption sites important to the saturation capacity of the framework. This aspect is related to the surface area of the MCP and numerous studies have shown that high hydrogen uptakes are correlated with high surface areas.[5]

Currently, the top performing materials for hydrogen storage include MOF-177 (H_2 uptake 7.6 wt%, BET surface area 4750 m^2/g),[5,16] MOF-210 (H_2 uptake 8.6 wt%, BET surface area 6240 m^2/g),[31] and NU-100 (H_2 uptake 9.95 wt%, BET surface area 6143 m^2/g).[32] Although the excess saturation capacities of these materials at 77 K exceeds 7.5 wt%, the weight of a cryogenic storage device is not taken into account and this is needed for a viable storage system incorporating MCPs. Hence, MCPs with higher surface areas must be produced to ultimately meet DOE goals.

1.4. Surface Area

Surface area is a key property of coordination polymers and relates to their physisorptive capacities for gasses. Surface area is typically determined using a nitrogen sorption isotherm in which the uptake of N_2 at low pressures is translated into a surface area using common models such as the Brunauer-Emmett-Teller (BET) and Langmuir methods. Unfortunately, experimental surface areas in the literature are not consistently reported in terms of method and pressure range. The BET method is the most appropriate for determining surface area in MCPs because it assumes multilayer coverage; however, calculated values may still fluctuate depending on the pressure range used for analysis.[33]

Surface area has often been used as a metric for sample quality. Instances of framework collapse, incomplete guest removal, and interpenetration are often cited to rationalize low surface areas. These phenomena contribute to materials non-ideality

because they can block surface sites making them unavailable for adsorption, constrict pore apertures, increase framework weight, and give rise to broad pore size distributions. The improvement of materials which have low or non-optimal surface areas represents a significant challenge in the pursuit of MCPs with high surface areas. Therefore, a careful understanding of why materials fail to meet expectations is essential for the development of high performance coordination polymers for applications such as fuel gas storage.

1.4.1. Framework collapse

Framework collapse is defined by the partial or complete loss of crystallinity of a material and is diagnosed by the shifting or broadening of peaks in a powder X-ray diffraction pattern. This most commonly occurs during sample activation, the process by which the internal surface of a material is freed of solvent and other guests. Traditional methods for activation include the use of reduced pressure and mild heating to remove volatile guests from within a framework. Recent efforts for avoiding collapse by minimizing the surface tension of exiting guests has led to techniques of benzene sublimation[34] and supercritical carbon dioxide processing.[35] These new methods have demonstrated promising results; for example, supercritical carbon dioxide was employed to activate two MCPs having the highest surface areas reported to date, MOF-210 (BET surface area 6240 m^2/g)[31] and NU-100 (BET surface area 6143 m^2/g).[32] These materials exhibited nonporous behavior by activation with traditional methods. Despite these advances, many materials still possess less than ideal surface areas, prompting the need for more robust structures.

1.4.2. Interpenetration

Interpenetration is the physical entanglement of two or more frameworks. Although few tools exist for predicting the likelihood of interpenetration,[36] frameworks having large pores and long linkers represent the majority of interpenetrated structures. In certain cases interpenetration may improve surface area by stabilizing a framework likely to collapse;[37] however, it is most generally accepted that interpenetration prevents a material from achieving optimal surface area values because surface sites along the linker and metal cluster become inaccessible for adsorption. Recent efforts to inhibit interpenetration have focused on epitaxial growth,[38] incorporation of steric bulk on the linker[39] or guest coordinating group,[40] adjustments in solution concentration and reaction temperature,[41] and the use of templating agents[42] However, these methods are not universally effective, leaving most efforts for avoiding interpenetration a serendipitous endeavor.

1.5. Context and Organization of Thesis

Because surface area is a significant property in MCPs which relates to both physisorptive capacity and sample quality, it is important that factors influencing surface area be better understood. The research presented in this thesis serves to address these considerations by offering a method for verifying maximum attainable surface area as well as novel linker design strategies for avoiding common surface area impediments.

A predictive tool termed the linker to metal cluster (LiMe) ratio is introduced for understanding surface area in MCPs (Chapter 2).[43] Prior to this work, a study using the structure of graphene suggested that high surface areas in MCPs can be achieved by

maximizing the number of exposed linker edges and rings in a structure.[14] However, an accurate theoretical surface area model based upon that study could not be adapted for MCPs because the structures did not imitate true linker shape or include surface area contributions from metal clusters. The LiMe ratio surface area prediction method utilizes crystal structures from real MCPs and models based upon linker extensions of these structures to generate a surface area prediction method that can directly provide insight into the effects of linker size, geometry and number of coordinating groups as well as metal cluster geometry.

Lessons learned from the theoretical surface area work are applied toward the synthesis of new MCPs using two novel linker design strategies. In the first approach, a large linker containing seven benzene units and six carboxylate groups assembled with copper paddlewheel clusters forming a non-interpenetrated MCP, UMCM-300 (Chapter 3). The lack of interpenetration is an outstanding feature that is attributed to the formation of a (3,24)-connected network that contains cuboctahedral cages containing small pore apertures too small to allow interpenetration. Since the original synthesis of UMCM-300, this strategy has proven to be universally applicable to linkers containing the same geometry. Isoreticular frameworks derived from even larger linkers have recently been published by other groups in which the same (3,24)-connected network allows for the formation of non-interpenetrated MCPs with BET surface areas exceeding 6,000 m^2/g.

In a second synthetic strategy, a new genre of linkers having symmetry inequivalent coordination groups is presented and leads to the formation of five non-interpenetrated MCPs (Chapter 4).[44] Two conceptual pathways for the production of these linkers is introduced based upon ring addition and carboxylate

addition/rearrangement. Unlike highly symmetrical linkers which tend to interpenetrate, networks derived from the reduced symmetry linkers lack the appropriate symmetry for self-interpenetration due to the non-uniformity of distances between coordinating groups and therefore promote the formation of highly porous MCPs. Structural features, such as rare metal clusters and new network topologies are identified in the new MCPs derived from reduced symmetry linkers. Additionally, a set of polymorphic frameworks (having the same building block components but different network connectivity) is employed to demonstrate key differences in gas and liquid phase adsorption.

Finally, conclusions and an outlook on the field are presented, including further areas of study in developing surface area prediction methods and improving framework stability (Chapter 5).

1.6. References

(1)   Mueller, U.; Schubert, M.; Teich, F.; Puetter, H.; Schierle-Arndt, K.; Pastré, J. *J. Mater. Chem*. **2006**, *16*, 626-636.

(2)   Li, H.; Eddaoudi, M.; O'Keeffe, M.; Yaghi, O. M. *Nature* **1999**, *402*, 276-279.

(3)   Chui, S. S. Y.; Lo, S. M. F.; Charmant, J. P. H.; Orpen, A. G.; Williams, I. D. *Science* **1999**, *283*, 1148-1150.

(4)   Kaye, S. S.; Dailly, A.; Yaghi, O. M.; Long, J. R. *J. Am. Chem. Soc*. **2007**, *129*, 14176-14177.

(5)   Wong-Foy, A. G.; Matzger, A. J.; Yaghi, O. M. *J. Am. Chem. Soc.* **2006**, *128*, 3494 - 3495.

(6)   Ockwig, N. W.; Delgado-Friedrichs, O.; O'Keefe, M.; Yaghi, O. M. *Acc. Chem. Res*. **2005**, *38*, 176-182.

(7)   Eddaoudi, M.; Kim, J.; Rosi, N.; Vodak, D.; Wachter, J.; O'Keefe, M.; Yaghi, O. M. *Science*, **2002**, *295*, 469-472.

(8)   Düren, T.; Bae, Y.-S.; Snurr, R. Q. *Chem. Soc. Rev.* **2009**, *38*, 1237-1247.

(9)   Rowsell, J. L. C.; Yaghi, O. M. *J. Am. Chem. Soc.*, **2006**, *128*, 1304-1315

(10)   Tranchemontagne, D. J.; Hunt, J. R.; Yaghi, O. M. *Tetrahedron*, **2008**, *64*, 8553-8557.

(11)   Tanabe, K. K.; Cohen, S. M.; *Chem. Soc. Rev*. **2011**, *40*, 498-519.

(12)   Koh, K.; Wong-Foy, A. G.; Matzger, A. J. *Chem Commun*. **2009**, 6162-6164.

(13)   Deng, H.; Doonan, C. J.; Furukawa, H.; Ferreira, R. B.; Towne, J.; Knobler, C. B.; Wang, B.; Yaghi, O. M. *Science*, **2010**, *327*, 846-850.

(14)   Chae, H. K.; Siberio-Pérez, D. Y.; Kim, J.; Go, Y.; Eddaoudi, M.; Matzger, A. J.; O'Keeffe, M.; Yaghi, O. M. *Nature* **2004**, *427*, 523.

(15)   Rowsell, J. L. C.; Yaghi, O. M. *J. Am. Chem. Soc*. **2006**, *128*, 1304-1314.

(16)   Koh, K.; Wong-Foy, A. G.; Matzger, A. J. *J. Am. Chem. Soc*. **2009**, *131*, 4184-4185.

(17)   Koh, K.; Wong-Foy, A. G.; Matzger, A. J. *Angew. Chem. Int. Edit*. **2008**, *47*, 677-680.

(18)   Han, S.S.; Deng, W.-Q.; Goddard III, W. A. *Angew. Chem.* **2007**, *119*, 6405-6408.

(19)   Han, S. S.; Mendoza-Cortes, J. L.; Goddard, W. A. *Chem. Soc. Rev*. **2009**, *38*, 1460-1476.

(20)   Hausdorf, S.;Baitalow, F.; Böhle,T.; Rafaja, D.; Mertens, F.O. R. L. *J. Am. Chem. Soc*. **2010**, *132*, 10978-10981.

(21)   Chen, B. L.; Ockwig, N. W.; Millward, A. R.; Contreras, D. S.; Yaghi, O. M. *Angew. Chem. Int. Edit*. **2005**, *44*, 4745-4749.

(22)   Wang, X. S.; Ma, S. Q.; Forster, P. M.; Yuan, D. Q.; Eckert, J.; Lopez, J. J.; Murphy, B. J.; Parise, J. B.; Zhou, H. C. *Angew. Chem. Int. Edit*. **2008**, *47*, 7263-7266.

(23)   Lin, X.; Jia, J. H.; Zhao, X. B.; Thomas, K. M.; Blake, A. J.; Walker, G. S.; Champness, N. R.; Hubberstey, P.; Schröder, M. *Angew. Chem. Int. Edit*. **2006**, *45*, 7358-7364.

(24)   Lin, X.; Telepeni, I.; Blake, A. J.; Dailly, A.; Brown, C. M.; Simmons, J. M.; Zoppi, M.; Walker, G. S.; Thomas, K. M.; Mays, T. J.; Hubberstey, P.; Champness, N. R.; Schröder, M. *J. Am. Chem. Soc*. **2009**, *131*, 2159-2171.

(25)   Li, H.; Eddaoudi, M.; Groy, T. L.; Yaghi, O. M. *J. Am. Chem. Soc*. **1998,** *120*, 8571-8572

(26)   Kramer, M.; Schwarz, U.; Kaskel, S. *J. Mater. Chem.*, **2006**, *16*, 2245-2248

(27)   U.S. Department of Energy, Targets for on-board hydrogen storage systems: http://www1.eere.energy.gov/hydrogenandfuelcells/storage/current_technology.html

(28)   Murray, L. J.; Dincă, M.; Long, J. R. *Chem. Soc. Rev*. **2009**, *38*, 1294-1314.

(29)   Frost, H.; Snurr, R. Q. *J. Phys. Chem. C*, **2007**, *111* 18794-18803.

(30)   Rosi, N. L.; Eddaoudi, M.; Vodak, D. T.; Eckert, J.; O'Keefe, M.; Yaghi, O. M. *Science*, **2003**, *300*, 1127-1129.

(31)   Furukawa, H.; Ko, N.; Go, Y. B.; Aratani, N.; Choi, S. B.; Choi, E.; Yazaydin, E.; Ö.; Snurr, R. Q.; O'Keeffe, M.; Kim, J.; Yaghi, O. M. *Science* **2010**, *329*, 424-428.

(32)   Farha, O. K.; Yazaydin, Ö.; Eryazici, I.; Malliakas, C. D.; Hauser, B. G.; Kanatzidis, M. G.; Nguyen, S. T.; Snurr, R.Q.; Hupp, J. T. *Nature Chemistry*, **2010**, *2*, 944 - 948.

(33)   Walton, K. S.; Snurr, R. Q. *J. Am. Chem.Soc*. **2007**, *129*, 8552-8556.

(34)   Ma, L.; Jin, A.; Xie, Z.; Lin,W. *Angew. Chem. Int. Ed*. **2009**, *48*, 9905-9908.

(35)   Nelson, A. P.; Farha, O. K.; Mulfort, K. L.; Hupp, J. T. *J. Am. Chem. Soc*. **2009**, *131*, 458-460.

(36)   Reineke, T. M.; Eddaoudi, M.; Moler, D.; O'Keeffe, M.; Yaghi, O. M. *J. Am. Chem. Soc.* **2000**, *122*, 4843-4844.

(37)   Ma, S. Q.; Sun, D. F.; Ambrogio, M.; Fillinger, J. A.; Parkin, S.; Zhou, H. C. *J. Am. Chem. Soc*. **2007**, *129*, 1858-1859.

(38)   Shekhah, O.; Wang, H.; Paradinas, M.; Ocal, C.; Schupbach, B.; Terfort, A.; Zacher, D.; Fischer, R. A.; Woll, C. *Nat Mater* **2009**, *8*, 481-484.

(39)   Farha, O. K.; Malliakas, C. D.; Kanatzidis, M. G.; Hupp, J. T. *J. Am. Chem. Soc.* **2010**, *132*, 950-952.

(40)   He, H.; Yuan, D.; Ma, H.; Sun, D.; Zhang, G.; Zhou, H.-C. *Inorg. Chem.*, **2010**, *49*, 7605-7607.

(41)   Zhang, J.; Wojtas, L.; Larsen, R. W.; Eddaoudi, M.; Zaworotko, M. J. *J. Am. Chem. Soc.* **2009**, *131*, 17040-17041.

(42)   Ma, S. Q.; Sun, D. F.; Ambrogio, M.; Fillinger, J. A.; Parkin, S.; Zhou, H. C. *J. Am. Chem. Soc.* **2007**, *129*, 1858-1859.

(43)   Schnobrich, J. K.; Koh, K.; Sura, K. N.; Matzger, A. J. *Langmuir*, **2010**, *26*, 5808-5814.

(44)   Schnobrich, J. K.; Lebel, O.; Cychosz, K. A.; Dailly, A.; Wong-Foy, A. G.; Matzger, A. J. *J. Am. Chem. Soc.* **2010**, *132*, 13941-13948.

CHAPTER 2

A Framework for Predicting Surface Areas in Microporous Coordination Polymers

2.1. Introduction

The spontaneous assembly of metals with ligands into nanostructured coordination polymers represents an operationally simple approach to create complex structures. Because surface area is an important feature in applications such as molecular recognition, storage, and catalysis,[1,2] much effort has been directed toward understanding how surface areas can be tuned, and in many cases large values are desirable. Most strategies for assembling microporous coordination polymers (MCPs) with high surface areas have focused on using extended organic linkers; however, many attempts with such linkers have yielded materials plagued with low surface areas or nonporous behavior due to issues of incomplete guest removal, framework collapse, nonoptimal linker or metal cluster geometry, and/or framework interpenetration. These problems motivate the use of theoretical calculations that can give an indication as to whether or not a material has achieved its optimal surface area.

2.1.1 Theoretical Method of Surface Area Approximation

Among the options for calculating theoretical surface areas of MCPs, grand canonical Monte Carlo (GCMC) simulations produce accurate values by generating an isotherm based upon a crystal structure.[3] BET surface areas can then be calculated in the same way that experimental values are determined. This method requires considerable computational power. Alternatively, theoretical surface areas have been analyzed with the much simpler Connolly method.[4] These values have been compared with BET and Langmuir values but have demonstrated limited predictive value.[5] Instead, Snurr and co-workers employed a geometric accessible (GA) surface area method in which values coincide well with GCMC theoretical values and with experimental BET determination.[6] The geometric accessible surface area[7] is a useful indicator for judging pore accessibility and crystal quality during experimental optimization of MCP surface area.

Although the aforementioned methods serve as useful tools for predicting the theoretically achievable surface area in MCPs, they require a level of structural characterization that is not always available. Instead, it is more desirable to predict surface area based upon experimental inputs such as the linker and metal components employed in the synthesis. Herein, a method for conceptually dividing the linker and metal cluster contributions to MCP surface area is introduced; by comparing geometric accessible surface areas of a standardized set of MCPs, a system for predicting surface area based upon simple inputs is established. In this method, the influence of size, shape, and weight of linkers with several metal clusters in MCPs is quantified. Similar to previous methods, this technique provides indication of interpenetration, framework collapse, and incomplete solvent removal; however, because a crystal structure is not

required, it gives the quickest feedback based upon minimal input data. Furthermore, because it can be used prior to any characterization procedures, this approach can be applied as a design tool to select linker and metal cluster combinations before any framework has been built.

2.2. Linker to Metal Cluster (LiMe) Ratio

Because surface area is defined in units of square meters per gram, two important factors influencing surface area are the number of surface sites available for guest adsorption and the mass of the scaffold giving rise to these sites. In order to account for each of these factors, MCP structures were conceptually divided into linker and metal cluster portions. Carboxylate groups were counted as part of the metal cluster and were omitted from the linker. A formula unit was determined based upon how many linkers were required to match the number of carboxylates in a metal cluster. The molecular weight of the linker for one formula unit was divided by the metal cluster weight; this value is termed the linker to metal cluster (LiMe) ratio. A sample calculation for a prototype MCP, MOF-5,[8] is detailed below.

Formula unit: $(C_6H_4)_3Zn_4O(CO_2)_6$

Linker weight: $W_{Li} = 228.29$ g/mol

Metal cluster weight: $W_{Me} = 541.70$ g/mol

$$\text{LiMe ratio} = \frac{W_{Li}}{W_{Me}} = \frac{228.29 \text{ g/mol}}{541.70 \text{ g/mol}} = \mathbf{0.42}$$

The LiMe ratio divides MCP weight into linker and metal cluster contributions because each component impacts surface area differently. Metal clusters add significantly to weight but only add modestly to the number of sites available for adsorption. Conversely, most linkers are composed of lightweight elements and are therefore capable of adding a number of adsorption sites with minimal weight penalty. Because most linkers are composed of similar elements (C, N, O, H), linker weight correlates with size; with heavier linkers possessing more adsorption sites and higher surface areas than lighter linkers. With these factors combined, the LiMe ratio serves as a suitable basis for a surface area prediction model. In this method, the linker is readily identified as a synthetic input, and in most cases the metal cluster is determined by solvent choice. Simple characterization techniques, such as vibrational spectroscopy, may be used to identify metal clusters in structures where ambiguity exists.

2.3. Analysis of Structures Having the $M_4O(CO_2R)_6$ Metal Cluster

To build a predictive model for determining the surface area of MCPs, the cubic structure of MOF-5 was used for analysis of MCPs built with the octahedral geometry of an $M_4O(CO_2R)_6$ cluster. A hypothetical series with linkers ranging between 1 and 12 benzenes rings was modeled (Figure 2.1), and the GA surface area was computed.[6] These surface areas are plotted in Figure 2.2.
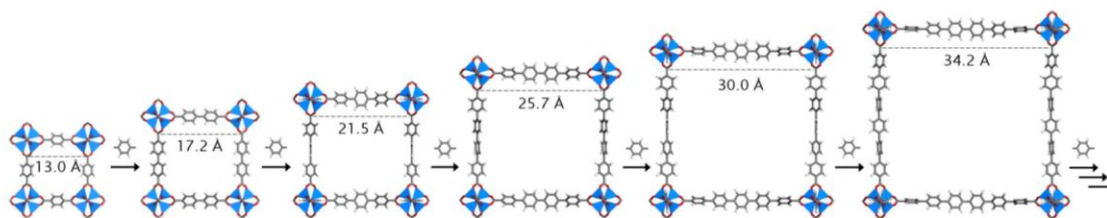
Figure 2.1. Cubic structures were modeled based upon linker extensions of MOF-5. Geometric accessible surface area values were computed for structures up to 12 benzene rings per linker. Values were extrapolated for structures containing up to 49 benzene rings per linker.
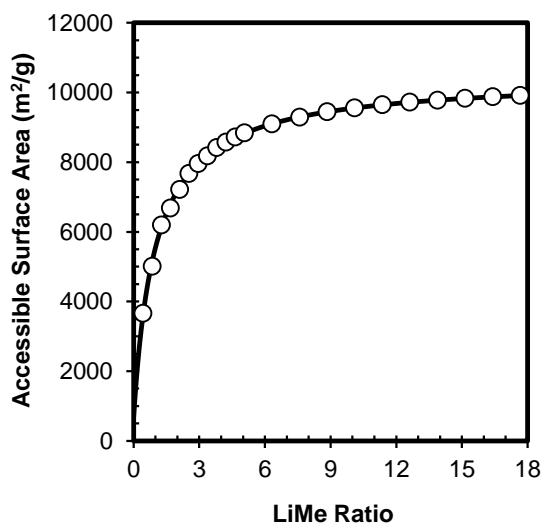
Figure 2.2. Surface areas of MCPs with $Zn_4O(CO_2R)_6$ clusters with structures based upon linker extensions of MOF-5 (○, geometric accessible; ▬, LiMe ratio predicted).

The trend can be fitted to the following equation where y represents the surface area, x is the LiMe ratio, a and b are constants associated with geometry and orientation of linker and metal cluster components, and z is a weight correction factor.

$$y = \frac{ax + bz}{x + 1}$$

This series is expressed in the following surface area equation.

$$surface\ area\ (LiMe)_{M_4O(CO_2R)_6} = \frac{10436\left(\dfrac{W_{Li}}{W_{Me}}\right) + 665\left(\dfrac{541.70}{W_{Me}}\right)}{\left(\dfrac{W_{Li}}{W_{Me}}\right) + 1} \qquad (1)$$

The weight of the metal cluster is integrated into the LiMe ratio through the z correction factor ($541.70/W_{Me}$), therefore, the equation is not solely appropriate for the Zn cluster, but also for all clusters with an octahedral $M_4O(CO_2R)_6$ geometry. For example, $Be_4O(CO_2R)_6$ has been hypothesized as an ideal metal cluster for the construction of porous solids due to its lightweight metal portion leading to the production of ultrahigh surface area MCPs.[9,10] According to this equation, a beryllium benzene dicarboxylate structure[11] would produce a LiMe ratio of 0.72 and a surface area of 5031 m^2/g. This represents greater than 30% improvement from the surface area of MOF-5 and is in reasonable accord with previously reported GCMC predictions of 5270 m^2/g.[12]
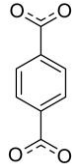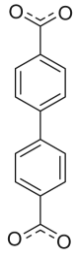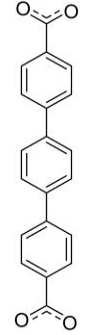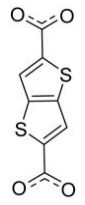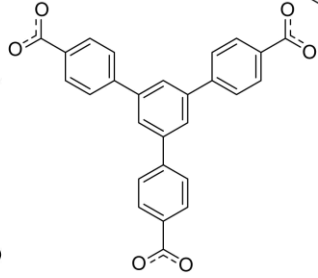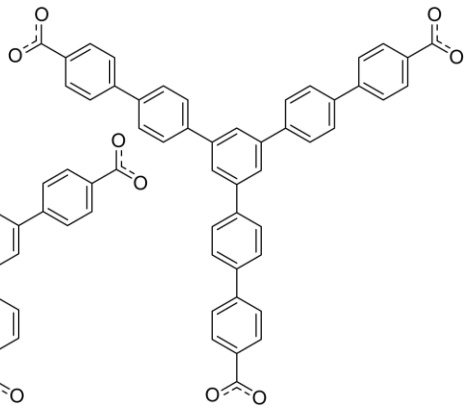
At low LiMe ratios, the surface area changes dramatically with small increases in LiMe ratio. This is consistent with the notion that linker extension is an effective method for enhancing surface area. At larger LiMe ratios, surface area does not significantly change as the LiMe ratio approaches infinity, revealing the upper limit of a conceptually organic-dominated framework to be 10436 m^2/g for this series. This value is in good

agreement with the geometric accessible surface area of an infinite poly(p-phenylene) structure (10577 m^2/g) and represents the maximum attainable surface area for structures derived from benzene rings. It is important to note that this value is independent of the metal or cluster and that other arrangements of benzene rings (e.g., meta, ortho, fused) lead to lower surface areas.

2.3.1. Analysis of Benchmark Materials

In order to assess the generality of the above trends, geometric accessible surface areas were compared to LiMe ratio predicted values for a group of MCPs with basic zinc carboxylate structures (Table 2.1, Figure 2.3). MCPs with significant differences between predicted values were found to possess structural features such as ring fusion, found in the naphthalene dicarboxylate linker of IRMOF-8, or other types of arrangements that are less extended than para-linked benzene rings and therefore produce a less open pore structure for guest adsorption thus reducing surface area. The discrepancy between predictions in IRMOF-20 can be attributed to sulfur being incorporated into the linker, giving it a larger LiMe ratio than other linkers of similar size that are composed of lighter elements. For example, if oxygen were incorporated instead of sulfur, the LiMe ratio would be reduced to 0.59 and the LiMe ratio predicted surface area (4291 m^2/g) would better match the geometric accessible surface area. MCPs involving tritopic linkers, MOF-177 and MOF-200, also fall short of their LiMe ratio predicted surface areas, revealing that differences in linker geometry also affect surface area. The decrease in surface area in these examples can be attributed to less spatial separation between benzene units in the linker making the shape more closely resemble a graphene sheet, thus rendering adsorption sites at the edge inaccessible.[14]

21

Table 2.1. Comparison of surface areas of MCPs with $Zn_4O(CO_2R)_6$ clusters determined through geometric accessible (GA) and LiMe ratio (LiMe) methods.

Linker							
$Zn_4O(CO_2R)_6$ MCP	MOF-5[8]	IRMOF-8[13]	IRMOF-10[13]	IRMOF-16[13]	IRMOF-20[5]	MOF-177[14]	MOF-200[15,16]
LiMe Ratio	0.42	0.70	0.84	1.26	0.77	1.12	1.96
SA (LiMe) (m^2/g)	3555	4688	5126	6133	4916	5827	7135
SA (GA) (m^2/g)	3663	4393	5011	6198	3931	4886	6362
% deviation[a]	3	7	2	1	22	18	11

[a] % Deviation defined as the absolute value of GA-LiMe surface area difference divided by the average GA/LiMe value.

Figure 2.3. Surface areas of MCPs with $Zn_4O(CO_2R)_6$ clusters ($\circ$, geometric accessible; ━, LiMe ratio predicted).
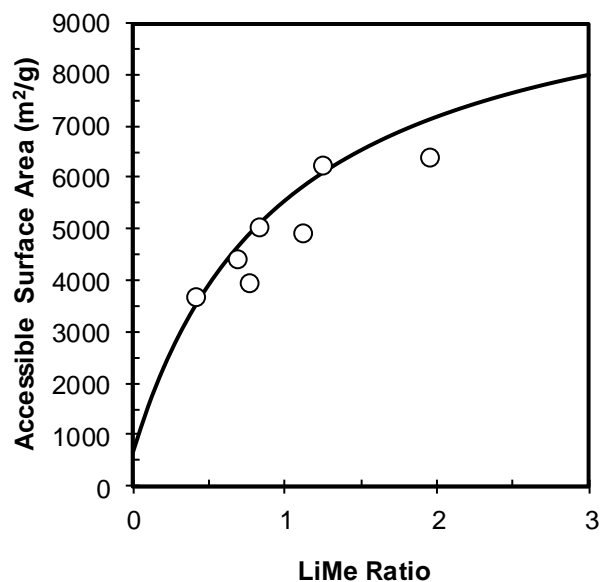
2.3.2. Analysis of MCPs Containing Functionalized Linkers

Another structural effect that can lead to a surface area lower than that predicted from eq 1 is illustrated by inspection of those members of the IRMOF series that consist of structurally related MCPs with various substituents on the benzene ring of MOF-5. Each of these structures has a heavier organic linker and therefore higher LiMe ratio than MOF-5; however, the mass increase is not used to expand the distance between coordinating groups but rather is localized along the linker periphery. This inefficient use of linker mass leads to lower surface areas than predicted by the LiMe ratio (Table 2.2, Figure 2.4). An additional consequence of this type of linker modification is the creation of corner adsorption sites that host fewer adsorbates, on a mass basis, than other sites.[6] This concept is demonstrated by comparison of structural isomers IRMOF-7 and IRMOF-8. Both linkers have the same LiMe ratio of 0.70 with IRMOF-7 containing

napthalene-1,4-dicarboxylate and IRMOF-8 napthalene-2,6-dicarboxylate. The placement of the carboxylates in IRMOF-7 orients the linker so that it protrudes into the open pore and blocks other adsorption sites. Additionally, corner adsorption sites are created from the linker orientation leading to a decrease in geometric accessible surface area from 4393 (IRMOF-8) to 2821 m^2/g. If such underpredictions of surface area by eq 1 are found to be general, additional terms to account for ring fusion, heteroatom and functional group substitutions, and substituent effects could be introduced once a suitable series of structures is studied in order to determine the magnitude of the correction factors.
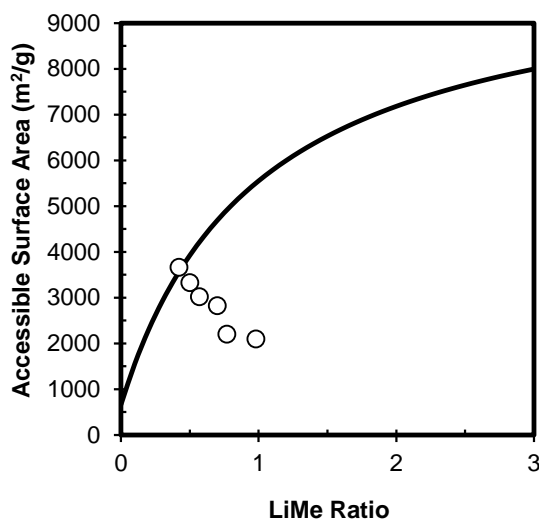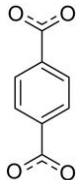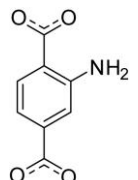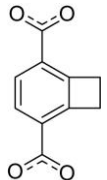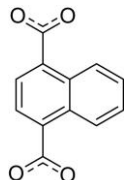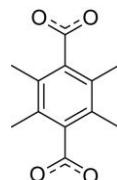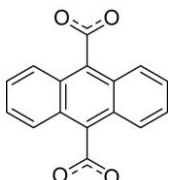
Figure 2.4. Surface areas of MCPs with substituted terephthalic acid linkers and $Zn_4O(CO_2R)_6$ clusters ($\circ$, geometric accessible; ▬, LiMe ratio predicted).

Table 2.2. Surface areas of MCP derivatives of MOF-5 determined through geometric accessible (GA) and LiMe ratio (LiMe) methods.

Linker						
$Zn_4O(CO_2R)_6$ MCP	MOF-5[8]	IRMOF-3[13]	IRMOF-6[13]	IRMOF-7[13]	IRMOF-18[13]	IRMOF-993[17]
LiMe Ratio	0.42	0.50	0.57	0.70	0.77	0.98
SA (LiMe) (m^2/g)	3555	3922	4212	4688	4916	5501
SA (GA) (m^2/g)	3663	3328	3016	2821	2200	2096
% deviation	3	16	33	50	76	90

2.3.3. Comparison to Experimental Values

The value of the LiMe ratio as a predictive tool is demonstrated by comparing experimental surface area values to those computed with eq 1; predicted values show a good match with the experimental surface area of MOF-5 (BET 3800 m^2/g),[18] and taking into account structural features that lead to suboptimal usage of linker mass previously discussed, IRMOF-20 (BET 4024 m^2/g)[19] and MOF-177 (BET 4746 m^2/g)[19] also show suitable agreement. Circumstances where experimental surface areas fall far short from surface area predictions, as in the case of IRMOF-8 (Langmuir 1466 m^2/g),[20] can be readily identified, suggesting that the crystal structure is not a good representation of the material used for gas sorption analysis. Additional evidence has supported this claim for the case of IRMOF-8 where Raman spectroscopy suggests that the structure may exhibit interpenetration.[21] Furthermore, experimental surface areas of IRMOF-10 and IRMOF-16[22] have not even begun to reach their surface area potential, indicating that, at least in this simple cubic series, MCPs possessing long linkers and large pores are vulnerable to structural problems such as interpenetration or framework collapse upon solvent evacuation.

2.4. Analysis of Structures Having the M$_2$(CO$_2$R)$_4$ Metal Cluster

Applying the LiMe ratio approach to M$_2$(CO$_2$R)$_4$ paddlewheel clusters, two series containing ditopic and tritopic linkers were modeled. Two-dimensional sheets with spacing that permits nitrogen adsorption onto both faces of square grid layers were formed through the combination of Cu$_2$(CO$_2$R)$_4$ clusters with linear ditopic linkers

(Figure 2.5). Linker extensions produced MCPs with surface areas expressed by the following equation:

$$\text{surface area (LiMe)}_{M_2(CO_2R)_4} = \frac{10374\left(\dfrac{W_{Li}}{W_{Me}}\right) + 2443\left(\dfrac{303.13}{W_{Me}}\right)}{\dfrac{W_{Li}}{W_{Me}} + 1} \qquad (2)$$
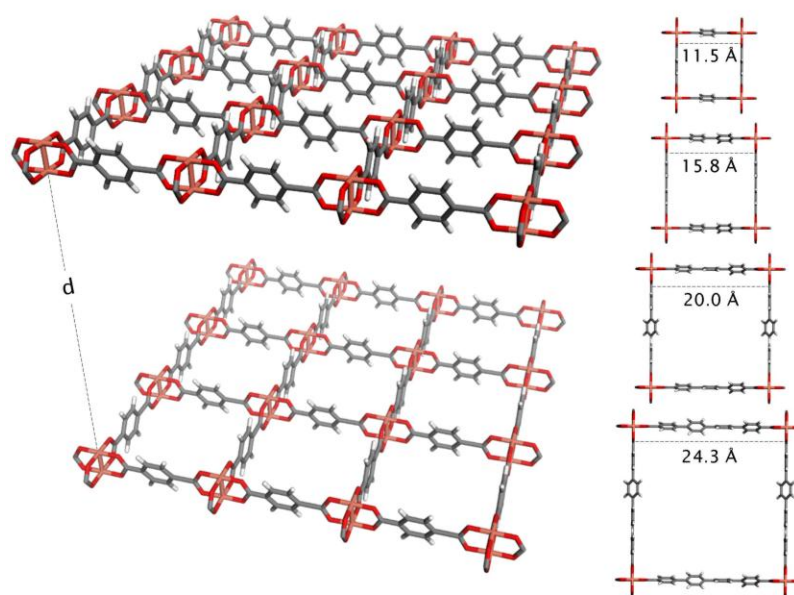
Figure 2.5. Two-dimensional sheets were modeled based upon the combination of linear ditopic linkers and paddlewheel metal clusters. The distance between sheets (d) is 24.6 Å and was arbitrarily chosen to allow nitrogen adsorption onto both faces of sheets. Structures with linkers possessing up to 5 benzene rings were modeled and the geometric accessible surface areas were computed. Values were extrapolated for linkers up to 35 benzene rings.

Structures containing $M_2(CO_2R)_4$ paddlewheel clusters based on a three-dimensional network were built from a model of HKUST-1, incorporating a tritopic linker coordinating to copper paddlewheels (Figure 2.6). Expansions of this linker produced surface areas fit by the following LiMe ratio equation:

$$\text{surface area (LiMe)}_{M_2(CO_2R)_4} = \frac{10295\left(\dfrac{W_{Li}}{W_{Me}}\right) - 714\left(\dfrac{303.13}{W_{Me}}\right)}{\dfrac{W_{Li}}{W_{Me}} + 1} \tag{3}$$
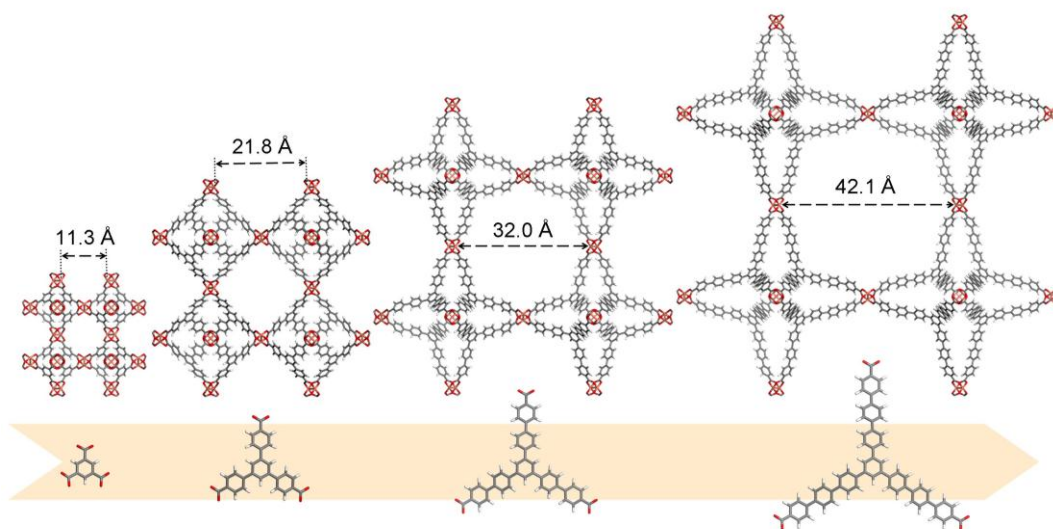
Figure 2.6. Linker extensions of HKUST-1 were modeled for linkers possessing up to 10 benzene rings. Geometric accessible surface areas were computed for these structures and values were extrapolated for structures out to 49 benzene rings per linker.

As for the case of the $M_4O(CO_2R)_6$ series, the surface areas for both paddlewheel series change considerably at low LiMe ratios and approach the surface area of poly(p-phenylene) at higher values (Figure 2.7). Although the shape of each trend is similar, values differ significantly in the low LiMe ratio region (Figure 2.8). Comparing materials

with ditopic linkers, paddlewheels produce higher surface areas for a given LiMe ratio. This can be explained by differences in accessibility of the two geometries of metal clusters; the paddlewheel cluster only accommodates four linkers, leaving more surface available for adsorption compared to the octahedral $M_4O(CO_2R)_6$ cluster. However, because three-dimensional $M_2(CO_2R)_4$ MCPs in general do not derive from linear ditopic linkers, it is more appropriate to use eq 3, based upon coordination of a tritopic linker, for the assessment of paddlewheel clusters. Surface areas for this series are lower than $M_4O(CO_2R)_6$ - ditopic linker values, indicating that both linker and metal cluster geometries play important roles in surface area determination.
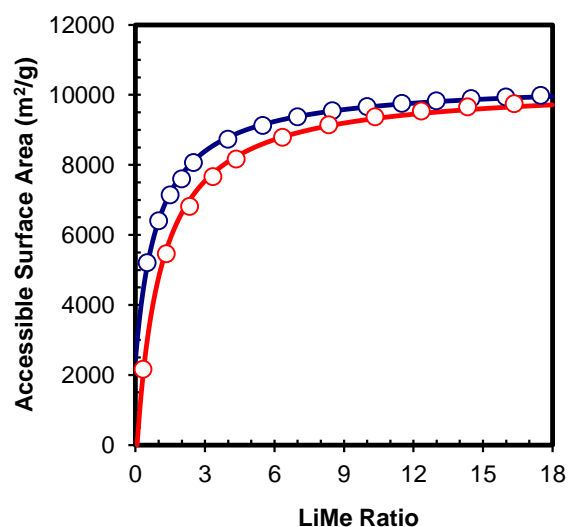
Figure 2.7. Surface areas of MCPs with $Cu_2(CO_2R)_4$ paddlewheel clusters (geometric accessible: ○, ditopic linker; ○, tritopic linker; LiMe ratio predicted: ▬, ditopic linker; ▬, tritopic linker).
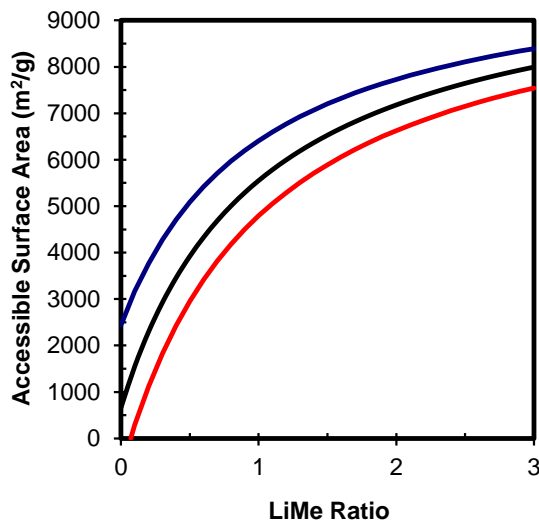
Figure 2.8. Low LiMe ratio region comparing LiMe ratio predicted surface areas (━,
ditopic $Cu_2(CO_2R)_4$; ━, ditopic $Zn_4O(CO_2R)_6$; ━, tritopic $Cu_2(CO_2R)_4$)

2.4.1. Analysis of Benchmark Materials

Surface areas of MCPs with Cu paddlewheel metal clusters are plotted and
compared to LiMe ratio surface area predictions of eq 3 (Figure 2.9, Table 2.3).
Structures with tritopic linkers show excellent agreement between geometric accessible
surface area values and those calculated with the LiMe ratio. The experimental surface
area for HKUST-1 (BET 1944 m^2/g)[19] is similar to its LiMe ratio predicted surface area;
however, structures assembled from larger linkers, PCN-6' (Langmuir 2700 m^2/g)[24] and
MesoMOF-1, do not experimentally meet their surface area potential, suggesting that
poor structural stability may plague materials at LiMe ratios greater than 1.35. MCPs
derived from linkers with more than three carboxylates have lower surface areas due to a
less open pore structure created by those linkers, and these deviations are more

30

significant at lower LiMe ratios. Equation 3 can be used for metal clusters not involving Cu, providing valuable surface area information for MCPs with paddlewheels incorporating Zn and may also be used for Mo or any other metal forming the same cluster.
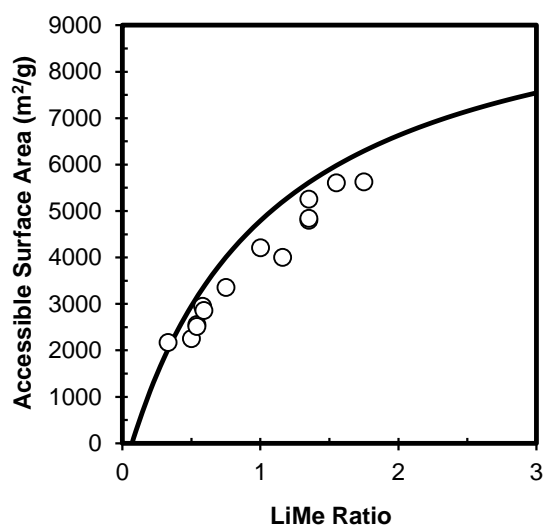
Figure 2.9. Surface areas of MCPs with $Cu_2(CO_2R)_4$ metal clusters ($\circ$, geometric accessible; —, LiMe ratio predicted).

Table 2.3. Comparison of surface areas of MCPs with $Cu_2(CO_2R)_4$ clusters determined through geometric accessible (GA) and LiMe ratio predicted (LiMe) methods.

MCP	# CO_2 groups	LiMe Ratio	SA (LiMe) (m^2/g)	SA (GA) (m^2/g)	% Deviation
HKUST-1[23]	3	0.33	2018	2167	7
PCN-6'[24]	3	1.35	5610	5255	7
MesoMOF-1[25]	3	1.55	5978	5610	6
MOF-HTB'[24]	3	1.75	6292	5625	11
MOF-505[26]	4	0.50	2956	2250	27
PCN-12[27]	4	0.54	3146	2557	21
PCN-12'[27]	4	0.54	3146	2517	22
PCN-11[28]	4	0.58	3327	2949	12
PCN-10[28]	4	0.59	3371	2859	16
NOTT-101[29]	4	0.75	4004	3357	18
NOTT-102[29]	4	1.00	4791	4210	13
$Cu_2(C_{2h}$-tcppda)[30]	4	1.35	5610	4800	16
$Cu_2(D_2$-tcppda)[30]	4	1.35	5610	4840	15
NOTT-112[31]	6	1.16	5198	3999	26

2.4.2. Interpenetration Analysis

Surface areas calculated from the LiMe ratio, with the aforementioned caveats that structural features such as ring fusion, heavy atom inclusion, and substitution can lead to lowered surface areas, may also help indicate interpenetration, another structural feature that prevents an MCP from achieving maximum surface area. Because this type of assembly is typically accompanied by physical contact, surface sites of the linker and/ or metal cluster become inaccessible for guest binding. In many cases, interpenetration has been shown to experimentally stabilize a framework that would otherwise collapse upon guest removal; however, it should not be considered a viable option for increasing absolute surface area. In this context, the case of PCN-6 (Langmuir surface area 3800 m^2/g) and its non-interpenetrated counterpart, PCN-6' (Langmuir surface area 2700

m^2/g), are of particular interest for apparently violating this expectation. Analysis of geometric accessible surface areas for interpenetrated MCPs as a class indicates that they have a much lower surface than is predicted by the LiMe ratio and that none exhibit values greater than the non-interpenetrated structures (Figure 2.10, Table 2.4). PCN-6 and PCN-6' have LiMe ratios of 1.35, which projects a surface area value of 5610 m^2/g. PCN-6' nearly matches this prediction with an accessible surface area of 5255 m^2/g; however, the interpenetrated PCN-6 only displays an accessible surface area of 3970 m^2/g. Therefore, it is likely that the experimental surface area for PCN-6 reaches its surface area potential and that the crystal structure for PCN-6' is not a good representation of material analyzed in gas sorption analysis.
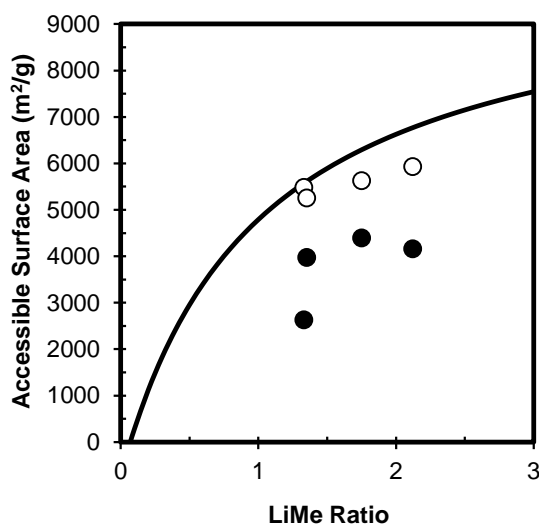
Figure 2.10. Surface areas of MCPs with $Cu_2(CO_2R)_4$ clusters (geometric accessible: ○, noninterpenetrated; ● interpenetrated; ▬, LiMe ratio predicted).

33

Table 2.4. Surface area comparison of interpenetrated and noninterpenetrated MCPs with $Cu_2(CO_2R)_4$ clusters determined through geometric accessible (GA) and LiMe ratio (LiMe) methods.

LiMe ratio	SA (LiMe) (m^2/g)	Noninterpenetrated		Interpenetrated	
		MCP	SA (GA) (m^2/g)	MCP	SA (GA) (m^2/g)
1.33	5570	MOF-14[a32]	5482	MOF-14[32]	2628
1.35	5610	PCN-6'[24]	5255	PCN-6[33]	3972
1.75	6292	MOF-HTB'[24]	5625	MOF-HTB[24]	4394
2.12	6766	Cu_2(Biaryl-TB)[34]	5930	Cu_2(Biaryl-TB[b])[34]	4158

[a]Interpenetration removed in Materials Studio 4.3. [b]Cu_2(Biaryl-TB) = Cu_2(2,2'-diethyoxy-1,1'-binaphthyl-4,4',6,6'-tetrabenzoate)

2.5. Conclusions

In conclusion, the LiMe ratio serves as a tool for understanding surface area in MCPs. Geometric accessible area calculations were employed to build a predictive model that calculates the upper limit of surface area potential based upon molecular weight of building block components. Common experimental barriers such as interpenetration, framework collapse, and phase purity problems can be detected when experimental values deviate significantly from LiMe predictions. Because no structural characterization is required, the LiMe ratio surface area method also serves as a design tool, demonstrating how the factors of linker size, geometry, and number of coordinating groups can affect surface area. This currently represents the quickest and easiest theoretical approach for surface area prediction of MCPs.

2.6. Method

2.6.1. Geometric Accessible Surface Area Determination

Crystal structures were retrieved from the Cambridge Structural Database. CIF files with disorder or guest molecules were modified in Materials Studio 4.3 to mimic a perfectly ordered and guest-free crystal. Hydrogen atoms were placed at calculated positions. Geometric accessible surface areas for these materials were calculated by using the FORTRAN source code for nonorthorhombic cells of Düren.[35] The probe size diameter used for nitrogen was 3.861 Å,[36] and framework atom (H, C, O, N, S, Zn, Cu) diameters were taken from the Dreiding force field,[37] UFF force field,[38] and average van der Waals bond distances[39] (Table 2.5). It was found that slight variations in atomic diameters do not significantly affect the predicted surface area. Densities were calculated using PLATON.[40]

Table 2.5: Diameters of framework atoms of MCPs used in geometric accessible surface area simulations.

Framework Atom	Diameter (Å)
C	3.431[38]
O	3.118[38]
H	2.571[38]
N	3.10[39]
S	3.60[39]
Zn	2.462[38]
Cu	3.11[38]

2.6.2. Surface Area Extrapolation

Models with linker extensions of MOF-5, a two-dimensional $Cu_2(CO_2R)_4$ grid, and HKUST-1 were built in Materials Studio 4.3. As linker size increases, surface area becomes less dependent on pore size and geometry and can be predicted based solely upon the number of benzene units. This was established for the MOF-5 series by converting surface area in terms of m^2/formula unit. The average change in surface area per formula unit was calculated to be 3.97×10^{-18} m^2/formula unit (Table 2.6). This equates to a surface area gain of 1.32×10^{-18} m^2/benzene and is in agreement with the surface area of a benzene unit in poly(p-phenylene) ($1.34 \times 10\text{-}18$ m^2/benzene). This value was used to extrapolate geometric surface areas beyond modeled structures up to a LiMe ratio of 18. All calculated surface areas are summarized in Tables 2.7 ($Zn_4O(CO_2R)_6$ series), 2.8 ($Cu_2(CO_2R)_4$ – ditopic linker series), and 2.9 ($Cu_2(CO_2R)_4$ – tritopic linker series).

Table 2.6. Geometric surface area conversions in MOF-5 extended structures. Surface areas were calculated in terms of m^2/formula unit and the average of these values was used as a standard to calculate surface area changes in structures not capable of being computed directly.

Benzenes per linker	Formula wt. (g/mol)	Geometric Accessible Surface Area (m^2/g)	m^2/ formula unit	Surface area change
6	1911	7679	2.438E-17	
7	2140	7963	2.831E-17	3.92E-18
8	2368	8181	3.218E-17	3.88E-18
9	2596	8418	3.631E-17	4.13E-18
10	2824	8574	4.023E-17	3.92E-18
11	3053	8727	4.426E-17	4.03E-18
12	3281	8849	4.823E-17	3.97E-18

Table 2.7. Surface area equation for MCPs with $M_4O(CO_2R)_6$ clusters (based on MOF-5).

Benzenes per linker	Formula wt. (g/mol)	LiMe Ratio	Geometric Accessible Surface Area (m²/g)	Extrapolated Geometric Accessible Surface Area (m²/g)
1	770	0.42	3663	
2	998	0.84	5011	
3	1226	1.26	6198	
4	1455	1.69	6689	
5	1683	2.11	7217	
6	1911	2.53	7679	
7	2140	2.95	7963	
8	2368	3.37	8181	
9	2596	3.79	8418	
10	2824	4.21	8574	
11	3053	4.64	8727	
12	3281	5.06	8849	
15	3966	6.32		9100
18	4651	7.58		9299
21	5336	8.84		9446
24	6020	10.10		9560
27	6705	11.36		9650
30	7390	12.62		9724
33	8075	13.88		9785
36	8760	15.14		9837
39	9445	16.40		9881
42	10130	17.66		9919

Table 2.8. Surface area equation for MCPs with $M_2(CO_2R)_4$ clusters (based on Cu-2D square grids).

Benzenes per linker	Formula wt. (g/mol)	LiMe Ratio	Geometric Accessible Surface Area (m^2/g)	Extrapolated Geometric Accessible Surface Area (m^2/g)
1	455	0.50	5206	
2	608	1.00	6405	
3	760	1.50	7143	
4	912	2.00	7605	
5	1064	2.49	8065	
8	1521	3.99		8733
11	1977	5.49		9131
14	2434	6.99		9376
17	2890	8.49		9547
20	3347	9.99		9669
23	3804	11.49		9761
26	4260	12.99		9836
29	4717	14.49		9894
32	5173	15.99		9944
35	5630	17.49		9984

Table 2.9. Surface area equation for MCPs with $M_2(CO_2R)_4$ clusters (based on HKUST-1)

Benzenes per linker	Formula wt. (g/mol)	LiMe Ratio	Geometric Accessible Surface Area (m^2/g)	Extrapolated Geometric Accessible Surface Area (m^2/g)
1	403	0.33	2167	
4	708	1.33	5464	
7	1012	2.34	6819	
10	1316	3.34	7663	
13	1621	4.34		8165
19	2230	6.34		8788
25	2838	8.34		9144
31	3447	10.34		9374
37	4056	12.34		9535
43	4665	14.34		9654
49	5273	16.34		9745

2.6.3. Fitting Parameters

Surface areas from Tables 2.7 - 2.9 were fit to the following equation where y = accessible surface area and x = LiMe ratio = W_{Li}/W_{Me}. The metal cluster weight correction factor (z) is formulated in each equation to be the weight of the metal cluster (541.70 for equation **1** and 303.13 for equations **2** and **3**) divided by W_{Me}. Therefore, this correction factor reduces to 1 when $Zn_4O(CO_2R)_6$ and $Cu_2(CO_2R)_4$ are the metal clusters in the MCP used in equations **1** and **2/3**, respectively. Results are summarized below.

$$y = \frac{ax + bz}{x + 1}$$

(**1**) Equation fit to MOF-5 ($Zn_4O(CO_2R)_6$) extensions:

a = 10436 ± 18
b = 665 ± 52
R^2=0.9991

(**2**) Equation fit to $Cu_2(CO_2R)_4$ 2-dimmensional square grids:

$a = 10374 \pm 23$
$b = 2443 \pm 67$
$R^2 = 0.99859$

(**3**) Equation fit to HKUST-1 ($Cu_2(CO_2R)_4$) extensions:

$a = 10295 \pm 47$
$b = -714 \pm 128$
$R^2 = 0.99452$

In cases when the surface area is less than or equal to zero, a nonporous structure is predicted from a linker that is too small to connect metal clusters in a network accessible to the nitrogen probe. Furthermore, because these equations are derived for benzenoid systems the physical significance of a LiMe ratio implying less than one benzene ring is problematic. It might be imagined that a LiMe ratio of zero is equivalent to an oxalate connected metal cluster; however, the LiMe ratio equation subtracts surface area overlap between linker and metal cluster components in the *b* value. At a LiMe ratio equal to zero, the equation underestimates the surface area because it subtracts this correction factor even though the oxalate connected metal cluster structure does not contain a linker that contributes adsorption sites.

2.7. References

(1)   Mueller, U.; Schubert, M.; Teich, F.; Puetter, H.; Schierle-Arndt, K.; Pastré, J. *J. Mater. Chem*. **2006**, *16*, 626-636.

(2)   Kepert, C. J. *Chem. Commun*. **2006**, 695-700.

(3)   Walton, K. S.; Snurr, R. Q. *J. Am. Chem. Soc*. **2007**, *129*, 8552-8556.

(4)   Connolly, M. L. J. *Appl. Crystallogr*. **1983**, *16*, 548-558.

(5)   Rowsell, J. L. C.; Yaghi, O. M. *J. Am. Chem. Soc*. **2006**, *128*, 1304-1314.

(6)   Düren, T.; Millange, F.; Férey, G.; Walton, K. S.; Snurr, R. Q. *J. Phys. Chem. C* **2007**, *111*, 15350-15356.

(7)   Leach, A. R. *Molecular Modelling: Principles and Applications*; Prentice Hall: Harlow, England, 2001.

(8)   Li, H.; Eddaoudi, M.; O'Keeffe, M.; Yaghi, O. M. *Nature* **1999**, *402*, 276-279.

(9)   Han, S. S.; Deng, W. Q.; Goddard, W. A. *Angew. Chem. Int. Edit.* **2007**, *46*, 6289-6292.

(10)   Han, S. S.; Mendoza-Cortes, J. L.; Goddard, W. A. *Chem. Soc. Rev*. **2009**, *38*, 1460-1476.

(11)   Hausdorf, S.;Baitalow, F.; Böhle,T.; Rafaja, D.; Mertens, F.O. R. L. *J. Am. Chem. Soc*. **2010**, *132*, 10978-10981.

(12)   Babarao, R.; Jiang, J. W. *Langmuir* **2008**, *24*, 6270-6278.

(13)   Eddaoudi, M.; Kim, J.; Rosi, N.; Vodak, D.; Wachter, J.; O'Keeffe, M.; Yaghi, O. M. *Science* **2002**, *295*, 469-472.

(14)   Chae, H. K.; Siberio-Pérez, D. Y.; Kim, J.; Go, Y.; Eddaoudi, M.; Matzger, A. J.; O'Keeffe, M.; Yaghi, O. M. *Nature* **2004**, *427*, 523.

(15)   Ockwig. N. W. Development and Illustration of a Unified Conceptual Framework for the Design of Extended Metal Organic Structures. Ph.D. Thesis, University of Michigan, Ann Arbor, MI, **2005**.

(16)   Furukawa, H.; Ko, N.; Go, Y. B.; Aratani, N.; Choi, S. B.; Choi, E.; Yazaydin, E.; Ö.; Snurr, R. Q.; O'Keeffe, M.; Kim, J.; Yaghi, O. M. *Science* **2010**, *329*, 424-428.

(17)   Düren, T.; Sarkisov, L.; Yaghi, O. M.; Snurr, R. Q. *Langmuir* **2004**, *20*, 2683-2689.

(18)   Kaye, S. S.; Dailly, A.; Yaghi, O. M.; Long, J. R. *J. Am. Chem. Soc*. **2007**, *129*, 14176-14177.

(19)   Wong-Foy, A. G.; Matzger, A. J.; Yaghi, O. M. *J. Am. Chem. Soc*. **2006**, *128*, 3494-3495.

(20)   Rowsell, J. L. C.; Millward, A. R.; Park, K. S.; Yaghi, O. M. *J. Am. Chem. Soc*. **2004**, *126*, 5666-5667.

(21)   Siberio-Pérez, D. Y.; Wong-Foy, A. G.; Yaghi, O. M.; Matzger, A. *J. Chem. Mater*. **2007**, *19*, 3681-3685.

(22)   Nelson, A. P.; Farha, O. K.; Mulfort, K. L.; Hupp, J. T. *J. Am. Chem. Soc*. **2008**, *131*, 458-460.

(23)   Chui, S. S. Y.; Lo, S. M. F.; Charmant, J. P. H.; Orpen, A. G.; Williams, I. D. *Science* **1999**, *283*, 1148-1150

(24)) Ma, S. Q.; Sun, D. F.; Ambrogio, M.; Fillinger, J. A.; Parkin, S.; Zhou, H. C. *J. Am. Chem. Soc*. **2007**, *129*, 1858-1859.

(25)   Wang, X. S.; Ma, S. Q.; Sun, D. F.; Parkin, S.; Zhou, H. C. *J. Am. Chem. Soc.* **2006**, *128*, 16474-16475.

(26)   Chen, B. L.; Ockwig, N. W.; Millward, A. R.; Contreras, D. S.; Yaghi, O. M. *Angew. Chem. Int. Edit*. **2005**, *44*, 4745-4749.

(27)   Wang, X. S.; Ma, S. Q.; Forster, P. M.; Yuan, D. Q.; Eckert, J.; López, J. J.; Murphy, B. J.; Parise, J. B.; Zhou, H. C. *Angew. Chem. Int. Edit*. **2008**, *47*, 7263-7266.

(28)   Wang, X. S.; Ma, S. Q.; Rauch, K.; Simmons, J. M.; Yuan, D. Q.; Wang, X. P.; Yildirim, T.; Cole, W. C.; López, J. J.; de Meijere, A.; Zhou, H. C. *Chem. Mater*. **2008**, *20*, 3145-3152.

(29)   Lin, X.; Jia, J. H.; Zhao, X. B.; Thomas, K. M.; Blake, A. J.; Walker, G. S.; Champness, N. R.; Hubberstey, P.; Schröder, M. *Angew. Chem. Int. Edit*. **2006**, *45*, 7358-7364.

(30)   Sun, D. F.; Ke, Y. X.; Mattox, T. M.; Ooro, B. A.; Zhou, H. C. *Chem. Commun*. **2005**, 5447-5449.

(31)   Yan, Y.; Lin, X.; Yang, S. H.; Blake, A. J.; Dailly, A.; Champness, N. R.; Hubberstey, P.; Schröder, M. *Chem. Commun*. **2009**, 1025-1027.

(32)   Chen, B. L.; Eddaoudi, M.; Hyde, S. T.; O'Keeffe, M.; Yaghi, O. M. *Science* **2001**, *291*, 1021-1023.

(33)   Sun, D. F.; Ma, S. Q.; Ke, Y. X.; Collins, D. J.; Zhou, H. C. *J. Am. Chem. Soc*. **2006**, *128*, 3896-3897.

(34)   Ma, L. Q.; Lin, W. B. *J. Am. Chem. Soc*. **2008**, *130*, 13834-13835.

(35)   The source code was downloaded from the following website and compiled with gfortran. http://www.see.ed.ac.uk/~tduren/research/surface_area/non_ortho/

(36)   Bird, R., B.; Steward,W. E.; Lightfoot, E. N. *Transport Phenomena, 2ⁿᵈ ed*.; Wiley: New York, 2002.

(37)   Mayo, S. L.; Olafson, B. D.; Goddard, W. A. *J. Phys. Chem*. **1990**, *94*, 8897-8909.

(38)   Rappe, A. K.; Casewit, C. J.; Colwell, K. S.; Goddard, W. A.; Skiff, W. M. *J. Am. Chem. Soc*. **1992**, *114*, 10024-10035.

(39)   Bondi, A. *J. Phys. Chem*. **1964**, *68*, 441-451.

(40)   Spek, A. L. *PLATON, A Multipurpose Crystallographic Tool*, (Ultrecht University, Ultrecht, The Netherlands, 2005).

CHAPTER 3

A Highly Connected Network for the Stabilization of Non-Interpenetrated Porous Coordination Polymers

3.1. Introduction

Due to their exceptional surface areas, microporous coordination polymers have emerged as a new class of porous materials with potential in applications of gas storage, separations, and selective catalysis.[1,2] Traditional methods for acquiring high surface areas and large porosities have paired large organic carboxylate linkers with relatively lightweight metal ions or clusters. These methods take advantage of large pore sizes and numerous adsorption sites provided by linkers with long spans between coordinating groups and the robust frameworks associated with stable metal clusters such as basic zinc carboxylate or copper paddlewheel units. Limits to this strategy have been encountered due to the tendency for structures to interpenetrate or collapse upon guest removal.[3-5] By examining past examples, it may be possible to gain further insight into the structure-property relationship of coordination polymers in order to design materials that exhibit permanent porosity and high surface areas in a regime of ligand sizes heretofore inaccessible. Examples of state-of-the art strategies and their limitations are presented

below followed by the conceptualization and implementation of an approach to circumvent these classical problems.

3.1.1. Examples of Linker Extension

Large linkers have typically been formed through formal extension from similarly shaped smaller units.[6-8] IRMOF-16,[6] derived from the linear terphenyl dicarboxylate linker, **1**, in Figure 3.1 forms the same cubic network as the terephthalic acid derived MOF-5.[9] The addition of two benzene rings significantly enhances the theoretically attainable surface area to 6146 m^2/g;[10] however, the large pores favor interpenetration, leading to the formation of IRMOF-15. Both of these MCPs lack significant structural integrity and display only minimal surface areas upon guest removal[11] suggesting that the long length and linear geometry of the linker are unfavorable for creating a robust porous material.
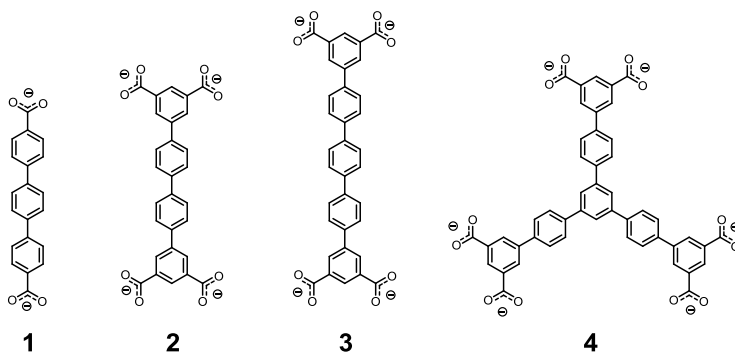
Figure 3.1. Large linkers used in the production of highly porous MCPs.

In considering how to elude structural collapse, isophthalate groups offer considerable promise as coordinating subunits because the additional carboxylates can stabilize even very open networks arising from large linkers by providing framework

reinforcement. The quaterphenyl tetracarboxylate linker, **2**, demonstrates this approach by featuring two sets of isophthalate groups arranged in a linear fashion. Coordination with copper forms a non-interpenetrated MCP, NOTT-102, having the NbO net and a surface area of nearly 3000 m^2/g.[8] Despite the isophthalate units, ever larger linkers having this geometry are still unstable and susceptible to interpenetration; linker extension through addition of a benzene unit to form **3** leads to an interpenetrated NbO net that collapses during activation. Therefore, the geometry of the linker may also play a critical role in forming scaffolds that are both non-interpenetrated and permanently porous. This has been achieved by stabilizing isophthalate groups in a trigonal geometry. Herein the strategy of grafting isophthalate linkages onto a 1,3,5-triphenylbenzene core to yield **4**, a massive seven ring linker reinforced with enough carboxylates to form a highly porous, non-interpenetrated material named UMCM-300 (University of Michigan Crystalline Material - 300) is reported.

3.2. UMCM-300

Aquamarine crystals of UMCM-300 were grown in 61% yield by the solvothermal reaction of linker **4** with $Cu(NO_3)_2 \cdot 2.5H_2O$ and HCl in DMF/DMSO at 85 ºC for 7 days. The mother liquor was then removed and replaced sequentially with DMF and acetone. Thermogravimetric analysis (TGA) of the material revealed rapid solvent loss between 25 and 85 ºC followed by the loss of solvent molecules bound to the Cu atoms at considerably higher temperature. Solvent removal from the bulk material was accomplished under vacuum at 100 ºC for 6h, causing the color of the material to change to deep purple. The partially desolvated material was formulated as

$C_{48}H_{24}O_{12}Cu_3 \cdot 1.5DMF$ by elemental analysis. No substantial change in the PXRD pattern was observed after removal of the solvent.

3.2.1. Structure

The structure of UMCM-300 was solved by single-crystal X-ray diffraction and found to belong to the Fm3̄m cubic space group with $a = 47.305$ Å. Views of the lattice perpendicular to the [100] and the [110] plane are provided in Figures 3.2a-b. Each linker is bound to nine neighboring linkers through three pairs of $Cu_2(CO_2R)_4$ paddlewheel clusters, each pair of Cu clusters binding three neighboring linkers. UMCM-300 derives from a (3,24)-connected net where the carboxylates assemble with the copper ions to form cuboctahedral cages linked together by 24 linkers and 12 Cu clusters (Figure 3.2c). These cages possess triangular apertures of 4.6 Å and circular apertures roughly 7.0 Å in diameter, whereas the cages possess an inner diameter of 13.2 Å. The triphenylbenzene cores of the linkers form two more types of cage-like structures. One cage has a tetrahedral shape with ellipsoidal apertures 7.2×9.7 Å, triangular apertures of 4.6 Å, and an inner diameter of 20.7 Å (Figure 3.2d). The other type of cage is octahedral containing ellipsoidal apertures of 7.2×9.7 Å, circular apertures with a diameter of 7.0 Å, and inner diameters of 25.7 Å (face-face), 33.5 Å (edge-edge) and 37.0 Å (vertex-vertex) (Figure 3.2e). The cuboctahedral cages are located on the vertices of both the tetrahedral and octahedral cages, in which faces are occupied by linker molecules and are shared by both types of cages.

47
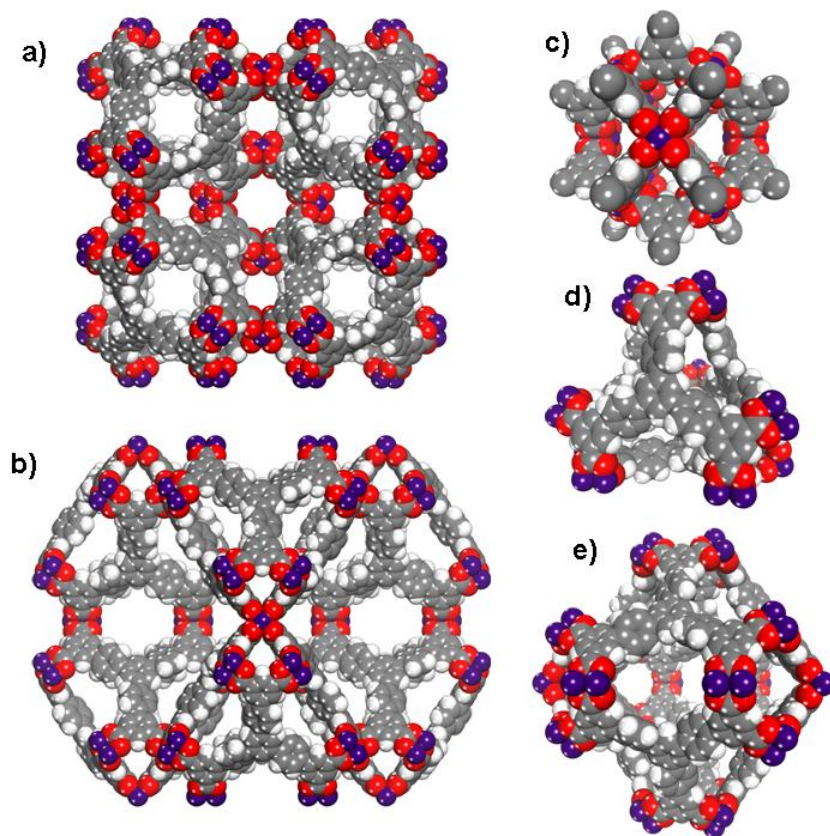
Figure 3.2. (a) View perpendicular to the [100] plane in the crystal structure of UMCM-300 (b) View perpendicular to the [110] plane. (c) Cuboctahedral cage formed by 24 linkers and 12 Cu clusters. (d) Tetrahedral cage formed by 4 linkers and 12 Cu clusters. (e) Octahedral cage formed from 8 linkers and 24 Cu clusters.

3.2.2. Gas Sorption

The N_2 sorption isotherm was recorded at 77 K on a fully evacuated sample of UMCM-300, and revealed a type IV behavior with no hysteresis upon desorption (Figure 3.3). The material shows a minor step at P/P_o = 0.08-0.09 followed by a second step which is indicative of a minor contribution from mesopores. From these data a total pore volume of 1.4 cm^3/g could be measured, and the apparent surface area determined by the BET method is estimated to 3900 m^2/g (4100 m^2/g Langmuir). This is in close agreement with theoretical geometric accessible surface area calculations[10] (3999 m^2/g) and

confirms proper sample activation. A pore size distribution for UMCM-300 was determined from the Ar sorption isotherm at 87 K and revealed the presence of micropores (10.5-11.5 Å and 12.5-13 Å in diameter), along with a smaller distribution of mesopores (21-23 Å in diameter). These pore sizes correspond to the three different types of cages observed in the crystal structure. The excess hydrogen uptake at 77 K was determined to be 6.0 wt % (Figure 3.5).
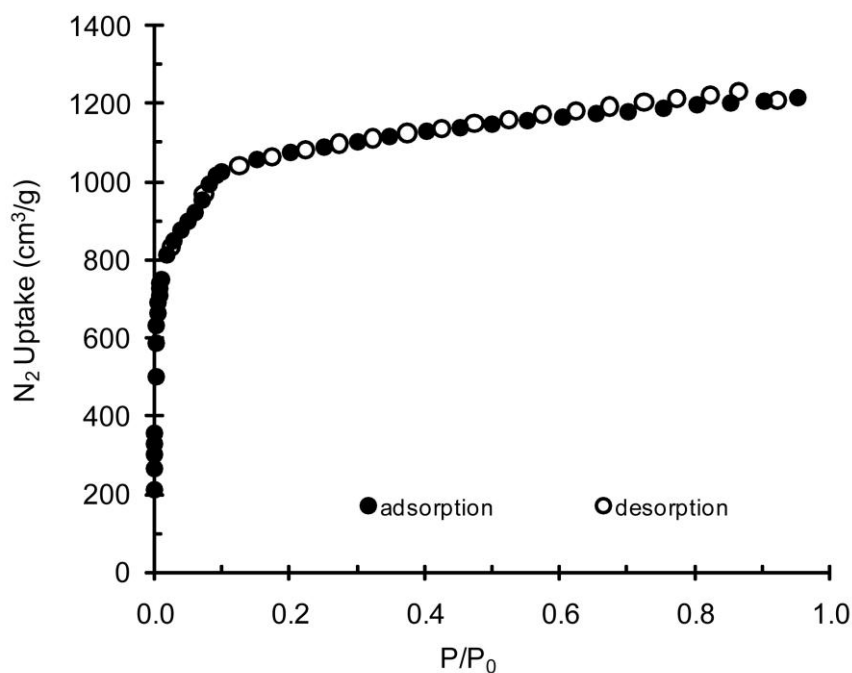
Figure 3.3. Nitrogen sorption isotherm at 77 K for UMCM-300.
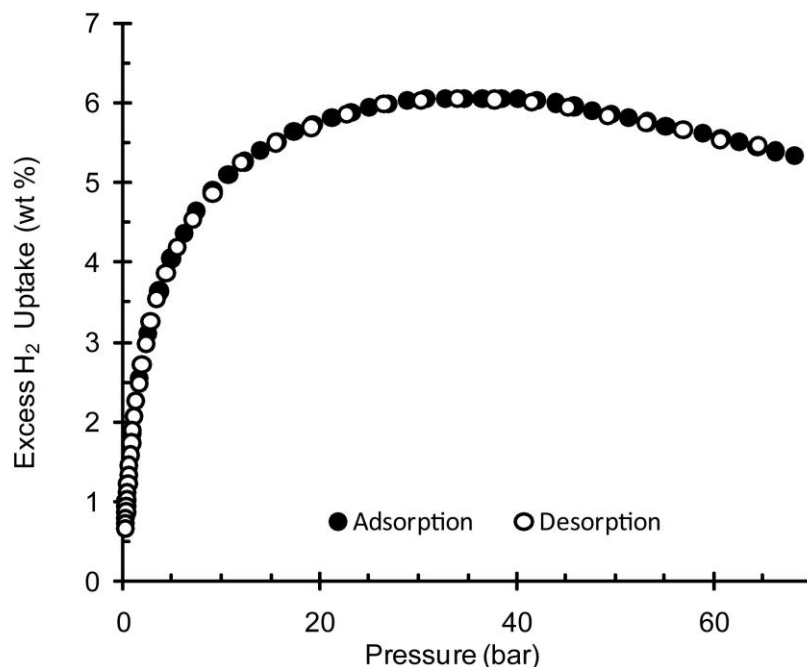
Figure 3.4. Saturation excess hydrogen uptake at 77 K for UMCM-300.

3.3. Universal Properties of Isoreticular MCPs

After the initial synthesis of UMCM-300, several reports of similar and identical MCPs containing (3,24)-connected networks emerged.[12-19] Each of these materials consists of a hexacarboxylate linker coordinating with Cu, Zn, or Co paddlewheels (Figure 3.6). Unlike the isoreticular series derived from linear dicarboxylate linkers connected to basic zinc carboxylate clusters[6] or linear diisophthalate linkers connected to copper paddlewheels,[7-8,20-23] none of the structures in this (3,24)-network series are interpenetrated despite some of them containing relatively large linkers.

The lack of interpenetration is an outstanding feature in this series and can be traced to the network topology.[24] Isophthalate groups coordinate predictably with copper

to form the ubiquitous paddlewheel metal cluster. When arranged linearly, as is the case of linkers **2** and **3**, the NbO net is formed and paddlewheels assemble into a corrugated sheet pattern. Isophthalates that are not linearly disposed are able to form cuboctahedral cages consisting of 24 isophthalate groups coordinating with 12 paddlewheels; therefore, a (3,24)-connected network is formed when these cuboctahedral cages are connected by a trigonal array of isophthalate groups. The cuboctahedral cage contains small pore apertures of approximately 4.6 Å and 7 Å that are too small to allow interpenetration. This general concept has been referred to as framework stabilization by incorporation of "mesocavities with microwindows".[15]
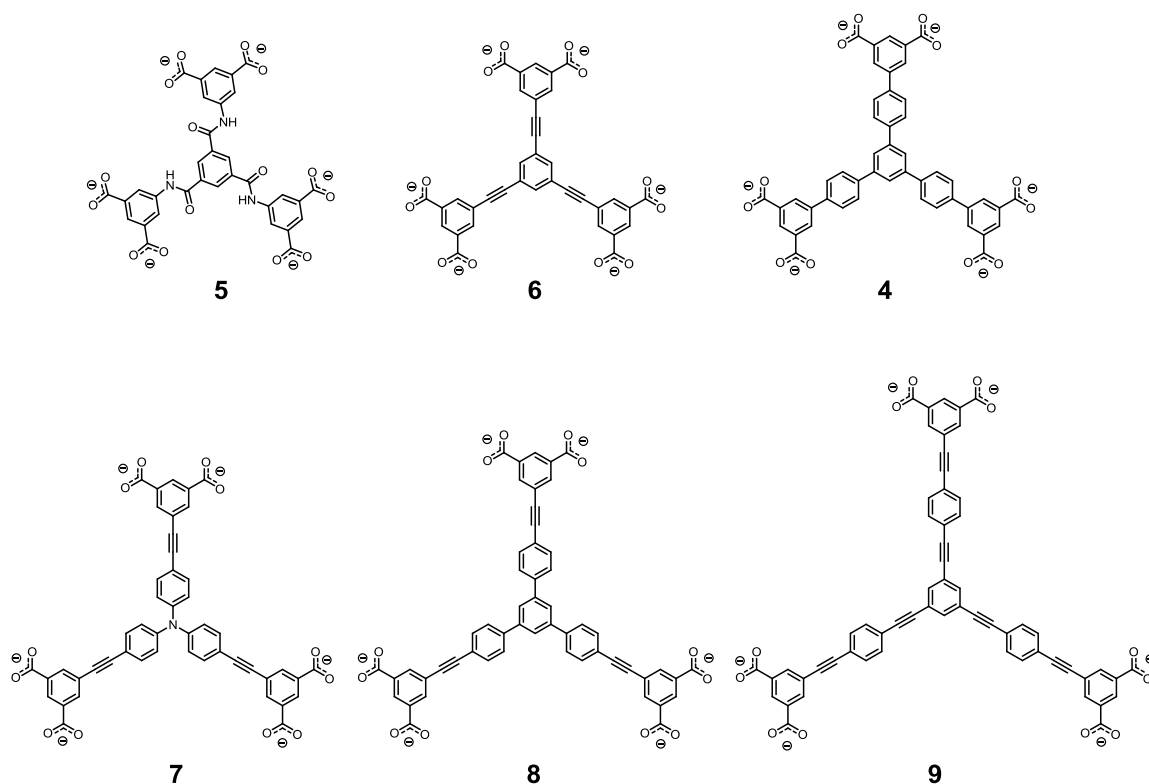
Figure 3.5. Hexacarboxylate linkers that assemble with paddlewheel metal clusters to produce a non-interpenetrated (3,24)-connected network.
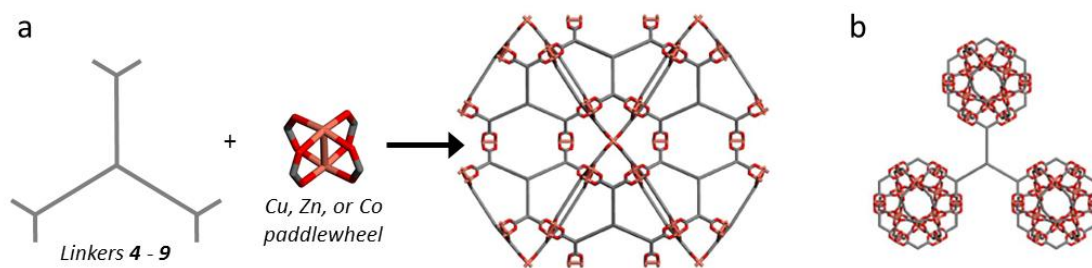
Figure 3.6 (a) General synthesis for the construction of a (3,24)-connected network. (b) A trigonal linker is coordinated to 3 cuboctahedra cages.

Table 3.1. Summary of MCPs derived from hexacarboxylate linkers **1**-**6**. Data includes surface areas and excess H_2 uptakes at 77 K.

Linker	5			6				4		7	8		9	
Name					PCN-60		PCN-61	UMCM-300	NOTT-112	PCN-66	NOTT-116	PCN-68	PCN-610	NU-100
Metal	Zn	Cu	Co	Zn	Zn	Cu	Cu	Cu	Cu	Cu	Cu	Cu	Cu	Cu
BET Surface Area (m^2/g)	--	3160	NA	72	--	3730	3000	3900	3800	4000	4664	5109	--	6143
H_2 uptake (wt %)	--	NA	NA	0.2	--	5	6.24	6	7.07	6.65	6.4	7.32	--	9.95
Reference	12	13	13	14	15	14	15,16	this work	17	15,16	18	16	16	19

Examination of surface areas and excess hydrogen capacities at 77 K tabulated for MCPs with the (3,24)-connected network in Table 3.1 reveals several trends consistent with those found in literature. First, high surface area values are correlated with large hydrogen storage capacities at 77 K. Secondly, structures derived from Zn paddlewheels display nonporous or severely low surface areas suggesting that the Zn paddlewheels do not produce robust structures required for gas sorption. Thirdly, even with independent groups reporting identical materials, surface areas and hydrogen uptakes vary considerably. For example, supercritical carbon dioxide activation was employed to activate NU-100 making it one of the highest surface area materials to date (BET surface area 6143 m^2/g);[19] however, the same structure reported by a different group, PCN-610, displays nonporous behavior using the same activation technique.[16] This inconsistency showcases the field's rapid pace in developing new high performance MCPs and demonstrates the struggle in adapting tools and techniques to properly activate and characterize these new materials. Furthermore, the smaller inconsistencies in reported surface areas and hydrogen uptakes emphasize the difficulty of using proper instrumental techniques and the importance of using consistent methods for interpreting results.[25]

3.4. Conclusion

Stabilization of a large linker with six carboxylate groups has been accomplished by trigonally arranging 3 isophthalate units around a 1,3,5-triphenylbenzene core. This has led to the formation of UMCM-300, in accord with other structures containing hexacarboxylate linkers, that is a member of an isoreticular series of non-interpenetrating

MCPs possessing a (3,24)-connected network. These MCPs are exceptionally porous and display some of the highest surface areas and hydrogen capacities at 77 K to date.

3.5. Experimental Section

3.5.1. Synthesis

1,3,5-tris(4-bromophenyl)benzene was prepared from 4-bromoacetophenone according to a published procedure. Dimethyl isophthalate-5-pinacolboronate was prepared from dimethyl 5-bromoisophthalate (purchased from Matrix Scientific) and bis(pinacolato)diboron (purchased from Combi-Phos) according to the literature. Palladium tetrakis(triphenylphosphine) was purchased from Strem. All other reagents were purchased from Sigma-Alrich or Acros. All reagents and solvents were used as received.

Synthesis of H$_6$**4**: 1,3,5-Tris(4-bromophenyl)benzene (0.980 g, 1.81 mmol), dimethyl isophthalate-5-pinacolboronate (2.08 g, 6.50 mmol), K$_3$PO$_4$ (tribasic, 3.84 g, 18.1 mmol) and 1,4-dioxane (100 mL) were added into a 200 mL round-bottomed flask equipped with a magnetic stirrer and water-jacketed condenser. The resulting suspension was degassed for 15 min. by sparging with nitrogen gas. Pd(PPh$_3$)$_4$ (0.157 g, 0.136 mmol) was added, and the mixture was heated to reflux overnight under a nitrogen atmosphere. After cooling to room temperature, the reaction mixture was poured in H2O (100 mL) and the precipitate was collected by filtration and washed with a minimal amount of THF. The crude material was dissolved in dioxane/H$_2$O (10:1, 110 mL), KOH (1.72 g, 30.6 mmol) was added and the mixture was heated to reflux for 12 h. The solvent was removed by evaporation and the residue was dissolved in H$_2$O (100 mL). The

residual solids were filtered off and the filtrate was acidified with concentrated HCl (20 mL). The target compound was collected by filtration, washed with H_2O and acetone and dried under vacuum to yield 0.783 g of 1 (0.980 mmol as a white powder, 54%): mp >300 °C; IR (KBr) 3423, 3083, 3030, 2924, 1693, 1597, 1516, 1427, 1387, 1317, 1248, 1213, 1138, 1068, 1014, 914 cm-1; ^{1}H NMR (400 MHz, DMSO-d_6): δ 13.39 (s, 6H), 8.43 (s, 3H), 8.42 (s, 6H), 8.04 (d, 3J = 8.2 Hz, 6H), 8.02 (s, 3H), 7.86 (d, 3J = 8.2 Hz, 6H) ppm; ^{13}C NMR (100 MHz, DMSO-d_6): δ 166.9, 141.4, 140.9, 140.3, 138.1, 132.5, 131.6, 129.3, 128.4, 127.8, 124.9 ppm; HRMS (EI) calcd. for $C_{48}H_{30}O_{12}$ (m/z): 798.1737, found: 798.1751.

Synthesis of UMCM-300: Linker **4** (0.36g, 0.45 mmol) and $Cu(NO_3)_2 \cdot 2.5H_2O$ (0.63 g, 2.70 mmol) were added to a solution of 0.01 M HCl in *N,N*-dimethylformamide/dimethylsulfoxide (2:1, 75 mL) and dissolved by sonication. The solution was placed in a tightly sealed 500 mL jar and heated at 85 ºC for 7 days. After cooling, the mother liquor was removed and replaced twice with fresh *N,N*-dimethylformamide and five times with acetone. The solvent was removed under vacuum for 24 h and further dried at 100 ºC for 6 h to yield a dark purple material.

3.5.2.Powder X-Ray Diffraction

Powder X-ray diffraction was performed on a Rigaku R-Axis Spider diffractometer with an image plate detector and Cu Kα radiation operating in transmission mode. The sample was rotated in φ and oscillated in ω to minimize preferred orientation. Diffraction patterns are shown in Figure 3.8.
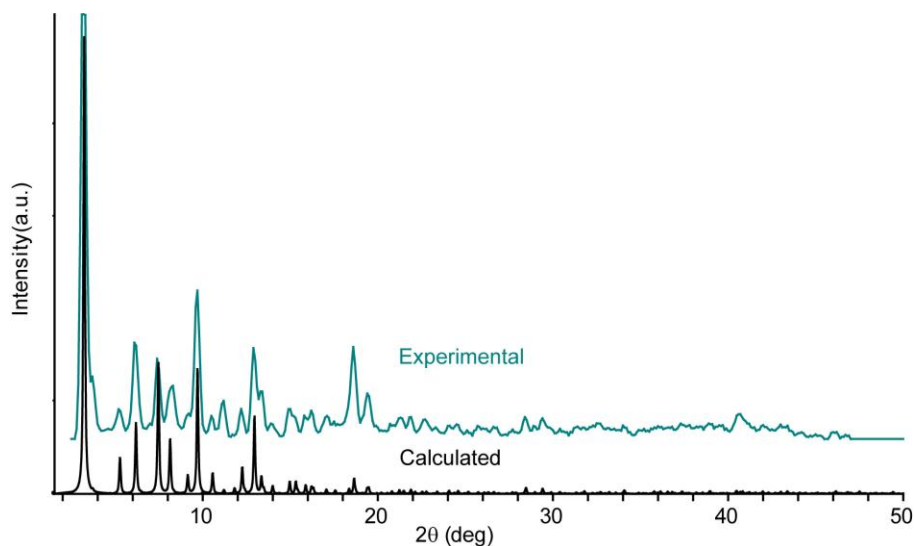
Figure 3.7. Powder X-ray diffraction pattern of UMCM-300.

3.5.3. Gas Sorption

Nitrogen adsorption/desorption isotherms were measured volumetrically at 77 K in the range $1.00 \times 10^{-3} \leq P/Po \leq 1.00$ with an Autosorb-1C outfitted with the micropore option by Quantachrome Instruments (Boynton Beach, Florida USA), running version 1.2 of the ASWin software package. Ultra-high purity He (99.999%, for void volume determination) and N_2 (99.999%) were purchased from Cryogenic Gasses and used as received. MCPs exchanged with acetone were charged into a sample cell and dried under vacuum (< 0.1 mTorr) at 100 °C. The resulting mass of dried material in the cell was ~10 mg.

The Ar adsorption/desorption isotherm was measured similarly. Ultra-high purity Ar (99.999%) was purchased from Cryogenic Gasses and used as received. Pore size distribution was determined by analyzing the Ar isotherm at 87 K using nonlocal density functional theory (NLDFT) implementing a hybrid kernel for argon adsorption at liquid-

argon temperature based on a zeolite/silica model containing cylindrical pores as implemented in the ASWin software package (Figures 3.9-3.10)
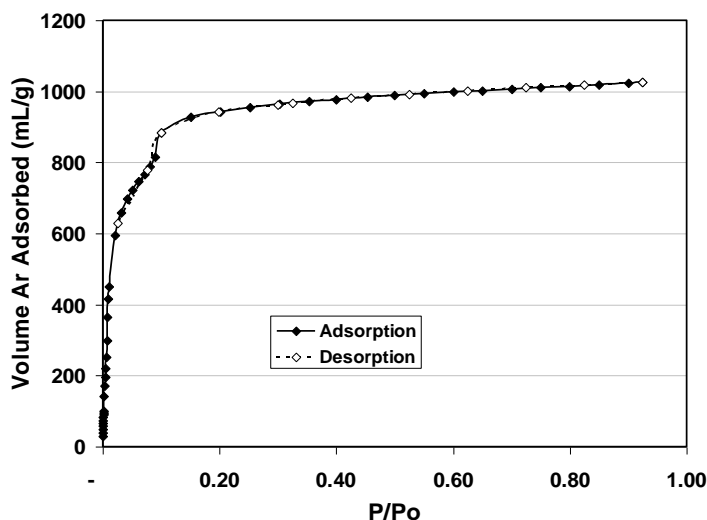
Figure 3.8. Ar sorption isotherm at 87 K for UMCM-300 and the corresponding NLDFT fit based on a cylindrical pore model.
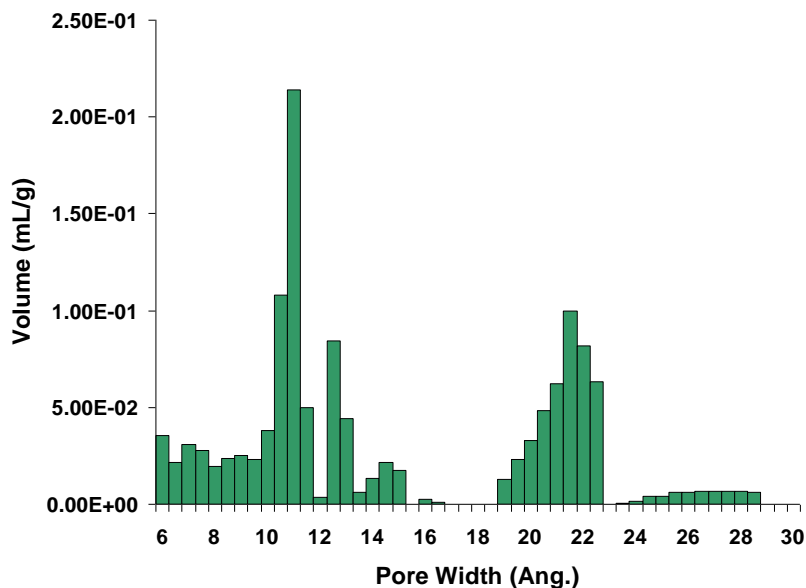
Figure 3.9. Histogram of the pore size distribution for UMCM-300 determined from the Ar sorption isotherm at 87K.

3.5.4. Thermogravimetric Analysis

Measurements were performed on a TA Q50 TGA apparatus. Approximately 10 mg of acetone exchanged material was loaded onto a platinum pan and excess solvent was allowed to evaporate to yield a free flowing powder before starting a temperature programmed ramp (Figure 3.11). Conditions: temperature ramp from 30 – 500 °C at 5 °C/min under a flow of N_2 gas.
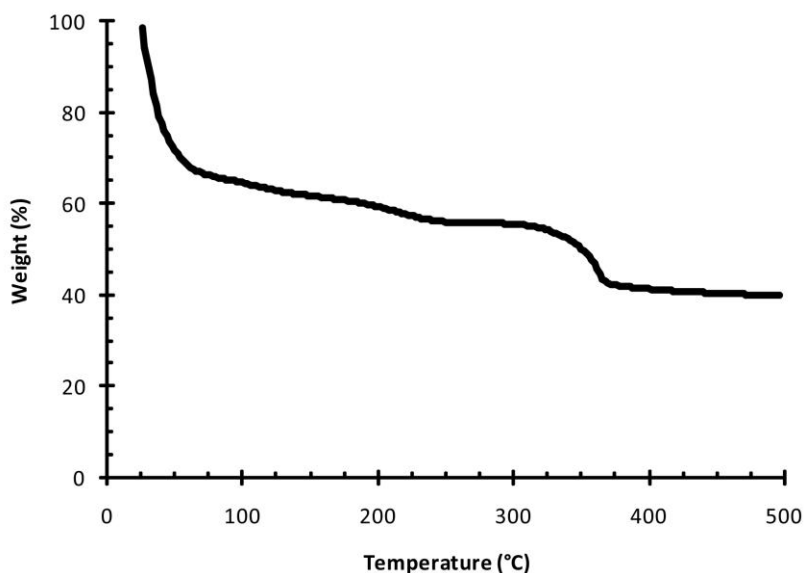
Figure 3.10. TGA trace of UMCM-300.

3.6. References

(1)   Mueller, U.; Schubert, M.; Teich, F.; Puetter, H.; Schierle-Arndt, K.; Pastré, J. *J. Mater. Chem*. **2006**, *16*, 626-636.

(2)   Kepert, C. J. *Chem. Commun*. **2006**, 695-700.

(3)   Nelson, A. P.; Farha, O. K.; Mulfort, K. L.; Hupp, J. T. *J. Am. Chem. Soc*. **2009**, *131*, 458-460.

(4)   Reineke, T. M.; Eddaoudi, M.; Moler, D.; O'Keeffe, M.; Yaghi, O. M. *J. Am. Chem. Soc.* **2000**, *122*, 4843-4844.

(5)   Walton, K. S.; Snurr, R. Q. *J. Am. Chem. Soc*. **2007**, *129*, 8552-8556.

(6)   Eddaoudi, M.; Kim, J.; Rosi, N.; Vodak, D.; Wachter, J.; O'Keefe, M.; Yaghi, O. M. *Science*, **2002**, *295*, 469-472.

(7)   Lin, X.; Jia, J. H.; Zhao, X. B.; Thomas, K. M.; Blake, A. J.; Walker, G. S.; Champness, N. R.; Hubberstey, P.; Schröder, M. *Angew. Chem. Int. Edit*. **2006**, *45*, 7358-7364.

(8)   Lin, X.; Telepeni, I.; Blake, A. J.; Dailly, A.; Brown, C. M.; Simmons, J. M.; Zoppi, M.; Walker, G. S.; Thomas, K. M.; Mays, T. J.; Hubberstey, P.; Champness, N. R.; Schröder, M. *J. Am. Chem. Soc*. **2009**, *131*, 2159-2171.

 (9)   Li, H.; Eddaoudi, M.; O'Keeffe, M.; Yaghi, O. M. *Nature* **1999**, *402*, 276-279.

(10)   Düren, T.; Millange, F.; Férey, G.; Walton, K. S.; Snurr, R. Q. *J. Phys.Chem.C* **2007**, *111*, 15350-15356.

(11)   Nelson, A. P.; Farha, O. K.; Mulfort, K. L.; Hupp, J. T. *J. Am. Chem. Soc*. **2009**, *131*, 458-460.

(12)   Zou, Y.; Park, M.; Hong, S.; Lah, M. S. *Chem. Commun*. **2008**, 2304-2342.

(13)   Zneng, B.; Bai, J.; Duan, J.; Wojitas, L.; Zaworotko, M. J.; *J. Am. Chem, Soc.* **2011**, *133*, 747-751.

(14)   Hong, S.; Oh,M.; Park, M.; Yoon, J. W.; Chang, J.-S.; Lah, M. S. *Chem. Commun*., **2009**, 5397-5399.

(15)   Zhao, D.; Yuan, D.; Sun, D.; Zhou, H.-C. *J. Am. Chem. Soc*. **2009**, *131*, 9186-9188.

(16)   Yuan, D.; Zhao, D.; Sun, D.; Zhou, H.-C. *Angew. Chem. Int. Ed*. **2010**, *49*, 5357-5361.

(17)   Yan, Y.; Lin, X.; Yang, S.; Blake, A. J.; Dailly, A.; Champness, N. R.; Hubberstey, P.; Schröder, M.*Chem.Commun*., **2009**, 1025-1027.

(18)   Yan, Y.; Telepeni, I.; Yang, S.; Lin, X.; Kockelmann, W.; Dailly, A.; Blake, A. J.; Lewis, W.; Walker, G. S.; Allan, D. R.; Barnett, S. A.; Champness, N. R.; Schröder, M. *J. Am.Chem. Soc*. **2010**. *132*, 4092-4094.

(19)   Farha, O. K.; Yazaydin, Ö.; Eryazici, I.; Malliakas, C. D.; Hauser, B. G.; Kanatzidis, M. G.; Nguyen, S. T.; Snurr, R.Q.; Hupp, J. T. *Nature Chemistry*, **2010**, *2*, 944 - 948.

(20)   Chen, B.; Ockwig, N. W.; Millward, A. R.; Consteras, D. S.; Yaghi, O. M. *Angew Chem. Int. Ed*. **2005**, *44*, 4745-4749.

(21)   Ma. S.; Sun, D.; Simmons, J. M.; Collier, C. D.; Yuan, D.; Zhou, H.-C. *J. Am.Chem. Soc.* **2008**, *130*, 1012-1016.

(22)   Wang, X.-S.; Ma. S.; Kauch, K.; Simmons, J. M.; Yuan, D.; Wang, X.; Yildirim, T.; Cole, W. C.; López, J. J.; de Meijere, A.; Zhou, H.-C. *Chem. Mater*. **2008**, *20*, 3145-3152.

(23)   Lee, Y.-G.; Moon, H. R.; Cheon, Y. E.; Suh, M. P. *Angew, Chem. Int. Ed*. **2008,** *47*, 7741-7745.

(24)   Eddaoudi, M., Nouar, F., Eubank, J. F., Wojtas, L., Bousquet, T., and Zaworotko, M. Supramolecular assemblies and building blocks. U.S. Pat. Appl. 20090143596 A1, filed November 17th **2008**

(25)   Walton, K. S.; Snurr, R. Q. *J. Am. Chem. Soc*. **2007**, *129*, 8552-8556.

CHAPTER 4

Linker-Directed Vertex Desymmetrization for the Production of Coordination Polymers with High Porosity

4.1. Introduction

A revolution in the production of new porous materials has come in the last decade due to the development of crystalline microporous coordination polymers (MCPs) as a potentially viable alternative to traditional zeolite and carbonaceous sorbents. Surface areas exceeding 3000 m^2/g have been reported for numerous MCPs[1-16] and values exceeding 5000 m^2/g are now obtainable.[4,14-16] This has been achieved almost exclusively using the traditional paradigm of a single symmetrical linker joined by a single metal cluster. Recently the potential of reduced symmetry linkers has been demonstrated; having one type of coordinating group in different chemical environments offers the potential to expose new regions of phase space ultimately enabling the discovery of novel materials.[17-21]

4.1.1. Reduced Symmetry Linkers

Inspiration for reduced symmetry linkers is derived from the strategy of linker extension. Symmetrical linker extension has been established as a general method for the synthesis of new MCPs, with some materials having the same network topology as their unextended frameworks and others forming entirely new structures. However, this strategy can be limiting due to the tendency of larger linkers to form structures that interpenetrate or collapse upon guest removal.[22-24] By removing the constraint of retaining a fully symmetric linker, two conceptual pathways for the production of new linkers can be envisaged: ring addition, in which the shape of a linker is only partially extended, and carboxylate addition/rearrangement, where the size and core connectivity of the linker remains unchanged but the addition and/or rearrangement of carboxylate groups produces more than one symmetry inequivalent coordinating group (Figure 4.1). Both methods introduce new types of building blocks and therefore expand the library of linkers available for coordination to a metal for the formation of new MCPs.
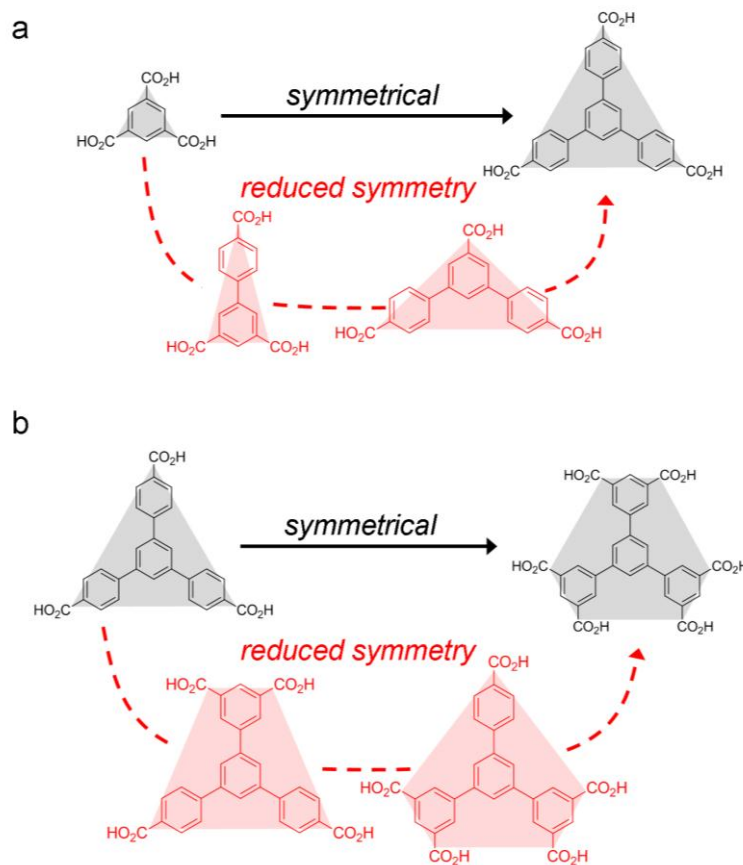
Figure 4.1: Conceptual modification of linkers through (a) ring and (b) carboxylate addition.

A potential benefit of using reduced symmetry linkers is the suppression of framework interpenetration. In considering general routes to porous solids, the tendency of many building blocks derived from a single symmetric linker to make interpenetrated coordination polymers must be explained. Here network topology analysis provides insight. Regular polyhedra are convex polyhedrons that have identical faces derived from equivalent regular polygons and identical vertices assembled from a single type of polygon. There are exactly five such solids: the cube, tetrahedron, octahedron, dodecahedron, and icosahedron.[25,26] On the other hand, semiregular solids (13 in all) are convex polyhedra that have two or more different types of regular polygons as faces with

all sides of the same length, and arranged in the same way about each vertex.[26,27] Such network substructures readily arise from high symmetry linkers coordinating to symmetric metal clusters because there exists only a single distance between coordinating groups. Reduced symmetry linkers will generally not form cage structures whose shapes are those of regular or semiregular polyhedra; a result of the non-uniformity of distances between coordinating groups. This will promote the formation of highly porous materials because the networks lack the appropriate symmetry for self-interpenetration.

Linker symmetry reduction was recently disclosed with the report of University of Michigan Crystalline Material (UMCM)-150 which incorporates a C_{2v} symmetric linker, biphenyl-3,4',5-tricarboxylate (**1**).[17] This was the first porous material derived from a linker containing only chemically inequivalent carboxylates with distinct coordination environments. Two types of metal clusters are formed upon coordination of **1** (Figure 4.2) with copper, $Cu_2(CO_2R)_4$ paddlewheels and $Cu_3(CO_2R)_6$ trigonal prismatic clusters. The presence of the trinuclear Cu cluster in UMCM-150 is remarkable considering it had not been previously formed in an MCP and because the paddlewheel is by far the most commonly formed metal cluster involving carboxylate coordination. Consequently, the structure of UMCM-150 is a non-interpenetrated (3,4,6)-connected network with a BET (Brunauer-Emmett-Teller) surface area of ~3000 m^2/g. The topological complexity in UMCM-150 is attributed to the symmetry of linker **1** which drives the formation of a new network needed to fulfill the enthalpic requirements imposed by a unique linker geometry. However, with only one example, it is difficult to generalize as to the behavior of reduced symmetry linkers in the formation of coordination polymers. Here five

examples of MCPs are presented to allow assessment of the general utility of this linker design strategy.
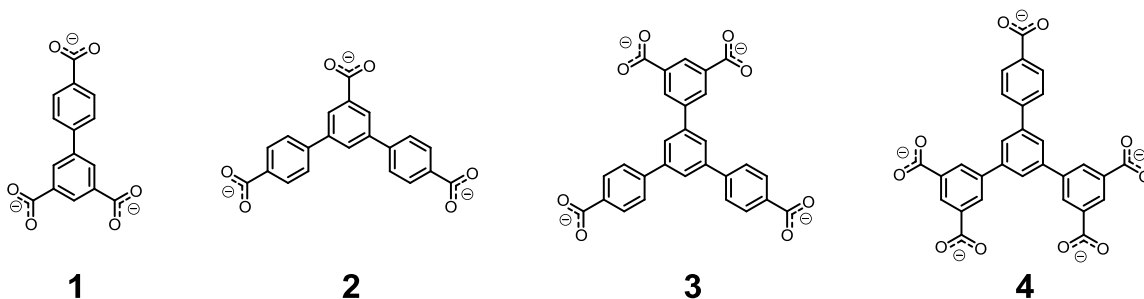
Figure 4.2. Reduced symmetry linkers forming MCPs.

4.2. Results and Discussion

4.2.1. UMCM-150

Among the important findings that arose from the synthesis of UMCM-150 was an uncommon structural motif. In addition to the ubiquitous $Cu_2(CO_2R)_4$ paddlewheel, a trinuclear cluster with the formula $Cu_3(CO_2R)_6$ was found (Figure 4.3a). In this structure, all paddlewheels arise from isophthalate coordination connected through corrugated sheets joined by coordination of *p*-benzoate groups forming trinuclear clusters. Each $Cu_3(CO_2R)_6$ cluster forms a trigonal prismatic geometry orienting six p-benzoate groups along the *c*-axis (Figure 4.3b). There are three times as many paddlewheels as trigonal prismatic clusters.
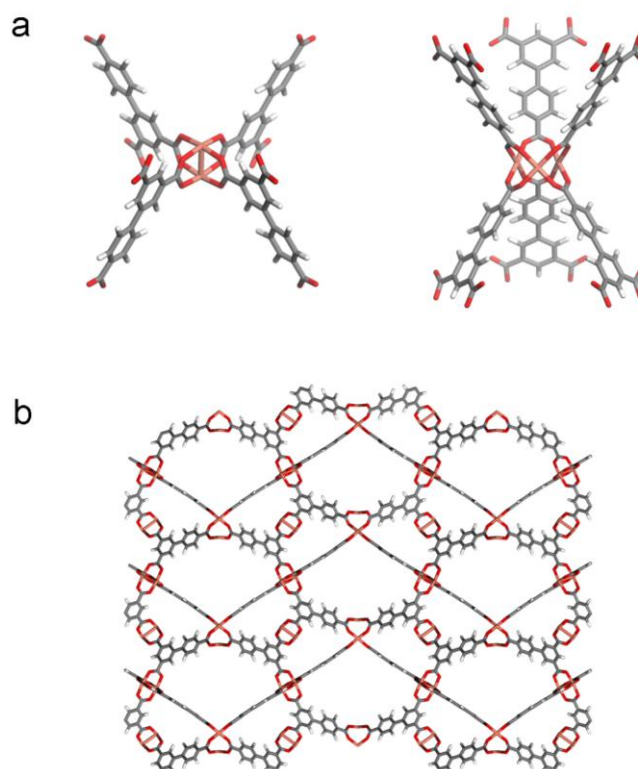
Figure 4.3: (a) View of the $Cu_2(CO_2R)_4$ paddlewheel and $Cu_3(CO_2R)_6$ trigonal prismatic clusters present in UMCM-150. (b) View of the network connectivity along the *a*-axis of UMCM-150.

Although the $Cu_3(CO_2R)_6$ cluster was unprecedented in coordination polymers, the formation can be rationalized by the 1:2 ratio of symmetry inequivalent carboxylates of **1** dictating that one type of paddlewheel, having a capacity for four carboxylate groups, cannot exclusively form within a structure. Consequently, if a paddlewheel is formed, another metal cluster (symmetry inequivalent paddlewheel or different cluster geometry) must also be present. In this case, segregation occurs among the chemically distinct carboxylates with isophthate carboxylates assembling into Cu paddlewheels and *p*-benzoate groups forming a new mode of assembly, a $Cu_3(CO_2R)_6$ cluster.

4.2.2. UMCM-151

Extension of **1** through the addition of a benzene ring leads to linker **2** and assembly of this linker with Cu produces UMCM-151. This structure does not share the same net as UMCM-150 even though **2** possesses the same number of carboxylates and C_{2v} symmetry as linker **1**. Monocarboxylated rings are present with *p*-benzoate groups attached to a central benzene ring possessing a carboxylate in the 5-position (herein referred to as *m*-carboxylate), thus changing the distance between nodes and angles of extension between coordinating groups of the linker and allowing a new structure to form. Similar to the case with linker **1**, the 1:2 ratio of carboxylate types in **2** prevents a single kind of Cu paddlewheel cluster from forming. Segregation based upon carboxylate symmetry is also observed; however, in the case of UMCM-151, two different paddlewheels are present, with *p*-benzoate groups forming one type of paddlewheel and *m*-carboxylate groups of **2** forming a separate paddlewheel (Figure 4.4a). There are twice as many paddlewheels based upon *p*-benzoate coordination as *m*-carboxylate coordination in order to satisfy the stoichiometric number of carboxylates of linker **2**.
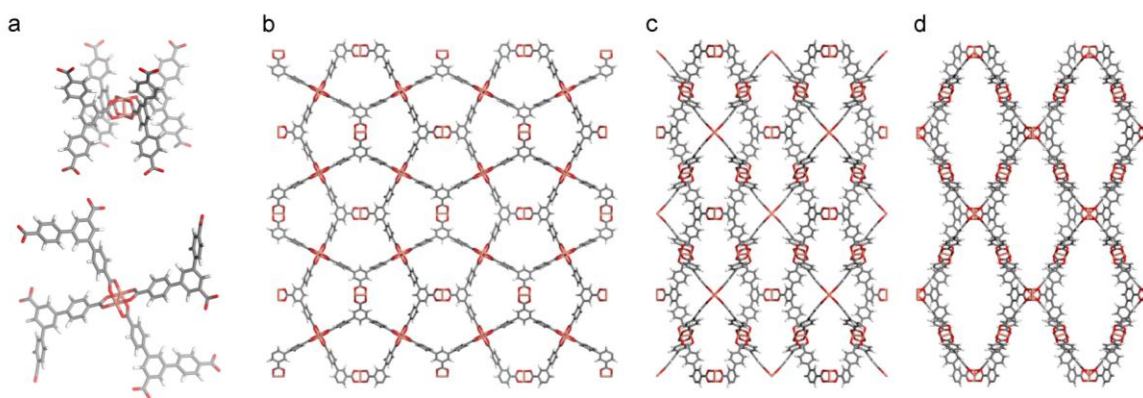
Figure 4.4: (a) Separate Cu paddlewheels are formed through the coordination of four *m*-carboxylate groups and four *p*-benzoate groups in UMCM-151. (b) View of the pentagonal channels along the *a*-axis. (c) View along the *b*-axis in UMCM-151. (d) View along the *c*-axis featuring 3 nm oblong-shaped channels.

UMCM-151 consists of a non-interpenetrated open-pore network crystallizing in the space group *Immm*. A view along the *a*-axis reveals pentagonal-shaped channels with dimensions, accounting for van der Waals radii, of 11.4 × 9.6 Å formed through the connection of three *p*-benzoate groups and two *m*-carboxylate groups coordinated through a Cu-paddlewheel (Figure 4.4b). These are intersected by another set of pentagonal channels (11.3 × 6.9 Å) defined by four *m*-carboxylate units and four *p*-benzoate groups coordinated with four Cu clusters along the *b*-axis (Figure 4.4c). The largest channels within UMCM-151 are oblong with pore dimensions of 28.4 × 11.0 Å spanning the c-axis (Figure 4.4d).

Attempts to activate UMCM-151 by heating under reduced pressure led to surface areas much lower than theoretical values predicted by the LiMe ratio surface area analysis[28] (4791 m^2/g) and geometric accessible surface area method[29] (4493 m^2/g). Examination of the PXRD pattern after solvent removal indicates significant loss of crystallinity consistent with structural collapse. The 3 nm channels within UMCM-151 may ultimately be responsible for this collapse, suggesting that three carboxylate groups cannot provide enough junction points for the *m*-terphenyl linker, **2**, to coordinate with Cu paddlewheels in a stable conformation.

4.2.3 UMCM-152 & UMCM-153

In considering how to overcome the problem of low structural rigidity in UMCM-151, inspiration is derived from isophthalate-based MCPs and especially those possessing a ratio of benzene rings to carboxylates of 1 or greater.[7,9,12,15,30] To implement this design while maintaining reduced symmetry, **3** was considered as a C$_{2v}$ tetracarboxylate precursor. This ligand can be conceptually derived from 1,3,5-tris(4-

carboxyphenyl)benzene by replacing one phenyl carboxylate with an isophthalate group. Gratifyingly this ligand led to two non-interpenetrated coordination polymers that both maintain porosity.

Solvothermal synthesis in a solution of 4:1:1 DMF/dioxane/H_2O with H_4-**3** and $Cu_2(NO_3)_2 \cdot 2.5H_2O$ affords a mixture of blue block-shaped crystals of UMCM-152 and blue blade-like crystals of UMCM-153. UMCM-152 can be formed as a pure phase through the addition of 0.005 M HCl to the reaction solution and UMCM-153 can be produced pure from a mixture of 4:1:1 N-methyl-2-pyrrolidone (NMP)/dioxane/H_2O.

A key distinction between UMCM-152 and UMCM-153 is the pattern of carboxylate coordination to form Cu paddlewheels. Linker **3** contains two pairs of chemically equivalent carboxylates: an isophthalate group and two *p*-benzoate units. Therefore, carboxylate segregation may occur, as in the cases of UMCM-150 and UMCM-151, or chemically inequivalent carboxylates may blend to form one or more types of mixed carboxylate paddlewheels. Single crystal X-ray analysis reveals that both materials feature one unique paddlewheel containing two carboxylates of each type; however, the arrangement of these groups is very different. In UMCM-152, two isophthalate carboxylates assemble in adjacent positions joined by two adjacent p-benzoate groups whereas coordination of chemically inequivalent units alternates in UMCM-153 (Figure 4.5). Consequently, the differences in paddlewheel coordination prompt the formation of two distinct structures, but because they have the same building block components, UMCM-152 and UMCM-153 are polymorphic frameworks.[31] Although several examples have been generated from fully symmetric linkers,[18,31-34] reduced symmetry linkers offer significantly more assembly modes because both linker

orientation and inequivalent carboxylate coordination can produce diverse networks from the same linker and metal cluster.
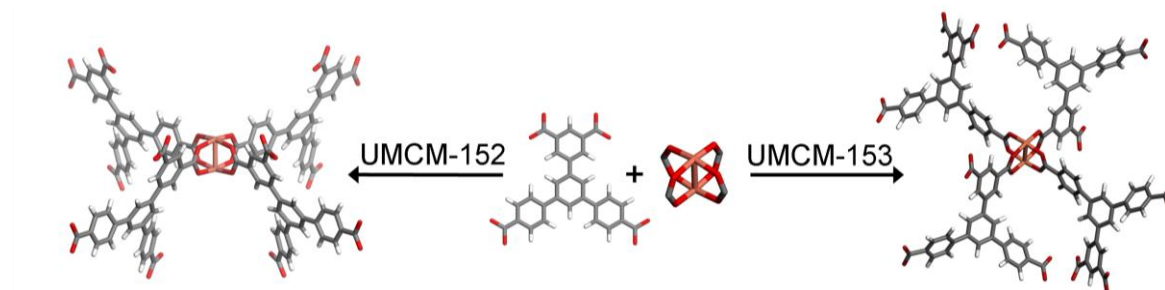
Figure 4.5 Coordination of linker **3** with Cu to form paddlewheels. Adjacent coordination of two equivalent carboxylates leads to the formation of UMCM-152 whereas an alternating pattern of carboxylate types leads to UMCM-153.

The structure of UMCM-152 belongs to the space group R3m and consists of two types of alternatively stacked cages. The first cage is defined by the faces of six linker molecules and twelve metal clusters to form a distorted hexagonal bipyramid with pore apertures of approximately 7.5 Å (Figure 4.6a). Apical positions are occupied by a set of three isophthalate groups coordinated to three paddlewheels with small cylindrical pores of 4.1 Å and a set of six *p*-benzoates coordinating to three paddlewheels with a larger pore size of 10.6 Å. Coordination in the equatorial region of this cage consists of an alternating pattern of two *p*-benzoate groups and isophthalates joined to six paddlewheel clusters. The inner diameter of this cage is approximately 18.6 Å. A second cage is formed from the edges of twelve linkers and six Cu paddlewheels (Figure 4.6b). Apical positions and pore apertures are shared with the first cage and the inner diameter of this cage is 16.9 Å. A view down the *a*-axis and *c*-axis are provided (Figure 4.6c and Figure 4.6d) as well as a view of the 302 plane (Figure 4.6e) highlighting the two cages present in UMCM-152.

UMCM-153 crystallizes in the space group *Fddd*. Hexagonal channels align along the *a*-axis producing cylindrical pores of 8.7 Å (Figure 4.6f). These channels are formed through the stacking of cages defined by the faces of four whole linkers and the edges of four isophthalate groups and two sets of *m*-terphenyl linked *p*-benzoate fragments joined by twelve Cu paddlewheels. The inside of each cage possesses four coordinatively unsaturated metal sites which are oriented towards the center of the hexagonal channel. A view of the 470 plane (Figure 4.6g) displays the channel walls defined by the faces of linker 3. The connection of two isophthalate groups and four p-benzoate groups produce an intersecting channel with dimensions of 15.0 × 4.4 Å (Figure 4.6h).
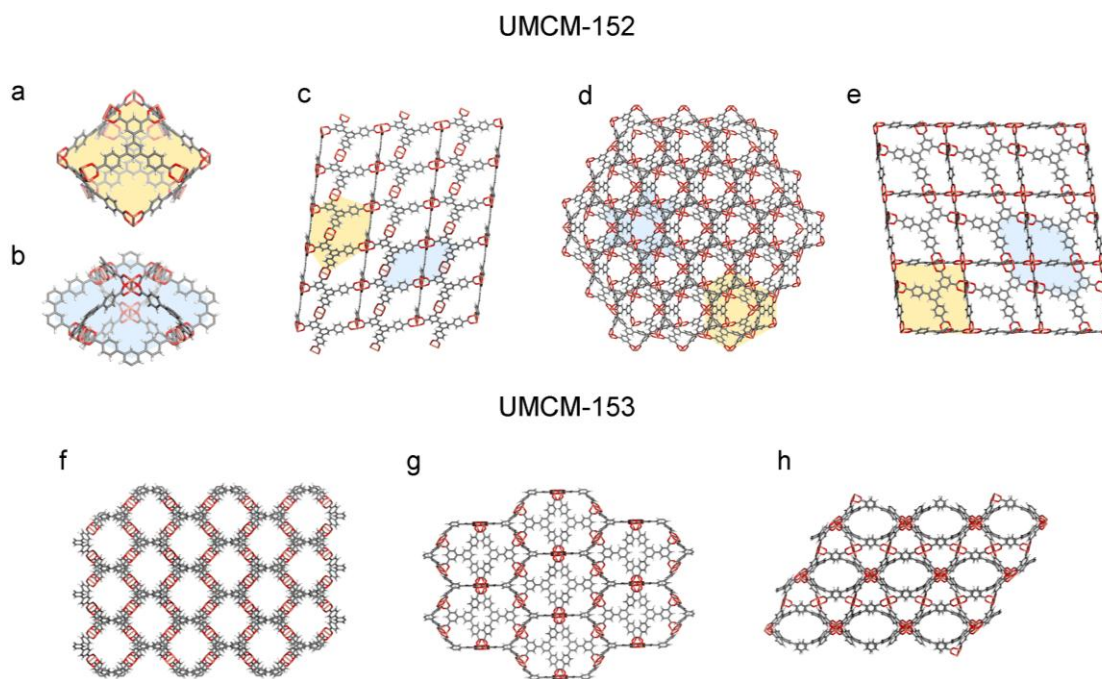
Figure 4.6: (a) One cage in UMCM-152 is defined by the faces of six linkers and twelve Cu-paddlewheels to form a distorted hexagonal bipyramid. (b) Another cage is formed through by the edges of twelve linkers and six Cu-paddlewheels. (c) View along the *a*-axis. (d) View along the *c*-axis. (e) View of the 302 plane of UMCM-152. (f) View along the *a*-axis of UMCM-153 featuring channels aligned with coordinatively unsaturated metal sites. (g) View of the channel walls of the 470 plane. (h) Intersecting elliptical channels in the 104 plane in UMCM-153.

The surface areas of UMCM-152 and UMCM-153 were determined from N_2 adsorption isotherms at 77 K revealing that UMCM-152 has a BET surface area of 3480 m^2/g (Langmuir 3850 m^2/g) and UMCM-153 has a value of 3370 m^2/g (Langmuir 3730 m^2/g) (Figure 4.7a) and these values are in good agreement with geometric accessible surface area predictions. Pore size distributions were determined with NLDFT calculations from Ar adsorption isotherms at 87 K corresponding to pore sizes of 8-10 and 10-11.5 Å for UMCM-152 and of 7–10.5 and 10.5-11.5 Å for UMCM-153; these ranges are consistent with crystallographic data. A small distribution of 40.5–46.0 Å is also found in UMCM-153 signaling either a deficiency in applying the NLDFT model to the irregular pore shape of UMCM-153 or defects within the material as has previously been found in MOF-5.[35] The excess hydrogen uptake for UMCM-152 at 77 K and 25 bar is 5.7 %. This value is similar to the capacity of UMCM-153, 5.8 % at 77 K and 29 bar, indicating that UMCM-152 and UMCM-153 have similar gas sorption properties despite differences in pore shape (Figure 4.7b). Considering identical linker and metal cluster components and similarities in surface area, differences in sorption properties in UMCM-152 and UMCM-153 might be expected to arise when guest size more closely matches pore dimensions; this hypothesis motivated us to examine larger guest inclusion of the sort that can be realized in liquids.[36]
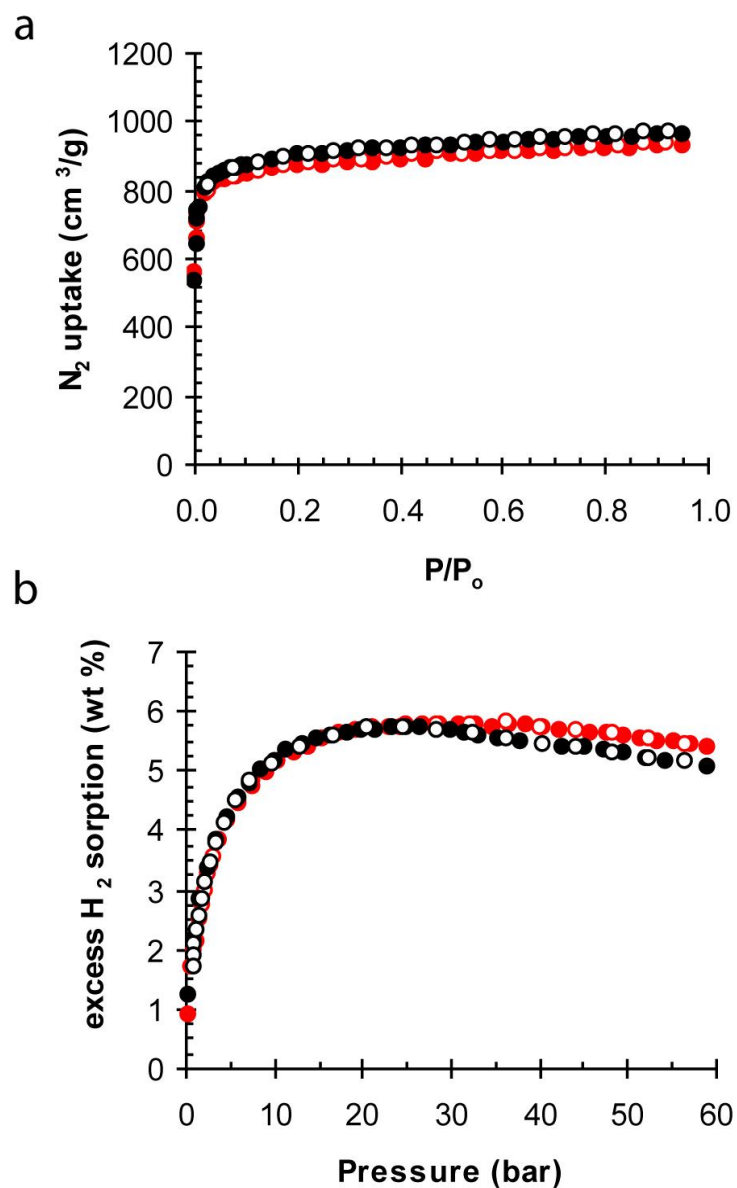
Figure 4.7: (a) Nitrogen sorption isotherms at 77 K for UMCM-152 (black) and UMCM-153 (red) (b) High pressure excess hydrogen isotherms at 77 K (closed markers: adsorption, open markers: desorption).

Recently MCPs have been shown to remove organosulfur compounds from model fuels and diesel representing an efficient method for reaching new sulfur level targets in diesel and gasoline set by the U.S. Department of Transportation.[37,38] UMCM-152 and

UMCM-153, having the same building block units and nearly identical surface areas, offer an opportunity to study the effect of framework structure in the absence of variation in linker or metal cluster. Adsorption isotherms were measured out to 2000 ppmw S for dibenzothiophene (DBT) (Figure 4.8a) and to 600 ppmw S for 4,6-dimethyldibenzothiophene (DMDBT) (Figure 4.8b) in isooctane. UMCM-152 and UMCM-153 exhibit tremendous capacities for DBT and DMDBT: DBT capacities (g S/kg MCP, 1500 ppmw S) are 59 and 89 and DMDBT capacities (g S/kg MCP, 600 ppmw S) are 82 and 40, respectively. These values exceed considerably those of published MCPs. The dramatic differences in capacity of DBT and DMDBT in UMCM-152 and UMCM-153 provide indisputable evidence that liquid phase adsorption is not dependent on surface area or linker or metal cluster identity. Moreover, this constitutes a unique case where the equilibrium adsorption capacity for large molecules in the liquid phase can be directly credited to effects of pore size and shape[38,40] UMCM-153 adsorbs more DBT than UMCM-152 over the entire concentration range examined likely due to a better fit of DBT in the pores of UMCM-153. At low DMDBT concentrations UMCM-153 again outperforms UMCM-152. However, at higher concentrations where the uptake of UMCM-153 begins to level off, the UMCM-152 isotherm continues to rise, leading to higher adsorption capacities at high DMDBT concentration than for UMCM-153. It is postulated that at higher DMDBT concentrations the larger DMDBT molecules begin to block further uptake in the smaller UMCM-153 pores. In contrast, the larger pores of UMCM-152 can readily accommodate the DMDBT molecule in such a way such that the pore apertures are not blocked for further adsorption.
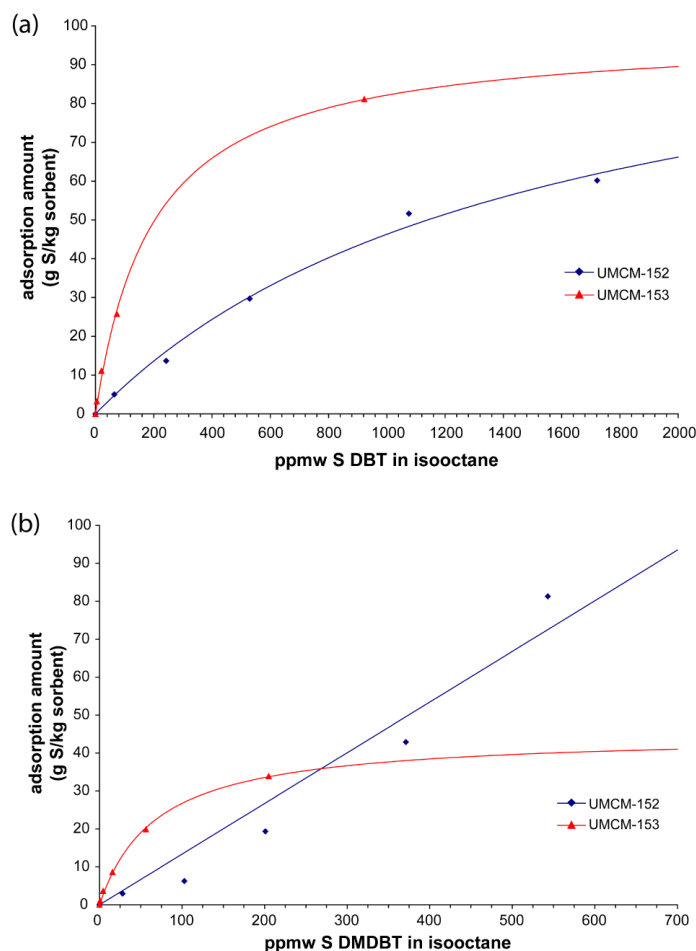
Figure 4.8: Adsorption isotherms for (a) DBT and (b) DMDBT for UMCM-152 (blue) and UMCM-153 (red). The curves represent a fit to the Langmuir equation and are intended as guides to the eye.

4.2.4. UMCM-154

Further increasing the number of carboxylates around the triphenylbenzene core while maintaining C_{2v} symmetry leads to linker **4**. Statistical analysis reveals that the 4:1 ratio of chemically equivalent carboxylates cannot form only one type of $M_2(CO_2R)_4$ paddlewheel; however, segregation involving p-benzoate groups coordinating to form one type of paddlewheel with isophthalates forming another paddlewheel or a series of

mixed carboxylate paddlewheels may be plausible. Attempts to form a coordination polymer with Cu have thus far failed; however, Zn coordinates with **4** to form an MCP termed UMCM-154.

The metal cluster present in UMCM-154 is uncommon, consisting of a three-bladed zinc paddlewheel with three carboxylates coordinated to two tetrahedral zinc ions and an additional two carboxylates coordinated to the axial positions. In this cluster, two isophthalate and one p-benzoate coordinate to form paddlewheels. The two remaining isophthalate carboxylates coordinate in the axial positions in a monodentate fashion (Figure 4.9a). Crystallographic evidence does not indicate the presence of a counter ion, suggesting that the metal cluster is uncharged. To satisfy this condition, half of the axial carboxylate groups must exist in the protonated form, generating a metal cluster formula of $Zn_2(CO_2)_4(CO_2H)$. The coordination geometry of this metal cluster has only been formed in MCP systems where severe steric strain[40] or copolymerization[41] of linkers is present. In UMCM-154, the formation of this three-bladed metal cluster over other more common Zn clusters is attributed to the thermodynamic requirements imposed by linker **4** having five carboxylates in a 1:4 symmetry equivalent ratio.

UMCM-154 exists in the space group C2/c and derives from a (5,5)-net. Sheets of isophthalate groups coordinating to the metal clusters are connected by pillars of *p*-benzoate groups (Figure 4.9b). Hexagonal channels of 14.9 × 6.8 Å are defined by three linkers coordinating with three metal clusters that stack in alternating directions (Figure 4.9c). UMCM-154 does not maintain permanent porosity upon guest removal. Collapse is attributed to an unstable metal cluster incorporating two monodentate coordinating carboxylates.
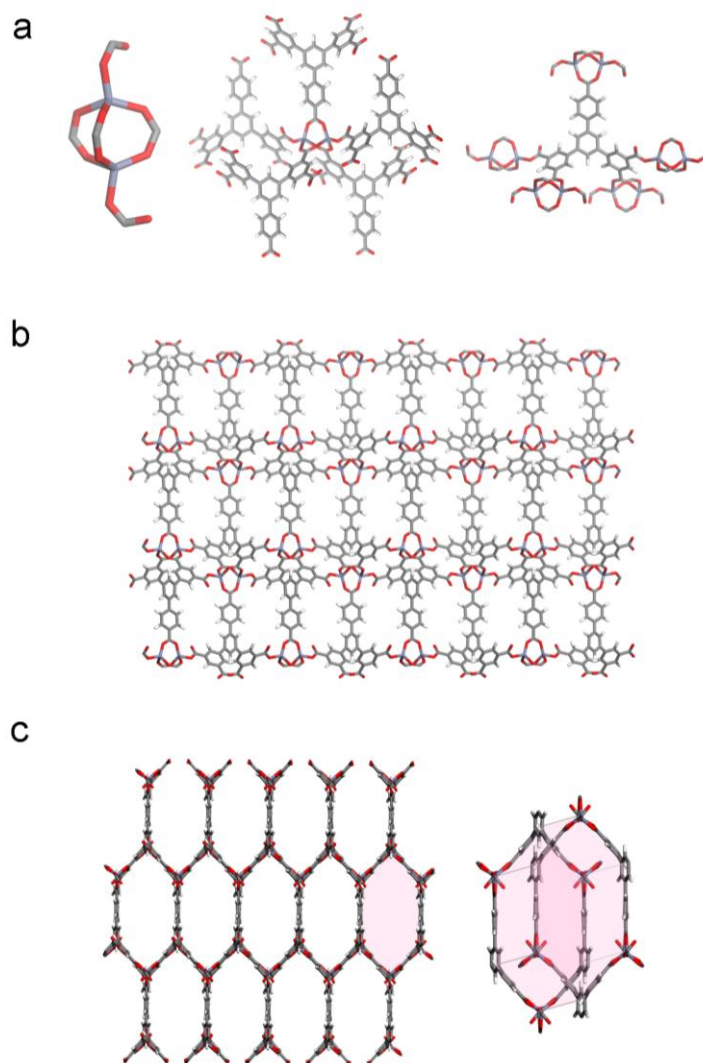
Figure 4.9: (a) Views of the three-bladed zinc paddlewheel metal cluster in UMCM-154. Each metal cluster coordinates to four isophthalate carboxylates and one *p*-benzoate group. Each linker contributes three equatorial "paddle" carboxylates and two axial coordinating carboxylates. (b) View along the *a*-axis. (c) View of hexagonal pores formed through the connection of three linkers and three Zn-metal clusters.

4.3 Conclusions

To summarize, reduced symmetry linkers offer a largely unexploited approach to the synthesis of high performance coordination polymers. They can drive new modes of assembly as illustrated by UMCM-150 and UMCM-154 and even common metal clusters

are susceptible to creating different networks due to supramolecular isomerism imparted by varying coordination modes of chemically distinct carboxylates. Framework isomers UMCM-152 and UMCM-153 show nearly identical gas adsorption properties and dramatically different capacities for organosulfur compounds providing direct evidence that liquid phase adsorption is dependent on pore size and shape rather than the typical pillars sorption behavior (linker identity, metal cluster identity, and surface area) alone. In addition, the inherent complexity of vertex desymmetrization associated with coordinating chemically distinct carboxylates to a metal cluster leads to highly porous materials lacking interpenetration rendering them important building blocks in the synthesis of a new generation of porous materials.

4.4 Experimental Section

All chemical reagents were obtained from commercial sources and, unless otherwise noted, were used as received.

4.4.1 Linker Synthesis

Preparation of H$_3$**2**. Methyl-3,5-dibromobenzoate (1.00 g, 3.66 mmol), methyl-4-carboxyphenylboronic acid[42] (1.38 g, 7.69 mmol) and K$_3$PO$_4$ (4.66 g, 22.0 mmol) were combined in 1,4-dioxane (40 mL) and the solution sparged with N$_2$ gas for 30 min. Pd(PPh$_3$)$_4$ (0.130 g, 0.112 mmol) was added and the suspension was stirred under N$_2$ for 20 hours at 100 °C in a pressure vessel. After cooling, H$_2$O (~100 mL) was added and a white solid precipitated. The coupled product was collected by filtration and purified through column chromatography on silica gel using CH$_2$Cl$_2$ as the eluent. The material

was hydrolyzed in a solution of KOH (1.5 M) in dioxane/H_2O (4:1, 20 mL) by heating at reflux for 18 hours. The solvent was evaporated and the residue was dissolved in water. The solution was acidified (pH ~ 2) by addition of conc HCl. The resulting white precipitate was collected by centrifugation, washed by resuspending in water then recollected by centrifugation. After multiple washing cycles the solid was dried under vacuum (0.92 g, 69 %). mp >300 °C; ^{1}H NMR (500 MHz, CDCl$_3$): δ 13.14 (br, 3H), 8.29 (d, 2H, J = 1.6 Hz), 8.26 (t, 1H, 1.6 Hz, 8.06 (m, 4H), 7.97, (m, 4H); ^{13}C NMR (125 MHz, CDCl$_3$): δ 167.1, 166.9, 143.1, 140.4, 132.5, 130.2, 130.0, 129.9, 127.3   HRMS (EI) (m/z) calcd (found) for $C_{21}H_{14}O_6$: 362.0790 (362.0805).

Preparation of intermediates for H$_4$**3** and H$_5$**4**. 1,3,5-Tribromobenzene (3.32 g, 10.5 mmol), methyl-4-carboxyphenylboronic acid (4.17 g, 23.2 mmol) and K_3PO_4 (13.4 g, 63.2 mmol) were combined in 1,4-dioxane (125 mL) and sparged with N_2 gas for 30 min. Pd(PPh$_3$)$_4$ (0.300 g, 0.260 mmol) was added and the suspension was stirred under N_2 for 20 hours at 100 °C in a pressure vessel. After cooling, H_2O (~1 L) was added and a white solid precipitated. The precipitate was dissolved in CH_2Cl_2 and dried over Na_2SO_4. The monocoupled and dicoupled esters were isolated using column chromatography on silica gel with CH_2Cl_2 and hexanes (75% CH_2Cl_2/25 % hexanes to 100% CH_2Cl_2) as the eluent. Dimethyl 5'-bromo-[1,1':3',1"-terphenyl]-4,4"-dicarboxylate: (3.12 g, 31.6 %) ^{1}H NMR (500 MHz, CDCl$_3$): δ 8.14 (m, 4H), 7.77 (d, 2H, J = 1.6 Hz), 7.75 (t, 1H, J = 1.6 Hz), 7.68 (m, 4H), 3.96 (s, 6H); ^{13}C NMR (125 MHz, CDCl$_3$): δ 166.7, 143.8, 142.7, 130.3, 129.8, 129.7, 127.2, 125.0, 123.6, 52.2. Methyl 3',5'-dibromo-[1,1'-biphenyl]-4-carboxylate: (1.61 g, 43.5 %) ^{1}H NMR (500 MHz, CDCl$_3$): δ 8.12 (m, 2H), 7.68 (s, 3H),

7.60 (m, 2H), 3.95 (s, 3H); ^{13}C NMR (125 MHz, CDCl$_3$): δ 166.7, 143.5, 142.6, 133.4, 130.3, 130.0, 129.2, 127.1, 123.4, 52.3.

Preparation of H$_4$**3**. Dimethyl 5'-bromo-[1,1':3',1"-terphenyl]-4,4"-dicarboxylate (0.69 g, 1.6 mmol), dimethyl isophthalate-5-pinacolboronate[31] (0.63 g, 1.96 mmol) and K$_3$PO$_4$ (1.0 g, 4.8 mmol) were combined in 1,4-dioxane/H$_2$O (9:1, 15 mL) and sparged with N$_2$ gas for 30 min. Pd(PPh$_3$)$_4$ (0.037 g, 0.036 mmol) was added and the suspension was stirred under N$_2$ for 16 hours at 100 °C in a pressure vessel. After cooling the solvent was evaporated and the crude product was taken up in CH$_2$Cl$_2$. The solution was cooled (-80 °C) and the precipitate was collected by cold filtration and dried. The material was hydrolyzed in a solution of KOH (1 M) in dioxane/H$_2$O (2:1, 20 mL) by heating at reflux for 18 hours. The solvent was evaporated and the residue was dissolved in water. The solution was acidified (pH ~ 2) through addition of conc HCl. The resulting white precipitate was collected by centrifugation, washed by resuspending in water then recollected by centrifugation. After multiple washing cycles the solid was dried under vacuum (0.54 g, 69 %). ^{1}H NMR (500 MHz, DMSO-d$_6$): δ 13.24 (br, 4H), 8.56 (d, 2H, J = 1.6 Hz), 8.52 (t, 1H, J = 1.5 Hz), 8.10 (t, 1H, J = 1.6 Hz) 8.08 (d, 2H, J = 1.6 Hz), 8.04 (s, 3H). ^{13}C NMR (100 MHz, CDCl$_3$): δ (167.1, 166.5, 143.7, 140.8, 140.8, 140.3, 132.2, 131.9, 130.0, 129.9, 127.5, 125.6. HRMS (EI) (m/z) calcd (found) for C$_{28}$H$_{18}$O$_8$: 482.1002 (482.1007).

Preparation of H$_5$**4**. Dimethyl 5'-bromo-[1,1':3',1"-terphenyl]-4,4"-dicarboxylate (1.00 g, 2.70 mmol), dimethyl isophthalate-5-pinacolboronate[43] (2.18 g, 6.49 mmol) and K$_3$PO$_4$ (3.45 g, 16.2 mmol) were combined in 1,4-dioxane/H$_2$O (9:1, 35 mL) and sparged with N$_2$ gas for 30 min. Pd(PPh$_3$)$_4$ (0.125 g, 0.108 mmol) was added and the suspension was

stirred under N_2 for 8 hours at 100 °C in a pressure vessel. After cooling the solvent was evaporated and the crude product was taken up in CH_2Cl_2. The solution was cooled (-80 °C) and the precipitate was collected by cold filtration and dried. The material was hydrolyzed in a solution of KOH (1 M) in dioxane/H_2O (2:1, 25 mL) by heating at reflux for 18 hours. The solvent was evaporated and the residue was dissolved in water. The solution was acidified (pH ~ 2) through addition of conc M HCl. The resulting white precipitate was collected by centrifugation, washed by resuspending in water then recollected by centrifugation. After multiple washing cycles the solid was dried under vacuum (0.423 g, 31 %). mp >300 °C ^{1}H NMR (500 MHz, DMSO-d_6): δ 13.15 (br, 5H), 8.54 (d, 4H, J = 1.6 Hz), 8.49 (t, 2H, J = 1.6 Hz), 8.04 (m, 7H), ^{13}C NMR (125 MHz, DMSO-d_6): δ 167.2, 167.0, 143.6, 140.9, 140.7, 140.2, 133.4, 131.3, 130.4, 129.9, 129.3, 127.4, 125.5, 125.3 HRMS (EI) (m/z) calcd (found) for $C_{29}H_{18}O_{10}$ [M-H]$^-$: 525.0827 (525.0822).

4.4.2 MCP Synthesis

Preparation of UMCM-151 [$Cu_2(C_{21}H_{11}O_6)_{1.33}$]. Linker H$_3$**2** (0.050 g, 0.14 mmol) was added to a solution of DMF/dioxane/H_2O (4:1:1, 10 mL) in a 20 mL scintillation vial. To this mixture was added $Cu(NO_3)_2·2.5H_2O$ (0.096 g, 0.41 mmol) and the contents were sonicated until dissolved and then heated at 85 °C. After 12 hours, the mother liquor was decanted and replaced with fresh DMF/dioxane/H_2O (4:1:1). The blue crystals were exchanged twice in DMF and five times in acetone. The material was dried under vacuum at room temperature for 4 h in which time the crystals turned green. The yield of the reaction based upon the weight of the solvent-free material is 80% based upon H$_3$**2**. Anal. Calcd (Found) for [$Cu_2(C_{21}H_{11}O_6)(H_2O)_5$]: C, 52.39 (51.96) H, 2.89 (2.50).

Preparation of UMCM-152 [$Cu_2(C_{28}H_{14}O_8)$)] Linker H$_4$**3** (0.050 g, 0.10 mmol) was added to a solution of 0.005 M HCl in DMF/dioxane/H$_2$O (4:1:1, 10 mL) in a 20 mL scintillation vial. To this mixture, $Cu(NO_3)_2 \cdot 2.5H_2O$ (0.096 g, 0.41 mmol) was added and the contents were sonicated until dissolved and then heated at 85 °C. After 12 hours, the mother liquor was decanted and replaced with fresh DMF/dioxane/H$_2$O (4:1:1). Blue block-like crystals were washed twice with DMF and five times with acetone. Solvent was removed under vacuum for 4 h and further dried at 100 ºC for 18 h to yield a dark purple material. The yield of the reaction based upon the weight of the solvent-free material is 82 % based upon H$_4$**3**. Anal. Calcd (Found) for [$Cu_2(C_{28}H_{14}O_8)(H_2O)_{1.5}$]: C, 53.17 (52.89) H, 2.71 (2.28).

Preparation of UMCM-153 [$Cu_2(C_{28}H_{14}O_8)$)]. Linker H$_4$**3** (0.050 g, 0.10 mmol) was added to a solution of NMP/dioxane/H$_2$O (4:1:1, 10 mL) in a 20 mL scintillation vial. To this mixture, $Cu(NO_3)_2 \cdot 2.5H_2O$ (0.096 g, 0.41 mmol) was added and the contents were sonicated until dissolved and then heated at 85 °C. After 24 hours, the mother liquor was decanted and replaced with fresh NMP/dioxane/H$_2$O (4:1:1). Blue blade-like crystals were washed twice with DMF and five times with acetone. Solvent was removed under vacuum for 4 h and further dried at 100 ºC for 18 h to yield a dark purple material. The yield of the reaction based upon the weight of the solvent-free material is 55 % based upon H$_4$**3**. Anal. Calcd (Found) for [$Cu_2(C_{28}H_{14}O_8)(H_2O)_{1.5}$]: C, 53.17 (53.37) H, 2.71 (2.50).

Preparation of UMCM-154 [$Zn_2(C_{29}H_{14}O_{10})$)].Linker H$_5$**4** (0.050 g, 0.095 mmol) was added to DMF (10 mL) in a 20 mL scintillation vial. To this mixture, $Zn(NO_3)_2 \cdot 6H_2O$ (0.14 g, 0.47 mmol) was added and the contents were sonicated until dissolved and

heated at 85 °C. After 24 h the mother liquor was decanted and replaced with fresh DMF. Crystals were washed twice with DMF and five times with CH_2Cl_2 to yield colorless polygons. The solvent was removed under vacuum for 6 hours and the yield of the reaction based upon the weight of $[Zn_2(C_{29}H_{14}O_{10})(C_3H_6NO)(H_2O)_5]$ is 87 % based upon $H_5\mathbf{4}$. Anal. Calcd (Found) for $[Zn_2(C_{29}H_{14}O_{10})(C_3H_6NO)(H_2O)_5]$: C, 47.14 (47.45), H, 3.71 (3.59), N, 1.72 (2.26).

4.4.3. Gas Sorption

Nitrogen adsorption/desorption isotherms were measured volumetrically at 77 K in the range $1.00 \times 10^{-3} \leq P/Po \leq 1.00$ with an Autosorb-1C outfitted with the micropore option by Quantachrome Instruments (Boynton Beach, Florida USA), running version 1.2 of the ASWin software package. Ultra-high purity He (99.999%, for void volume determination) and N_2 (99.999%) were purchased from Cryogenic Gasses and used as received. MCPs exchanged with acetone were charged into a sample cell and dried under vacuum (< 0.1 mTorr) at 100 °C. The resulting mass of dried material in the cell was ~10 mg. The specific surface areas were determined using either the BET or the Langmuir equation (Figures 4.10-4.13).

Argon sorption experiments were performed at 87 K in the range $1.00 \times 10^{-4} \leq P/Po \leq 1.00$ with ultra-high purity Ar (99.999%) purchased from Cryogenic Gasses. Pore size distributions were calculated using the Non-local Density Functional Theory (NLDFT) zeolite/silica equilibrium transition kernel for Ar adsorption at 87 K based on a cylindrical pore model as implemented in version 1.2 of the ASWin software package (Figures 4.14-4.17).

Volumetric hydrogen adsorption measurements were performed on ~400 mg samples using an automated volumetric Sieverts' apparatus (PCT-Pro 2000 from Hy-Energy LLC) over the 0-60 bar range. The excess hydrogen adsorption isotherms were calculated from successive gas expansions by adding the differences between the amounts of gas depleted from the reference cell and that occupying the sample cell after each expansion. Dead space volumes were determined at room temperature using helium gas as a negligibly adsorbing gas. Ultra-high purity hydrogen and helium (99.999% purity) obtained from Airgas Inc. were used for all measurements.

4.4.4. Thermogravimetric Analysis

Measurements were performed on a TA Q50 TGA apparatus. Approximately 10 mg of acetone or CH_2Cl_2 exchanged material was loaded onto a platinum pan and excess solvent was allowed to evaporate to yield a free flowing powder before starting a temperature programmed ramp (Figure 4.18). Conditions: temperature ramp from $30 - 500$ °C at 5 °C/min under a flow of N_2 gas.

4.4.5. Powder X-Ray Diffraction

Powder X-ray diffraction was performed on a Rigaku R-Axis Spider diffractometer with an image plate detector and Cu Kα radiation operating in transmission mode. The sample was rotated in φ and oscillated in ω to minimize preferred orientation. Diffraction patterns are shown in Figure 4.19.

4.4.6. Crystal Structure Determination.

Single crystals suitable for X-ray structure determination were selected under a microscope and mounted in MiTiGen micro-mounts or on Nylon loops with Paratone N

hydrocarbon oil and placed in a stream of cold nitrogen from an Oxford Cryosystems Cryostream Plus cooler for low temperature data collection. For the room temperature collection, suitable crystals were glued to the end of a thin glass capillary. Intensity data were collected on a three circle (quarter χ–arm) Rigaku R-Axis Spider diffractometer (460 mm $\times$ 256 mm curved imaging plate detector with graphite monochromated Cu Kα radiation (λ = 1.54187 Å)). Initial ω scans of each sample were performed to determine preliminary unit cell parameters and to allow the selection of image widths for data collection. For all cases oscillation images were collected using widths of 2.0-2.5° in ω. Data were collected using the d*TREK package in the CrystalClear software suite[44] to obtain ω scans for χ at 0° and 54°. Using the FS_PROCESS[45] package in CrystalClear, the raw intensity data were then reduced to F^2 values with corrections for Lorentz, and polarization effects. Decay of the crystals during data collection was negligible. An empirical absorption correction was applied as implemented by FS_PROCESS. The structures were solved within the CrystalStructure[46] package by direct methods and refined against all data.[47] Hydrogen atoms were placed at calculated positions (C - H = 0.93 Å) using a riding model with isotropic displacement parameters scaled by the U_{eq} of the attached carbon atom. Thermal parameters for all non-hydrogen atoms were refined anisotropically. In structures with voids, attempts to locate and model the highly disordered solvent molecules in the voids were unsuccessful. Therefore the SQUEEZE routine of PLATON[48] was used to remove the diffraction contribution from these solvents to produce a set of solvent free diffraction intensities. Crystallographic data parameters are summarized in Tables 4.1-4.4.
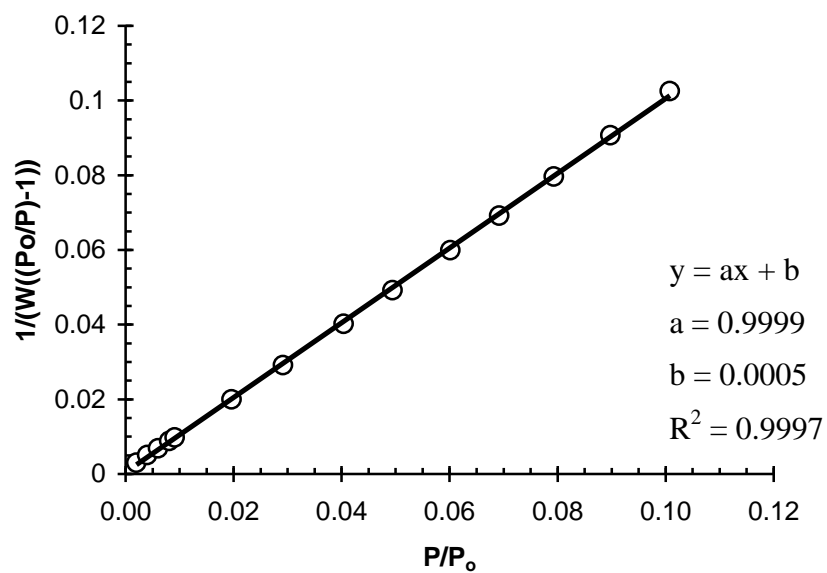
Figure 4.10: BET plot of the N_2 isotherm for UMCM-152 collected at 77 K.
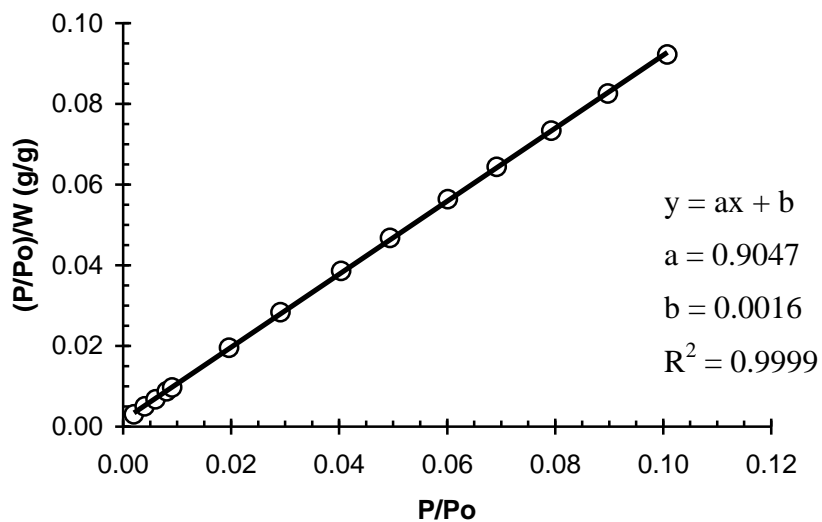
Figure 4.11: Langmuir plot of the N_2 isotherm for UMCM-152 collected at 77 K.
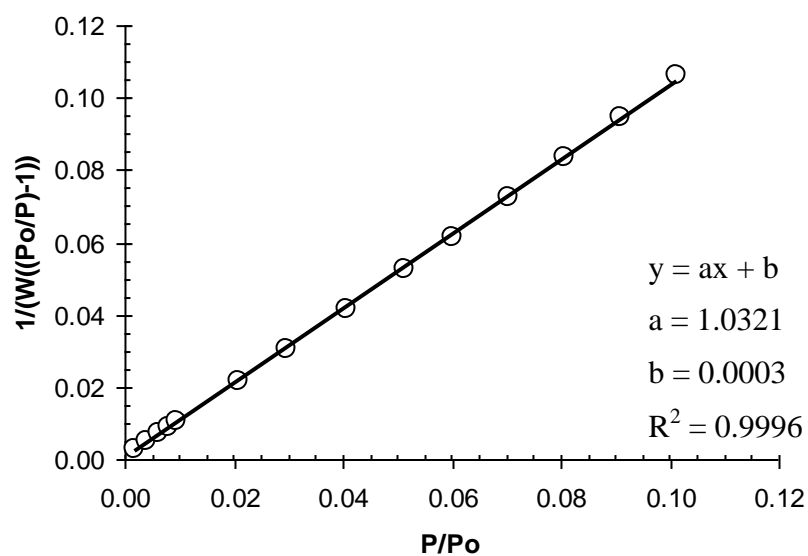
Figure 4.12: BET plot of the N_2 isotherm for UMCM-153 collected at 77 K.
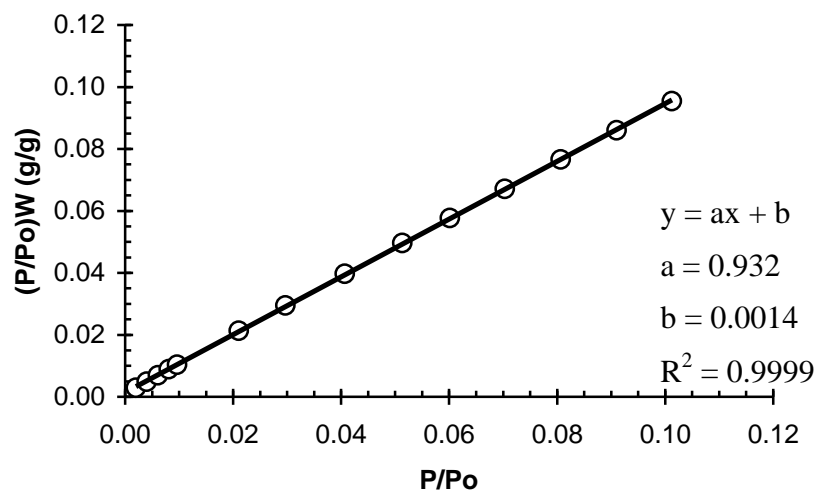
Figure 4.13: Langmuir plot of the N_2 isotherm for UMCM-153 collected at 77 K.
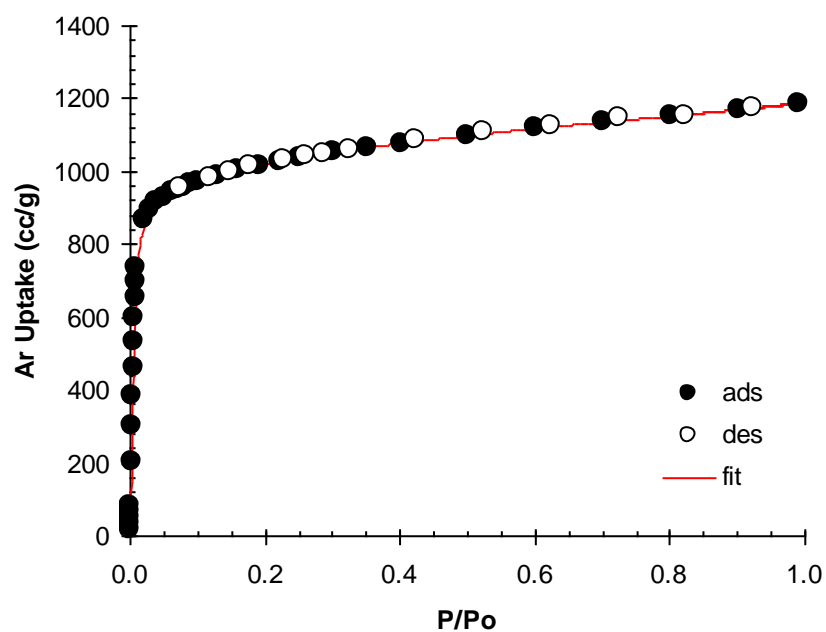
Figure 4.14: Ar sorption isotherm at 87 K for UMCM-152 and the corresponding NLDFT fit based on a cylindrical pore model.
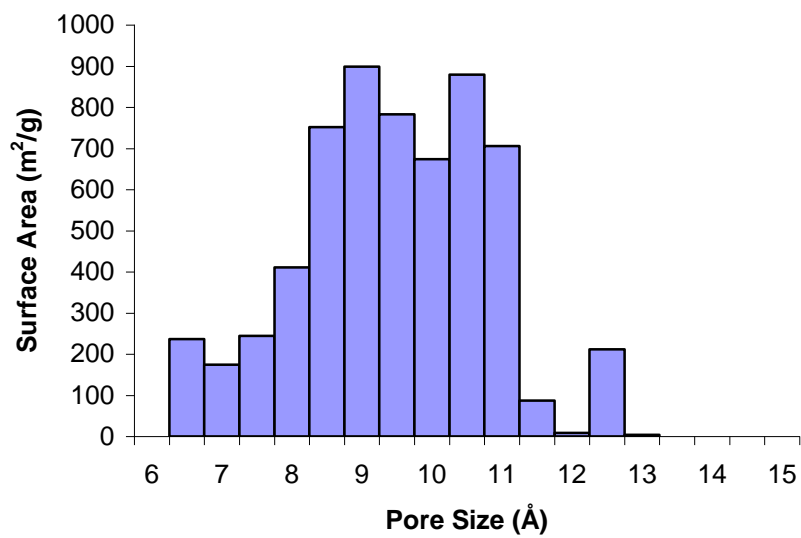
Figure 4.15: Pore size distribution of UMCM-152.
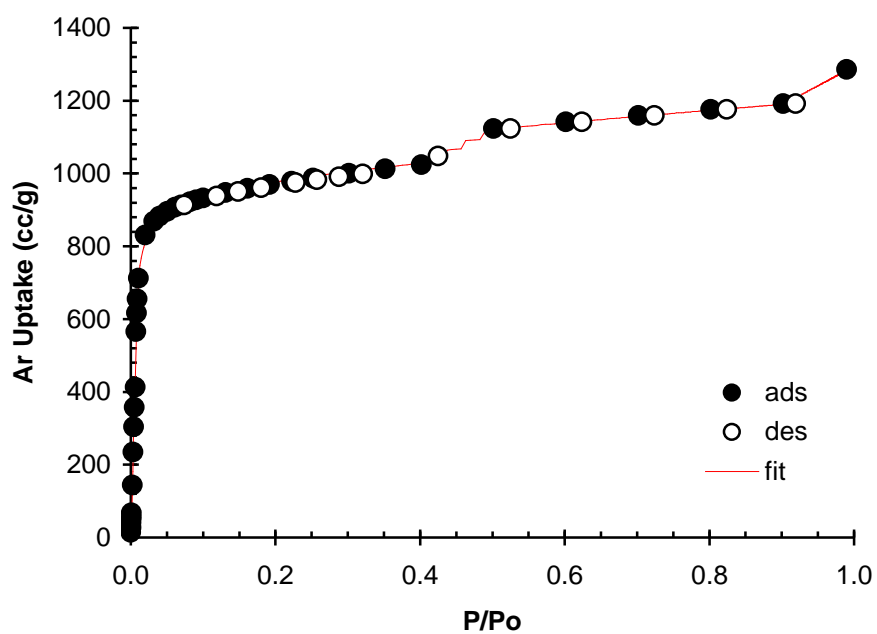
Figure 4.16: Ar sorption isotherm at 87 K for UMCM-153 and the corresponding NLDFT fit based on a cylindrical pore model.
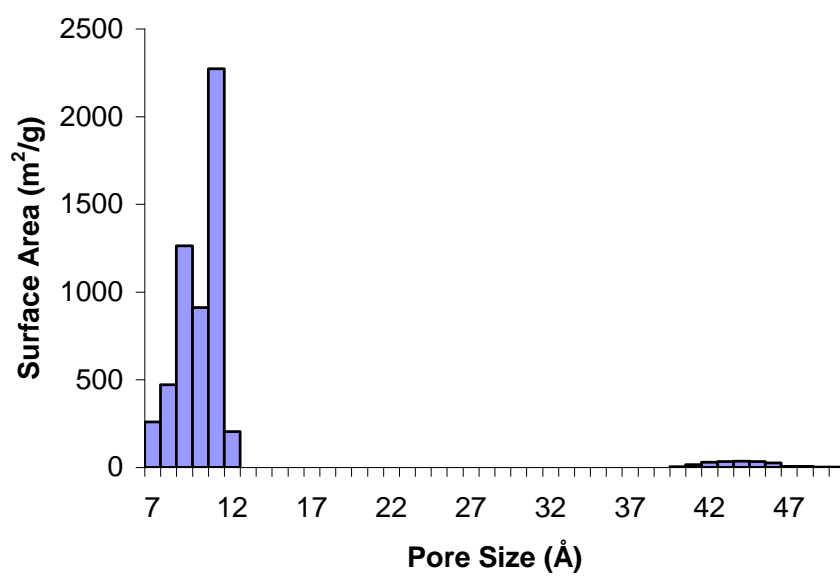
Figure 4.17. Pore size distribution of UMCM-153.
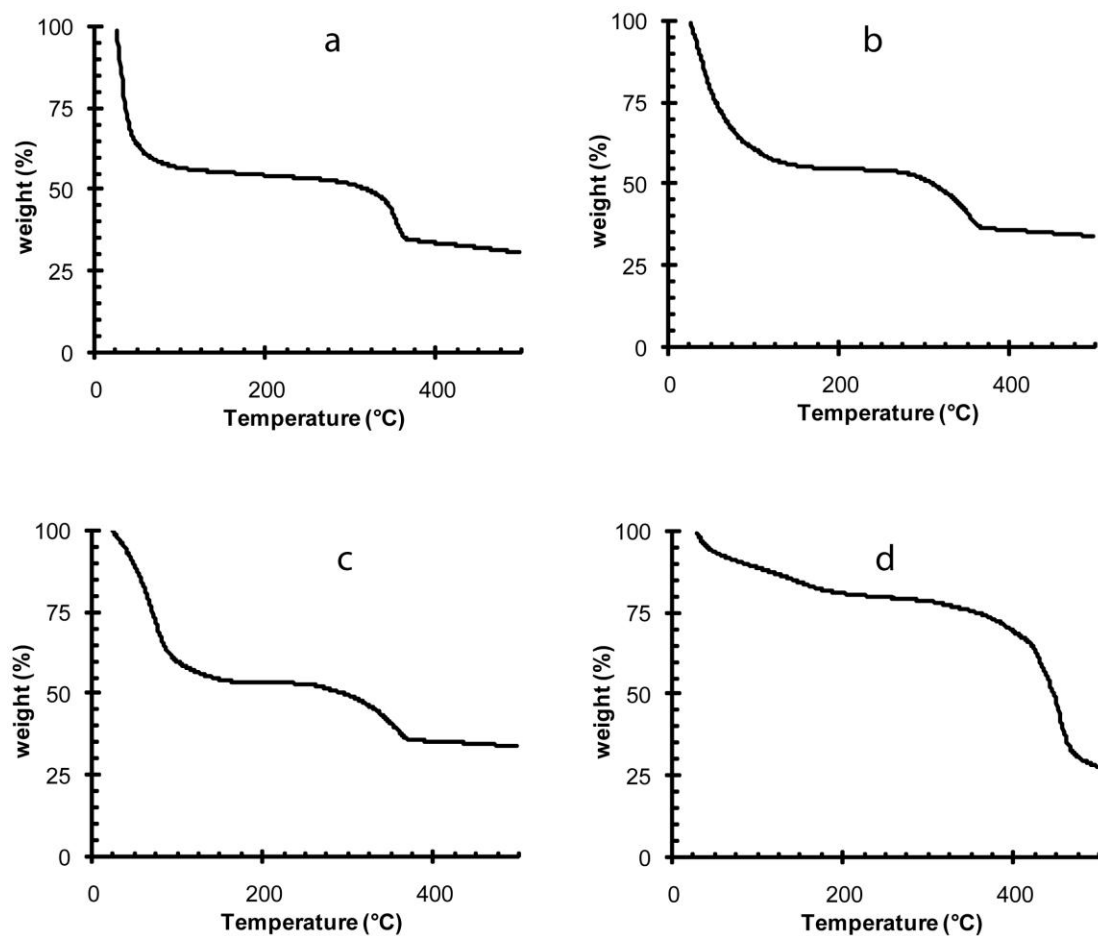
Figure 4.18: TGA traces of (a) UMCM-151, (b) UMCM-152, (c) UMCM-153, and (d) UMCM-154.
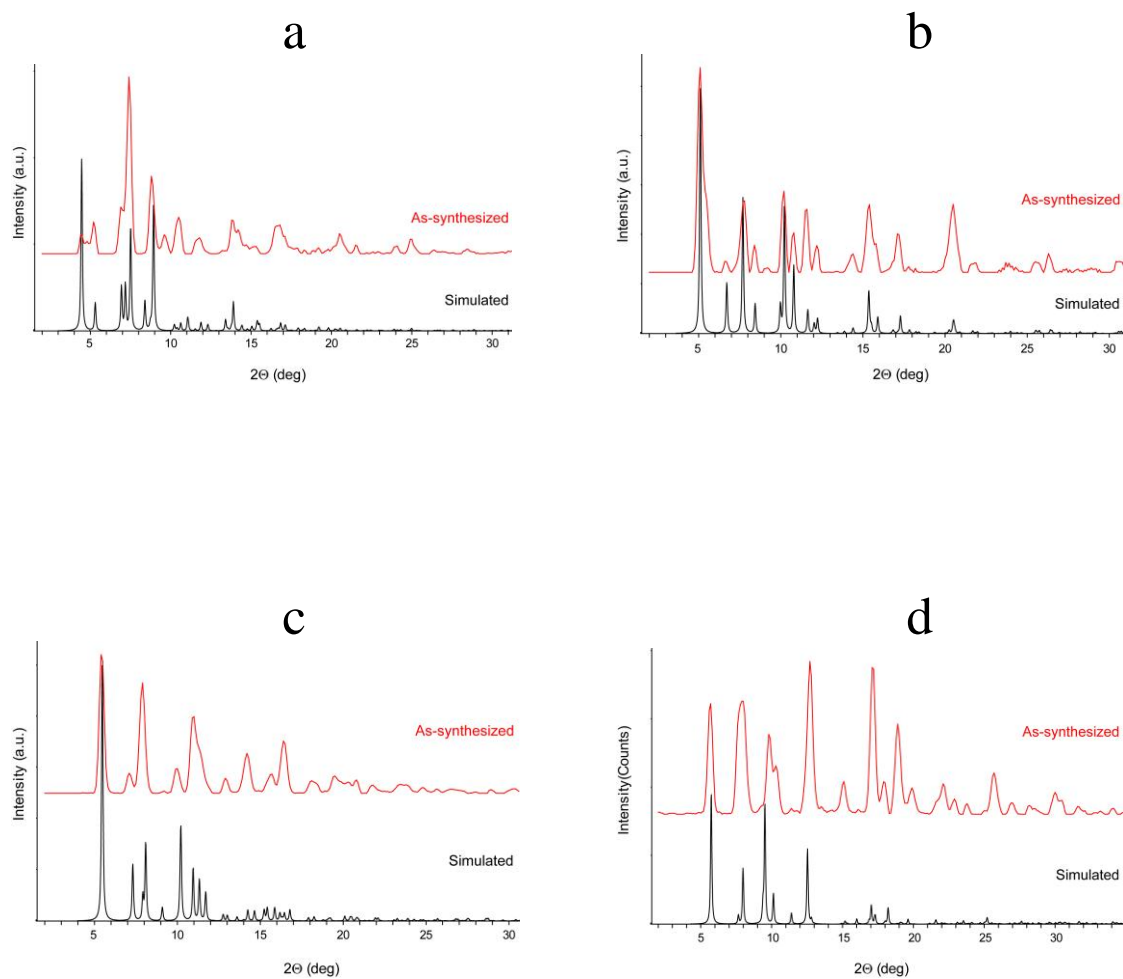
Figure 4.19: As-synthesized and simulated PXRD patterns for (a) UMCM-151, (b) UMCM-152, (c) UMCM-153, and (d) UMCM-154.

Table 4.1 Crystallographic Data for UMCM-151

|	
Empirical formula	$C_{42}H_{22}O_{15}Cu_3$
Formula weight	957.22
Temperature	253 K
Wavelength	1.5418
Crystal System	orthorhombic
Space Group	*Immm*
Unit Cell Dimensions	$a = 24.6055(17)$ Å $\quad \alpha = 90º$
	$b = 33.271(2)$ Å $\quad \beta = 90º$
	$c = 33.271(2)$ Å $\quad \gamma = 90º$
Volume	27237(2) $Å^3$
Z	8
Density (calculated)	0.467 g/cm^3
Absorption coefficient	0.727 mm^{-1}
F(000)	3848
Crystal Size	$0.30 \times 0.20 \times 0.15$ mm^3
Theta range for data collection	8.72 to 70.17
Index ranges	$0 \leq h \leq 28, 0 \leq k \leq 37, 0 \leq l \leq 38$
Reflections collected	12271
Independent reflections	5264 [R(int) = 0.235]]
Completeness to theta = 70.17	80.9 %
Absorption correction	Empirical from equivalents
Max. and min. transmission	0.8987 and 0.8114
Refinement method	Full-matrix least-squares on F^2
Data / restraints / parameters	5264 / 0 / 288
GOF on F^2	1.140
Final R indices [I>2sigma(I)]	R1 = 0.1327 wR2 = 0.3493
R indices (all data)	R1 = 0.1744 wR2 = 0.3785
Largest diff. peak and hole	1.247 and -1.351 $e^-/Å^3$

Table 4.2 Crystallographic Data for UMCM-152.

Empirical formula	$C_{14}H_7O_5Cu_5$
Formula weight	318.74
Temperature	293 (2) K
Wavelength	1.54187
Crystal System	Trigonal
Space Group	*R3m*
Unit Cell Dimensions	a = 26.3043(11) Å $\quad$ $\alpha = 90º$
	b = 26.3043(11) Å $\quad$ $\beta = 90º$
	c = 26.5885(19) Å $\quad$ $\gamma = 120º$
Volume	15932.3(15) $Å^3$
Z	18
Density (calculated)	0.598 g/cm^3
Absorption coefficient	0.932 mm^{-1}
F(000)	2880
Crystal Size	$0.12 \times 0.09 \times 0.07$ mm^3
Theta range for data collection	6.73 to 50.31
Index ranges	$-25 \leq h \leq 19$, $-20 \leq k \leq 26$, $-26 \leq l \leq 21$
Reflections collected	11560
Independent reflections	3479 [R(int) = 0.0759]]
Completeness to theta = 50.31	99.5 %
Absorption correction	Empirical from equivalents
Max. and min. transmission	0.9376 and 0.8963
Refinement method	Full-matrix least-squares on F^2
Data / restraints / parameters	3479 / 1 / 193
GOF on F^2	1.053
Final R indices [I>2sigma(I)]	R1 = 0.0555 wR2 = 0.1404
R indices (all data)	R1 = 0.0681 wR2 = 0.1555
Largest diff. peak and hole	0.383 and -0.503 $e^-/Å^3$

Table 4.3 Crystallographic Data for UMCM-153.

Empirical formula	$C_{14}H_7O_5Cu$
Formula weight	318.74
Temperature	150 (2) K
Wavelength	1.54187
Crystal System	orthorhombic
Space Group	*Fddd*
Unit Cell Dimensions	a = 21.7064(7) Å $\alpha = 90º$
	b = 29.0072(11) Å $\beta = 90º$
	c = 43.700(3) Å $\gamma = 90º$
Volume	27515(2) $Å^3$
Z	32
Density (calculated)	0.616 g/cm^3
Absorption coefficient	0.960 mm^{-1}
F(000)	5120
Crystal Size	$0.22 \times 0.06 \times 0.04$ mm^3
Theta range for data collection	6.51 to 50.42
Index ranges	$-17 \leq h \leq 21$, $0-17 \leq k \leq 28$, $-43 \leq l \leq 28$
Reflections collected	15770
Independent reflections	3591 [R(int) = 0.1197]
Completeness to theta = 50.42	99.5 %
Absorption correction	Empirical from equivalents
Max. and min. transmission	0.9626 and 0.8166
Refinement method	Full-matrix least-squares on F^2
Data / restraints / parameters	3591 / 0 / 183
GOF on F^2	0.988
Final R indices [I>2sigma(I)]	R1 = 0.0768 wR2 = 0.1949
R indices (all data)	R1 = 0.1064 wR2 = 0.2088
Largest diff. peak and hole	0.811 and -0.413 $e^-/Å^3$

Table 4.4 Crystallographic Data for UMCM-154.

Empirical formula	$C_{29}H_{13}O_{10}Zn_2$
Formula weight	652.13
Temperature	95 (2) K
Wavelength	1.54187
Crystal System	monoclinic
Space Group	*C2/c*
Unit Cell Dimensions	a = 11.8586(2) Å $\alpha = 90.00°$
	b = 30.7710(6) Å $\beta = 90.983(6)°$
	c = 17.4516(12) Å $\gamma = 90.00°$
Volume	6367.2(5) Å^3
Z	4
Density (calculated)	0.680 g/cm^3
Absorption coefficient	1.146 mm^{-1}
F(000)	1308
Crystal Size	$0.56 \times 0.25 \times 0.13$ mm^3
Theta range for data collection	6.51 to 66.59
Index ranges	$-12 \leq h \leq 14$, $-36 \leq k \leq 35$, $-17 \leq l \leq 2119$
Reflections collected	23435
Independent reflections	5485 [R(int) = 0.0426]]
Completeness to theta = 66.59	97.4 %
Absorption correction	Empirical from equivalents
Max. and min. transmission	0.8654 and 0.5663
Refinement method	Full-matrix least-squares on F^2
Data / restraints / parameters	5485 / 0 / 188
GOF on F^2	1.169
Final R indices [I>2sigma(I)]	R1 = 0.0724 wR2 = 0.2508
R indices (all data)	R1 = 0.0850 wR2 = 0.2802
Largest diff. peak and hole	0.609 and -0.831 e$^-$/Å^3

4.5. References

(1)   Wong-Foy, A. G.; Matzger, A. J.; Yaghi, O. M. *J. Am. Chem. Soc.* **2006**, *128*, 3494-3495.

(2)   Kaye, S. S.; Dailly, A.; Yaghi, O. M.; Long, J. R. *J. Am. Chem. Soc.* **2007**, *129*, 14176-14177.

(3)   Koh, K.; Wong-Foy, A. G.; Matzger, A. J. *Angew. Chem., Int. Edit.* **2008**, *47*, 677-680.

(4)   Koh, K.; Wong-Foy, A. G.; Matzger, A. J. *J. Am. Chem. Soc.* **2009**, *131*, 4184-4185.

(5)   Porter, W. W.; Wong-Foy, A.; Dailly, A.; Matzger, A. J. *J. Mater. Chem.* **2009**, *19*, 6489-6491.

(6)   Sumida, K.; Hill, M. R.; Horike, S.; Dailly, A.; Long, J. R. *J. Am. Chem. Soc.* **2009**, *131*, 15120-15121.

(7)   Yan, Y.; Lin, X.; Yang, S. H.; Blake, A. J.; Dailly, A.; Champness, N. R.; Hubberstey, P.; Schröder, M. *Chem. Commun.* **2009**, 1025-1027.

(8)   Wang, X.-S.; Ma, S.; Yuan, D.; Yoon, J. W.; Hwang, Y. K.; Chang, J.-S.; Wang, X.; Jørgensen, M. R.; Chen, Y.-S.; Zhou, H.-C. *Inorg. Chem.* **2009**, *48*, 7519-7521.

(9)   Zhao, D.; Yuan, D.; Sun, D.; Zhou, H.-C. *J. Am. Chem. Soc.* **2009**, *131*, 9186-9188.

(10)   Férey, G.; Mellot-Draznieks, C.; Serre, C.; Millange, F.; Dutour, J.; Surble, S.; Margiolaki, I. *Science* **2005**, *309*, 2040-2042.

(11)   Hong, S.; Oh, M.; Park, M.; Yoon, J. W.; Chang, J.-S.; Lah, M. S. *Chem. Commun.* **2009**, 5397-5399.

(12)   Yan, Y.; Telepeni, I.; Yang, S.; Lin, X.; Kockelmann, W.; Dailly, A.; Blake, A. J.; Lewis, W.; Walker, G. S.; Allan, D. R.; Barnett, S. A.; Champness, N. R.; Schröder, M. *J. Am. Chem. Soc.* **2010**, *132*, 4092-4094.

(13)   Ma, S. Q.; Sun, D. F.; Ambrogio, M.; Fillinger, J. A.; Parkin, S.; Zhou, H. C. *J. Am. Chem. Soc.* **2007**, *129*, 1858-1859.

(14)   Furukawa, H.; Ko, N.; Go, Y. B.; Aratani, N.; Choi, S. B.; Choi, E.; Yazaydin, A. O.; Snurr, R. Q.; O'Keeffe, M.; Kim, J.; Yaghi, O. M. *Science*, **2010**, *239, 424 - 428.

(15) Yuan, D.; Zhao, D.; Sun, D.; Zhou, H.-C. *Angew. Chem. Int. Ed.*, **2010**, *49*, 5357-5361.

(16) Farha, O. K.; Yazaydin, Ö.; Eryazici, I.; Malliakas, C. D.; Hauser, B. G.; Kanatzidis, M. G.; Nguyen, S. T.; Snurr, R.Q.; Hupp, J. T. *Nature Chemistry*, **2010**, *2*, 944 - 948.

(17) Wong-Foy, A. G.; Lebel, O.; Matzger, A. J. *J. Am. Chem. Soc.* **2007**, *129*, 15740-15741.

(18) Feng, L.; Chen, Z. X.; Liao, T. B.; Li, P.; Jia, Y.; Liu, X. F.; Yang, Y. T.; Zhou, Y. M. *Cryst. Growth Des.* **2009**, *9*, 1505-1510.

(19) Guo, Z.; Li, G.; Zhou, L.; Su, S.; Lei, Y.; Dang, S.; Zhang, H. *Inorg. Chem.* **2009**, *48*, 8069-8071.

(20) Ma, L. Q.; Lin, W. B. *Angew. Chem., Int. Edit.* **2009**, *48*, 3637-3640.

(21) Ma, L. Q.; Mihalcik, D. J.; Lin, W. B. *J. Am. Chem. Soc.* **2009**, *131*, 4610-4612.

(22) Nelson, A. P.; Farha, O. K.; Mulfort, K. L.; Hupp, J. T. *J. Am. Chem. Soc.* **2009**, *131*, 458-460.

(23) Reineke, T. M.; Eddaoudi, M.; Moler, D.; O'Keeffe, M.; Yaghi, O. M. *J. Am. Chem. Soc.* **2000**, *122*, 4843-4844.

(24) Walton, K. S.; Snurr, R. Q. *J. Am. Chem. Soc.* **2007**, *129*, 8552-8556.

(25) Weisstein, E. W. "Platonic Solid". *MathWorld--A Wolfram Web Resource*. http://mathworld.wolfram.com/PlatonicSolid.html.

(26) Wells, A. F.; Clarendon Press: Oxford, London, 1956, p 143.

(27) Weisstein, E. W. "Archimedean Solid". *MathWorld--A Wolfram Web Resource. http://mathworld.wolfram.com/ArchimedeanSolid.html.*

(28) Schnobrich, J. K.; Koh, K.; Sura, K. N.; Matzger, A. J. *Langmuir* **2010**, *26,* 5808-5814.

(29) Düren, T.; Millange, F.; Férey, G.; Walton, K. S.; Snurr, R. Q. *J. Phys. Chem. C* **2007**, *111*, 15350-15356.

(30) Lin, X.; Jia, J. H.; Zhao, X. B.; Thomas, K. M.; Blake, A. J.; Walker, G. S.; Champness, N. R.; Hubberstey, P.; Schröder, M. *Angew. Chem., Int. Edit.* **2006**, *45*, 7358-7364.

(31) Caskey, S. R.; Wong-Foy, A. G.; Matzger, A. J. *Inorg. Chem.* **2008**, *47*, 7751-7756.

(32)   Wang, X. S.; Ma, S. Q.; Forster, P. M.; Yuan, D. Q.; Eckert, J.; López, J. J.; Murphy, B. J.; Parise, J. B.; Zhou, H. C. *Angew. Chem., Int. Edit.* **2008**, *47*, 7263-7266.

(33)   Sun, D. F.; Ke, Y. X.; Mattox, T. M.; Ooro, B. A.; Zhou, H. C. *Chem. Commun.* **2005**, 5447-5449.

(34)   Sun, D.; Ma, S.; Simmons, J. M.; Li, J.-R.; Yuan, D.; Zhou, H.-C. *Chem. Commun.* **2010**, *46*, 1329-1331.

(35)   Liu, M.; Wong-Foy, A. G.; Vallery, R. S.; Frieze, W. E.; Schnobrich, J. K.; Gidley, D. W.; Matzger, A. J. *Adv. Mater.* **2010**, *22*, 1598-1601.

(36)   Cychosz, K. A.; Ahmad, R.; Matzger, A. J. *Chemical Science*, **2010**, *1*, 293-302.

(37)   Cychosz, K. A.; Wong-Foy, A. G.; Matzger, A. J. *J. Am. Chem. Soc.* **2008**, *130*, 6938-6939.

(38)   Cychosz, K. A.; Wong-Foy, A. G.; Matzger, A. J. *J. Am. Chem. Soc.* **2009**, *131*, 14538-14543.

(39)   Vaidhyanathan, R.; Bradshaw, D.; Rebilly, J.-N.; Barrio, J. P.; Gould, J. A.; Berry, N. G.; Rosseinsky, M. J. *Angew. Chem. Int. Ed.* **2006**, *45*, 6495-6499.

(40)   Vagin, S.; Ott, A.; Weiss, H. C.; Karbach, A.; Volkmer, D.; Rieger, B. *Eur. J. Inorg. Chem.* **2008**, 2601-2609.

(41)   Hou, L.; Zhang, J. P.; Chen, X. M. *Cryst. Growth Des.* **2009**, *9*, 2415-2419.

(42)   Percec, V.; Won, B. C.; Peterca, M.; Heiney, P. A. *J. Am. Chem. Soc.* **2007**, *129*, 11265-11278.

(43)   Natera, J.; Otero, L.; Sereno, L.; Fungo, F.; Wang, N.-S.; Tsai, Y.-M.; Hwu, T.-Y.; Wong, K.-T. *Macromolecules* **2007**, *40*, 4456-4463.

(44)   CrystalClear 2.0, Rigaku and Rigaku/MSC: TX, USA, 2009.

(45)   Higashi, T. Program for Absorption Correction, Rigaku Corporation: Tokyo, Japan, 1995.

(46)   CrystalStructure 3.8.1 Single Crystal Structure Analysis Software, Rigaku and Rigaku/MSC: TX, USA, 2007.

(47)   Sheldrick, G. M. SHELXS '97 and SHELXL '97, Programs for Crystal Structure Analysis, University of Göttingen, Germany, 1997.

(48)   Spek, A. L. PLATON, A Multipurpose Crystallographic Tool, Utrecht University, Utrecht, The Netherlands, 2005.

CHAPTER 5

Conclusions and Future Directions

5.1.   Introduction

In this thesis, the relationship between surface area and building block components of microporous coordination polymers (MCPs) was scrutinized with the aim of discerning how structures can be precisely designed for gas sorption applications. Using the geometric accessible surface area method,[1] model structures were dissected so that surface area contributions could be separately attributed to linker and metal cluster components. It was discovered that linker functionalization and branching led to suboptimal surface areas due to inefficient distribution of linker mass and that the highest surface areas were achieved from para-extended linkers with few coordinating groups.

Because many synthetic strategies leading to high theoretical surface areas also lead to interpenetration or framework collapse, implementation of the aforementioned linker design guidelines was cautiously approached with due consideration for framework stability. The tactic of pairing a relatively large linker with six coordinating groups led to the formation of UMCM-300. Similar strategies employed by other groups have confirmed that this linker geometry is predisposed to avoid interpenetration and can therefore form MCPs having remarkable surface areas and capacities for hydrogen at cryogenic temperatures. In a second strategy, non-interpenetrated MCPs were constructed

with linkers containing symmetry-inequivalent carboxylate groups. Although all highly porous, the stability of these MCPs was problematic; only three of five examples maintain permanent porosity upon activation. These studies demonstrate the delicate balance of maintaining structural stability with high levels of porosity. Herein, areas of further study are suggested, both in the context of the work presented within this thesis and in the broader field.

5.2. Further Development of the LiMe Ratio Prediction Method

The LiMe ratio surface area prediction method lays a foundation for understanding the theoretical maximum achievable surface area for a given linker and metal cluster combination. This was accomplished by using the two most common metal clusters yielding MCPs with permanent porosity, $M_4O(CO_2R)_6$ and $M_2(CO_2R)_4$, connected to para-linked benzene units. Although this method offers a significant advantage over other theoretical surface area strategies (because minimum data input is required) the output shows only general structural modification trends and fails to yield accurate values in cases where variations such as functionalization and ring fusion exist. To build a more complete surface area model, correction factors need to be established for these conditions. Perhaps the easiest way to account for such linker modifications is to average the surface area change exhibited by MCPs containing these chemical variations. Increments can then be added or subtracted from the poly(*p*-phenylene) linker models already presented in Chapter 2 to predict surface area of MCPs having functionalized linkers.

A far more detailed approach may be needed in order to build an accurate surface area model for predicting limiting values even for perfect crystals. This would involve building new series of infinite linker chains so that additional surface area equations may be formulated. This strategy would be particularly beneficial for linkers that do not closely resemble a poly(*p*-phenylene) structure. For example, the linker of NU-100[2] consists of alternating benzene and triple bonded units. While the geometric accessible surface area of an infinite poly(p-phenylene) unit was determined to be 10,577 m^2/g, the theoretical surface area of alternating triple bonded and benzene units is substantially more (12,220 m^2/g). Furthermore, an infinite chain of triple bonded units gives a value of 15,080 m^2/g (Figure 5.1). This analysis demonstrates how sensitive surface area is to linker structure. To achieve the most accurate LiMe ratio predictions these factors must be accounted for in the model.

Surface Area = 10,577 m^2/g

Surface Area = 12,220 m^2/g

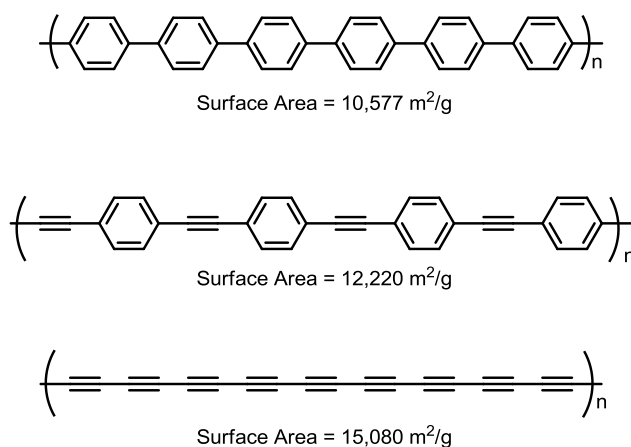Surface Area = 15,080 m^2/g

Figure 5.1. Theoretical geometric accessible surface area calculations for infinite chains of *p*-phenylene units, alternating phenylene and triple bonded units, and triple bonded units.

Another strategy for broadening the scope of the LiMe ratio surface area prediction model is to expand the types of compatible metal clusters. Rapidly becoming a benchmark material, MIL-53 consists of terephthalate linkers coordinating to metals ions such as Al^{3+} and Cr^{3+} to form a channeled pore structure having infinite rod metal clusters with the formula unit $M(CO_2R)_2(OH)$[3,4] Although this metal cluster is geometrically predisposed to avoid interpenetration,[5] the close packing of linkers extending from the metal cluster prevents this type of structure from achieving high surface area. Nevertheless, MCPs in this series have breathable channels that expand and shrink upon exposure to various chemical environments and have demonstrated in numerous examples post-synthetic modification and adsorbate selectivity using terephthalate-functionalized linkers.[6-8] A more versatile understanding of how surface area is affected by linker functionalization and extension would aid in both the rational design and optimization of this class of materials.

5.3 Improving Framework Stability

Applying supercritical carbon dioxide extraction of guests molecules to help MCPs achieve theoretically optimal surface areas has proven a critical advancement in MCP research.[9] Still, there are many existing materials that do not yet reach their surface area potential. In many of these cases, it is unclear whether individual labs lack the appropriate tools to correctly apply this method or if the current state of the technology is unable to accommodate activation of the most highly porous structures. This not only motivates further development of innovative activation techniques, but also drives the

need for more robust structures that do not need special practices for guest removal. The incorporation of ring fusion and linker coordination copolymerization techniques are discussed as methods for reconstructing those MCPs lacking significant structural stability into robust scaffolds.

5.3.1. Ring Fusion

Although ring fusion leads to a reduction in surface area (caused by formation of a less extended structure),[10] the increased stability afforded by a more rigid linker may outweigh this limitation, ultimately leading to higher surface areas. For example, linker **1** (Figure 5.2) coordinates with copper to form two polymorphic frameworks[11] having geometric accessible surface areas of approximately 4800 m^2/g.[10] Unfortunately, experimental surface areas have failed to reach values of even 1,000 m^2/g, revealing a significant lack of structural stability caused, potentially, by the rotational freedom of the triphenylamine subunits. Therefore, incorporation of ring fusion into the linker backbone in the form of carbazole groups, producing linker **2,** is recommended as a route to improved surface area. This same strategy is also suggested for other linker geometries such as **3**,[12] where carbazole units may be substituted into two different positions. It should be noted that, like other types of linker modifications, imparting ring fusion may not lead to MCPs having the same network topologies as their non-fused analogs; however, surface area is independent of pore shape and size as long as surfaces are similarly accessible for gas sorption.
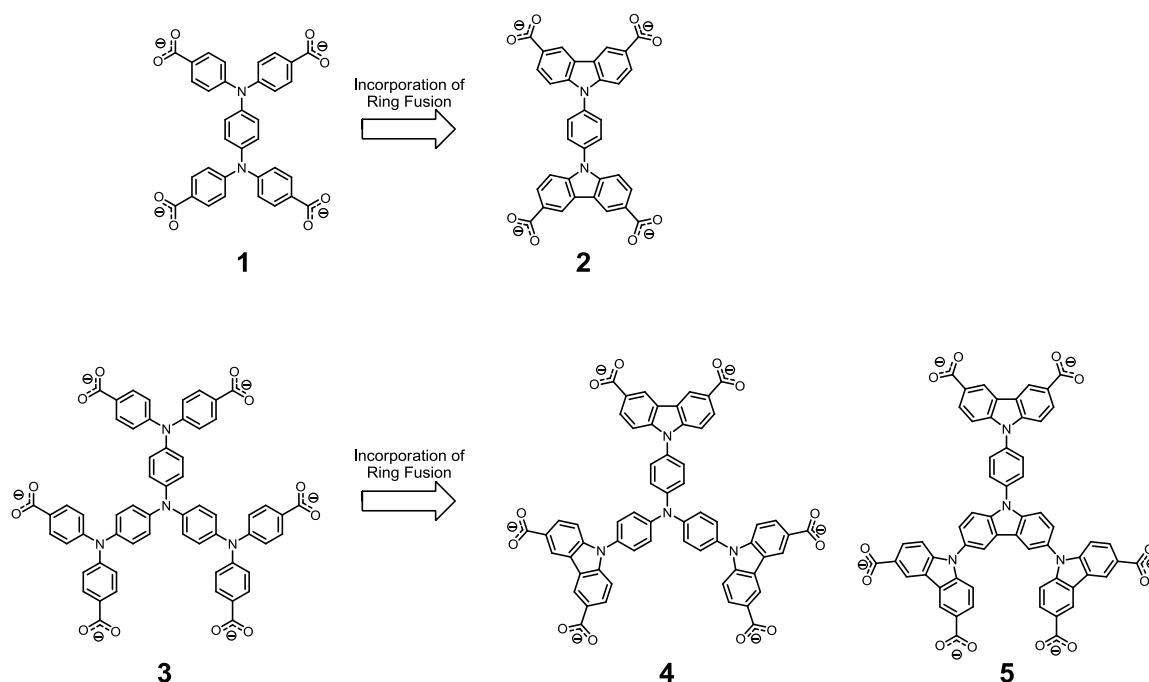
Figure 5.2. Conceptual modification of linkers through incorporation of ring fusion using carbazole units that offer potential to form structures with improved structural stability.

5.3.2. Linker Coordination Copolymerization

The method of linker copolymerization has been demonstrated utilizing topologically distinct linkers having different[13,14] and identical[15-19] functionality. By pairing with a second, more robust linker, both of these approaches may be applied in situations where a single linker does not offer enough support to produce a permanently porous framework. For example, in the work presented in Chapter 4, reduced symmetry linkers **6** and **7** (Figure 5.3) coordinate with Cu and Zn, respectively, forming MCPs lacking permanent porosity.[20] Because smaller linkers tend to form more robust structures, through copolymerization of linkers **6** and **7** with a smaller second linker such as terephthalate, **8**, or benzene-1,3,5-tricarboxylate, **9**, a structure with improved stability may emerge. In addition to unprecedented structural complexities that may arise due to incorporation of a third symmetry-inequivalent coordinating group, this method would

also reduce the cost associated with building block components by pairing linkers typically synthesized through metal-catalyzed cross-coupling reactions with cheaper, commercially available linkers.
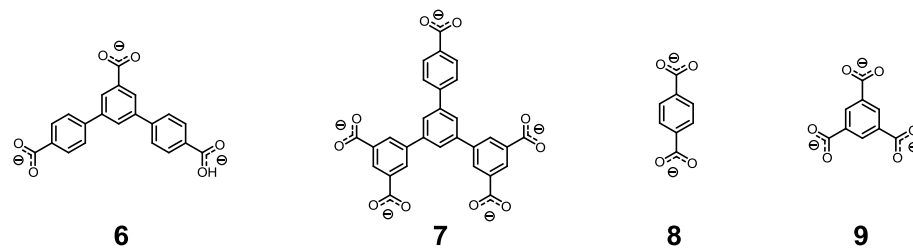

Figure 5.3 Linker copolymerization of linkers **6** and **7** with linkers **8** and **9** is suggested for the formation of robust MCPs displaying permanent porosity.

5.4. References

(1)   Düren, T.; Millange, F.; Férey, G.; Walton, K. S.; Snurr, R. Q. *J. Phys. Chem. C* **2007**, *111*, 15350-15356.

(2)   Farha, O. K.; Yazaydin, Ö.; Eryazici, I.; Malliakas, C. D.; Hauser, B. G.; Kanatzidis, M. G.; Nguyen, S. T.; Snurr, R.Q.; Hupp, J. T. *Nature Chemistry*, **2010**, *2*, 944 - 948.

(3)   Serre, C.; Millange, F.; thouvenot, C.; Noguès, M.; Marsolier, G.; Louër, Férey, G. *J. Am. Chem. Soc*. **2002**, *124*, 13519-13526.

(4)   Loiseau, T.; Serre,C.; Huguenard, C.; Find, G.; Taulelle, F.; Henry, M.; Bataille, T.; Férey, G. *Chem. Eur. J.* **2004**, *10*, 1373-1382.

(5)   Rosi, N. L.; Eddaoudi, M.; Kim, J.; O'Keeffe, M.; Yaghi, O. M. *Angew. Chem. Int. Ed*., **2002**, *41*, 294-297.

(6)   Tanabe, K. K.; Cohen, S. M.; *Chem. Soc. Rev*. **2011**, *40*, 498-519.

(7)   Couck, S.; Denayer, J. F. M.; Baron, G. V.; Rémy, T.; Gascon, J.; Kapteijn, F. *J. Am. Chem. Soc.* **2009**, *131*, 6326-6327.

(8)   Torrisi, A.; Bell, R. G.; Mellot-Draznieks, C. *Crystal Growth & Design*, **2010**, *10*, 2839-2841.

(9)   Nelson, A. P.; Farha, O. K.; Mulfort, K. L.; Hupp, J. T. *J. Am. Chem. Soc*. **2009**, *131*, 458-460.

(10)   Schnobrich, J. K.; Koh, K.; Sura, K. N.; Matzger, A. J. *Langmuir* **2010**, *26,* 5808-5814.

(11)   Sun, D.; Collins, D. J.; Ke, Y.; Z, J. L.; Zhou, H. C. *Chem. Eur. J*. **2006**, 12, 3768-3776.

(12)   Chae, H. K.; Eddaoudi, M.; Kim, J.; Hauck, S. I.; Hartwig, J. F.; O'Keeffe, M.; Yaghi. O. M. *J. Am. Chem. Soc.,* **2001**, *123*, 11482

(13)   Kitaura, R., Iwahori, F., Matsuda, R., Kitagawa, S., Kubota, Y., Takata, M., and Kobayashi, T. C. *Inorg. Chem*. **2004**, *43*, 6522– 6524

(14)   Ma, B.-Q., Mulfort, K. L., and Hupp, J. T. *Inorg. Chem*. **2005**, *44*, 4912– 4914

(15)   Koh, K.; Wong-Foy, A. G.; Matzger, A. J. *Angew. Chem., Int. Edit.* **2008**, *47*, 677-680.

(16)   Koh, K.; Wong-Foy, A. G.; Matzger, A. J. *J. Am. Chem. Soc.* **2009**, *131*, 4184-4185.

(17)   Koh,K.; Wong-Foy, A. G.; Matzger, A. J. *J. Am. Chem. Soc.* **2010**, *132*, 13005-13010.

(18)   Furukawa, H.; Ko, N.; Go, Y. B.; Aratani, N.; Choi, S. B.; Choi, E.; Yazaydin, E.; Ö.; Snurr, R. Q.; O'Keeffe, M.; Kim, J.; Yaghi, O. M. *Science* **2010**, *329*, 424-428.

(19)   Klein, N.; Senkovska, I.; Gedrich, K.; Stoeck, U.; Henschel, A.; Mueller, U.; Kaskel, S. *Angew. Chem. Int. Ed.* **2009**, *48*, 9954-9957.

(20)   Schnobrich, J. K.; Lebel, O.; Cychosz, K. A.; Dailly, A.; Wong-Foy, A. G.; Matzger, A. J. *J. Am. Chem. Soc.* **2010**, *132*, 13941-13948.